

UNIVERSITY OF SÃO PAULO  
SÃO CARLOS SCHOOL OF ENGINEERING

MURILO SARTORATO

**Micro and macroscale analyses for prognosis of composite structures: A  
new physics based multiscale methodology**

São Carlos

2018

MURILO SARTORATO

**Análises em micro e macro escala para o prognóstico de estruturas em material  
compósito: Uma nova metodologia baseada em mecanismos físicos**

**Versão Corrigida**

Tese apresentada à Escola de Engenharia de São Carlos, Universidade de São Paulo para obtenção do título de Doutor em Engenharia Mecânica.

Área de concentração: Aeronáutica

Orientador: Prof. Assoc. Volnei Tita

**ESTE EXEMPLAR TRATA-SE DA  
VERSÃO CORRIGIDA.  
A VERSÃO ORIGINAL ENCONTRA-  
SE DISPONÍVEL JUNTO AO  
DEPARTAMENTO DE  
ENGENHARIA MECANICA DA  
EESC-USP.**

São Carlos,  
2018



Class.	TESE ✓
Cutt.	10.120
Tombo	T22018
Sysno	2906252

31 100 21 17 73

10.10.18

AUTORIZO A REPRODUÇÃO TOTAL OU PARCIAL DESTE TRABALHO, POR QUALQUER MEIO CONVENCIONAL OU ELETRÔNICO, PARA FINS DE ESTUDO E PESQUISA, DESDE QUE CITADA A FONTE.

Ficha catalográfica elaborada pela Biblioteca Prof. Dr. Sérgio Rodrigues Fontes da EESC/USP com os dados inseridos pelo(a) autor(a).

S251m Sartorato, Murilo  
Micro and macroscale analyses for prognosis of composite structures: A new physics based multiscale methodology / Murilo Sartorato; orientador Volnei Tita; coorientador Ramesh Talreja. São Carlos, 2018.

Tese (Doutorado) - Programa de Pós-Graduação em Engenharia Mecânica e Área de Concentração em Aeronaves -- Escola de Engenharia de São Carlos da Universidade de São Paulo, 2018.

1. Composite materials. 2. Finite element analysis.  
3. Continuum fracture mechanics. I. Título.

Eduardo Graziosi Silva - CRB - 8/8907

MURILO SARTORATO

Micro and macroscale analyses for prognosis of composite structures:

A new physics based multiscale methodology

Revised Version

Thesis submitted to the São Carlos School of Engineering, University of São Paulo for the degree of Doctor of Science in Mechanical Engineering.

Concentration Area: Aeronautical Engineering

Supervisor: Associate Professor Volnei Tita

**THIS COPY CONTAINS THE  
REVISED VERSION.  
THE ORIGINAL VERSION CAN BE  
FOUND IN THE MECHANICAL  
ENGINEERING DEPARTMENT OF  
EESC-USP.**

São Carlos,  
2018

# FOLHA DE APROVAÇÃO

---

## FOLHA DE JULGAMENTO

Candidato: Engenheiro ANÍLIO SANTORATO.

Título da tese: "Análises em micro e macro escala para o prognóstico de estruturas em material compósito: uma nova metodologia baseada em mecânica fraca".

Data da defesa: 14/03/2018.

### Comissão Julgadora:

Prof. Associado Valnei Tito  
(Orientador)  
(Escola de Engenharia de São Carlos/EESC)

Prof. Dr. Marcelo Leite Ribeiro  
(Escola de Engenharia de São Carlos/EESC)

Prof. Dr. Edson Denner Leonel  
(Escola de Engenharia de São Carlos/EESC)

Prof. Dr. Marco Lucio Siffenour  
(Universidade Estadual de Campinas/UNICAMP)

Prof. Tit. Ramesh Rameshwar Taleja  
(Texas A&M University)

### Resultado:

APROVADO

Aprovado

Aprovado

Aprovado

APROVADO

Coordenador do Programa de Pós-Graduação em Engenharia Mecânica:

Prof. Associado Gherhard Sibelski

Presidente da Comissão de Pós-Graduação:

Prof. Associado Luis Fernando Costa Alberto

EESC/USP

Serviço de Pós Graduação

Protocolado em 03 / 10 / 2018

[Assinatura]

## DEDICATION

---

I would like to dedicate this work to my parents Eliana and Wilson and brother Fábio, whose unconditional support and love made the currently work possible.

## ACKNOWLEDGMENTS

---

I would like to thank all those who supported me from the duration of the studies for the development of this Thesis. In special:

To my supervisor, friend and tutor, the Professor Volnei Tita, for both the challenge and his guidance, knowledge and support, which made possible the execution and conclusion of this work.

To my co-supervisor, Professor Ramesh Talreja for welcoming my stay for in Texas, and whose knowledge, didactic and experience showed me new ways to think and renewed my motivation for research work.

To Professors Marcelo Leite Ribeiro and Mauricio Francisco Caliri Junior, whose support and discussions with different continuum mechanics theories greatly improved the present work.

To my friends from USP from the Aeronautical Structures Group, and in special to Felipe and Matheus.

To my friends from Texas A&M University from Prof. Talreja's group Linqi, Aswathi, Sarah and Lucio.

To my friends Lono, Rodolfo and Gray, whose support and friendship in different phases of my life during this PhD will never be forgotten.

To my parents and brother, whom always encouraged and gave their unconditional support.

To the aeronautical structures group (GEA), for the discussions on this work.

And finally, I would like to thank CAPES (Process Numbers: DS00011/07-0 and PDSE 99999.007060/2015-07) and FUSP (Process Number: 3016/TT-4) and for the financial support without which I would not be able to write this thesis.

## RESUMO

---

SARTORATO, Murilo. **Análises em micro e macro escala para o prognóstico de estruturas em material compósito: Uma nova metodologia baseada em mecanismos físicos.** 2018. 78 folhas. Tese (Doutorado em Engenharia Mecânica) – Escola de Engenharia de São Carlos, Universidade de São Paulo, São Carlos, 2018.

Atualmente, um dos maiores desafios nas áreas de Ciências dos Materiais e Engenharia Estrutural é efetuar análises precisas de previsão de dano em materiais compósitos – evolução e falha. Embora diversos modelos e critérios de falha existam na literatura para a simulação de dano em materiais compósitos, a maior parte dos modelos não produzem resultados aceitáveis para projetos estruturais detalhados. Os modelos atualmente em uso costumemente sub ou superestimam as cargas necessárias para a degradação e falha de materiais. Esse fato ocorre, pois, esses modelos são baseados em dados experimentais e/ou semi-empíricos ou modelos fenomenológicos. Essa abordagem negligencia a anisotropia e heterogeneidade inerente de materiais compósitos, que causam diversos mecanismos de falha ocorrendo simultaneamente em diferentes fases e escalas do material. Uma possível solução para esse problema é a utilização e/ou desenvolvimento de novos modelos de dano e falha baseados em abordagens multiescala e mecanismos físicos de falha baseados em Mecânica da Fratura. Nesse cenário, o principal objetivo do presente trabalho consiste no estudo e desenvolvimento de modelos de dano baseados em abordagens multiescala aplicados aos materiais compósitos manufaturados via fibras unidirecionais para diferentes casos de carga: tração pura, flexão pura, tração-flexão e cargas multiaxiais. Para o desenvolvimento desses modelos, publicações foram avaliadas criteriosamente e novas formulações foram estudadas, adaptadas e melhoradas. A metodologia básica se baseia na utilização de técnicas de homogeneização para obter propriedades elástica degeneradas a partir de Volumes Elementares Representativos (VER); o perfil de dano do VER é definido a partir de trincas intralaminares paralelas às fibras e calculadas através de uma abordagem multiescala. Essa abordagem compreende três modelos separados: um para a macro escala utilizado para o cálculo preciso de tensões e deformações em pontos críticos; e dois na microescala para previsão de dano intralaminar. Esses modelos interagem entre si, sendo que



os resultados obtidos em alguns modelos são utilizados como condições de contorno em outros de forma iterativa. Esses modelos foram implementados utilizando códigos em linguagem Python independentes e de automatização, bem como sub-rotinas (UEL – *User Element Subroutine*) em linguagem Fortran vinculadas ao pacote comercial de elementos finitos Abaqus™.

Palavras Chave: Materiais Compósitos, Método dos Elementos Finitos, Mecânica da Fratura, Análise Multiescala.

## ABSTRACT

---

SARTORATO, Murilo. **Micro and macroscale analyses for prognosis of composite structures: A new physics based multiscale methodology.** 2018. 78 sheets. Thesis (Ph. D. in Mechanical Engineering) – São Carlos School of Engineering, University of São Paulo, São Carlos, 2018.

Currently, one of the greatest challenges for the areas of Material Sciences and Structural Engineering is to perform accurate analysis for prediction of damage in composite materials, the evolution of damage and failure. Although several models and failure criterion already exist for the simulation of damage in composite materials, most models do not produce acceptable results for detailed designs. The models currently in use often under or overestimate loads required for the degradation and failure. This occurs as most of these models is based upon phenomenological or semi-empirical data, which adjust failure surfaces or failure envelopes to experiments. This approach neglects the inherent anisotropy and heterogeneity of composite materials, which cause several failure mechanisms to occur simultaneously in different materials scales and phases. One possible solution to this problem is to use and/or develop new damage and failure models based on multiscale approaches and physical failure mechanisms based on Continuum Fracture Mechanic. In this scenario, the main objective of the present work consists on studying and developing multiscale based damage models applied to composite structures manufactured with unidirectional fibers under different load cases: pure tensile, pure bending, mixed tensile-bending and multiaxial. For the development of these models, works found in the literature were critically evaluated and new formulations were studied, adapted and improved upon. The basic methodology is based on using homogenization techniques to obtain degenerated elastic properties from damaged Representative Volume Elements (RVEs); the damage profile of the RVE is defined as intralaminar cracks parallel to the fiber directions and is calculated using a multiscale approach. The multiscale approach comprehends three separate models, one in the macroscale for the calculation of accurate stress/strain states in the critical points, and two in the microscale for the prediction of intralaminar damage (matrix cracking). These models interact between themselves, as the results from each one are used as boundary conditions for the other in a computational analysis loop over load steps via an iterative process. The

developed models were implemented either stand-alone Python codes or into the finite element analysis package Abaqus™ using its automatization capabilities with Python scripts, as well as subroutines in Fortran (UEL – User Element Subroutine) linked to commercial finite element package Abaqus™.

Key words: Composite Materials, Finite Element Method, Continuum Fracture Mechanics, Multiscale analysis.

## LIST OF FIGURES

---

Figure 1 – (a) Boeing 787; (b) Airbus 380; (c) Airbus 350	25
Figure 2 – Qualitative study showing the lack of scientific papers that link macro and microscale analysis.	28
Figure 3 – Maximum Stress Criterion Failure Surface	34
Figure 4 – Tsai-Hill Failure Surface	35
Figure 5 – Tsai-Wu Criterion Failure Surface	36
Figure 6 – Ducker-Prager failure surface	37
Figure 7 – Bresler-Pister failure surface	37
Figure 8 – Square Unit Cell	41
Figure 9 – Hexagonal Unit Cell	41
Figure 10 – Examples of RVEs for composite materials.	42
Figure 11 – General behavior of damage evolution in composite materials	46
Figure 12 – Three point bending test of a $[0^\circ/90^\circ/0^\circ/90^\circ/0^\circ]$ laminate showing progressive failure of the layers, highlighted by the red circles. Force [kN] vs. deflection [mm].	47
Figure 13 - Scientific methodology used on the present PhD Thesis	51
Figure 14 – Computational procedure developed in the present work	51
Figure 15 – Shell finite element	55
Figure 16 – Schematic difference between ESL theories (left) and LW theories (right)	57
Figure 17 – Different types of applied loads in laminates compatible with unified theories	58
Figure 18 – Approach of modelling each material point with a different “RVE” considering different amounts of damage, dependent on the deformation energy available at the material point	62
Figure 19 – Methodology implementation flowchart	63
Figure 20 – Transversal Isotropic Material	66
Figure 21 – Lamina coordinate system rotation	66
Figure 22 – Shell finite element domain representation	75
Figure 23 – Compatibility imposition between layers. Example for the K13 matrix, $Nu1 = 2$ and $Nu3 = 3$	80
Figure 24 – Compatibility imposition between layers in the presence of delamination, example between Layers 2 and 3	81
Figure 25 - Shell finite element domain representation	85
Figure 26 – Representation of possible problem of unified formulations with boundary conditions applied through penalty or substitution methods	90
Figure 27 – Iterative loop for optimization of displacement orders for classic formulations	95
Figure 28 - Iterative loop for optimization of displacement orders for mixed formulations	96
Figure 29 – First numerical test	99
Figure 30 – Second numerical test	102

Figure 31 – $\sigma_{13}$ Stress distribution over the thickness for different theories, Classic Case, Point C, $[(+30/-60)_4]_T$ lay-up	105
Figure 32 – $\sigma_{23}$ Stress distribution over the thickness for different theories, Classic Case, Point C, $[(+30/-60)_4]_T$ lay-up	106
Figure 33 – $\sigma_{13}$ Stress distribution over the thickness for different theories, Classic Case, Point C, $[0/90/+45]_S$ lay-up	106
Figure 34 – $\sigma_{23}$ Stress distribution over the thickness for different theories, Classic Case, Point C, $[0/90/+45]_S$ lay-up	107
Figure 35 – Third numerical test	108
Figure 36 – Crack propagation Modes	112
Figure 37 - Example of process of damage evolution through increase in crack density in the microscale model for a $[\pm 60^\circ_4]_S$ laminate	114
Figure 38 – (a) Schema of the first phase of crack multiplication; (b) Experimental results showing periodicity in multiple cracks	115
Figure 39 - Principal strain at the center of a cracked layer over the distance away from the crack in a $[0^\circ/90^\circ_2]_S$ laminate	115
Figure 40 - Analytical stresses away from the crack center under bending for a $[90^\circ/0^\circ]_S$ laminate	116
Figure 41 – Schematics of the COD definition	117
Figure 42 – Example of geometry of the proposed model for a $[0^\circ/90^\circ/0^\circ]$ laminate to verify the hypothesis to neglect sliding. Center crack (left). Edge Crack (right).	119
Figure 43 - Example of a $\Delta W$ vs. $\lambda$ (or $\rho$ ) vs. $P$ (or $\phi$ ) surface	119
Figure 44 - Crack evolution under bending for the proposed analyses of a $[0^\circ/\pm 60^\circ_2]_S$ laminate	121
Figure 45 - Example of RVE used for the Mode II influence verification on a $[0^\circ/90^\circ/\pm 60^\circ]_S$ lay-up. (a) Geometrical model and cracks. (b) Mesh. (c) Example of a normalized displacement distribution over the thickness	122
Figure 46 - Evolution of the analysis for crack displacements for $60^\circ$ . a. First cracked and failed layer (ninth layer); b. Second cracked and failed layer (eighth layer for balanced, sixth layer for unbalanced)	123
Figure 47 - Evolution of the analysis for shear stress near the cracks for $60^\circ$ . a. First cracked and failed layer (ninth layer); b. Second cracked and failed layer (eighth layer for balanced, sixth layer for unbalanced)	124
Figure 48 - Mesh densities convergence tests for tensile loads for various laminates	125
Figure 49 - Mesh densities convergence tests for bending loads for a $[0^\circ/90^\circ_4/0^\circ]$ laminate	125
Figure 50 - RVE dimension convergence tests for bending loads for various laminates	125
Figure 51 – (a) Problematic points found in the $[0^\circ/\pm 75^\circ_2]_S$ laminate; (b) Example of crack behavior near the corner in the problematic model; (c) Example of crack problematic corner in the parallelepiped model; (d) Hexagonal prism model solution.	126
Figure 52 - Boundary conditions for the hexagonal prism model	127
Figure 53 – Example of RVE geometry used for a cross-ply lay-up with only $90^\circ$ damaged layers	127

Figure 54 - Example of RVE geometry used for an angled-ply lay-up with: (a) only 60° damaged layers; (b) only - 30° damaged layers	127
Figure 55 - Example of RVE geometry used for a generic lay-up with damaged layers oriented at -45°, 30°, 60° and 90°	128
Figure 56 - Load Cases and Boundary Conditions for the homogenization procedure	129
Figure 57 - Representation of the periodicity boundary conditions	131
Figure 58 - Energy required for crack multiplication surface for a $[0^{\circ}_2/90^{\circ}_4]_s$ laminate	132
Figure 59 - Results for a laminate $[0^{\circ}_2/90^{\circ}_4]_s$ property degradation under tensile loads	132
Figure 60 - Results for a laminate $[0^{\circ}_2/90^{\circ}_4]_s$ property degradation under bending loads	133
Figure 61 - Normalized average COD for a $[0^{\circ}/90^{\circ}]_s$ glass-epoxy laminate, present work vs. literature	134
Figure 62 - Damage evolution for $[0^{\circ}/90^{\circ}]_s$ and $[0^{\circ}/90^{\circ}/\pm 45^{\circ}]_s$ glass-epoxy laminate	135
Figure 63 - COD vs. crack density and damage evolution for a $[90]_s$ carbon-epoxy laminate	135
Figure 64 - COD vs. crack density for the two bottommost 90° layers in $[0^{\circ}/90^{\circ}/0^{\circ}/90^{\circ}/0^{\circ}]_s$ lay-up under pure bending load.	136
Figure 65 - COD vs. crack density and damage evolution for the two bottommost 90° layers in a $[0^{\circ}/90^{\circ}/0^{\circ}/90^{\circ}/0^{\circ}]_s$ lay-up under pure bending load	137
Figure 66 - Comparison between present methodology and experimental results for a $[90^{\circ}_{10}]$ laminate under tension	138
Figure 67 - Comparison between present methodology and experimental results for a $[\pm 67.5^{\circ}_{10}]_s$ laminate under tension	138

## LIST OF TABLES

---

<i>Table 1 – Other failure surfaces based criteria</i>	37
<i>Table 2 – Shell deformation theories</i>	55
<i>Table 3 – Z meaning for classic formulation</i>	77
<i>Table 4 – Z meaning for mixed formulations</i>	87
<i>Table 5 - Geometric and material properties for the numerical tests</i>	97
<i>Table 6 - Results for First Numerical Test – Classic Model. Maximum normal stress value at critical layer in MPa. Simple lay-ups.</i>	98
<i>Table 7 – Results for First Numerical Test – Classic Model. Maximum normal stress value at critical layer in MPa. Complex lay-ups.</i>	99
<i>Table 8 - Results for First Numerical Test – Mixed Model. Maximum normal stress value at critical layer in MPa. Simple lay-ups.</i>	100
<i>Table 9 - Results for First Numerical Test – Classic Model. Maximum normal stress value at critical layer in MPa. Complex lay-ups.</i>	100
<i>Table 10 - Results for Second Numerical Test – Bisinoidal Case – Classic Model. Transversal displacement at the center of the plate.</i>	102
<i>Table 11 - Results for Second Numerical Test – Bisinoidal Case – Mixed Model. Transversal displacement at the center of the plate.</i>	103
<i>Table 12 - Results for Second Numerical Test – Uniform Case – Classic Model. Transversal displacement at the center of the plate.</i>	103
<i>Table 13 - Results for Second Numerical Test – Uniform Case – Mixed Model. Transversal displacement at the center of the plate.</i>	104
<i>Table 14 - Results for Third Numerical Test – Uniform Case – Mixed Model. Transversal displacement at the center of the plate.</i>	109
<i>Table 15 - Results for Third Numerical Test – Uniform Case – Mixed Model. Transversal displacement at the center of the plate.</i>	109
<i>Table 16 - Material properties used for the CSD damage mode evaluation tests</i>	120
<i>Table 17 - Properties fo the analyzed material layers</i>	133

## LIST OF ABBREVIATIONS

---

CGF	Caliri's Generalized Formulation
CUF	Carrera's Unified Formulation
CDM	Continuum Damage Mechanics
CFM	Continuum Fracture Mechanics
COD	Crack Opening Displacements
CSD	Crack Sliding Displacements
ESL	Equivalent Single Layer
FEM	Finite Element Method
GUF	Generalized Unified Formulation
LW	Layer-Wise
RMVT	Reissner's Mixed Variational Theorem
RVE	Representative Volume Element
UD	Unidirectional
UC	Unit Cell



## SUMMARY

---

<b>FOLHA DE APROVAÇÃO</b>	<b>6</b>
<b>DEDICATION</b>	<b>7</b>
<b>ACKNOWLEDGMENTS</b>	<b>9</b>
<b>RESUMO</b>	<b>11</b>
<b>ABSTRACT</b>	<b>13</b>
<b>LIST OF FIGURES</b>	<b>XV</b>
<b>LIST OF TABLES</b>	<b>19</b>
<b>LIST OF ABBREVIATIONS</b>	<b>21</b>
<b>SUMMARY</b>	<b>23</b>
<b>1 INTRODUCTION, MOTIVATION AND OBJECTIVES</b>	<b>25</b>
1.1 PROBLEM DESCRIPTION AND APPLICATIONS	25
1.2 OBJECTIVES	29
1.3 CHAPTER ORGANIZATION	30
<b>2 ON THE MECHANISMS OF DAMAGE AND FAILURE ON COMPOSITE MATERIALS</b>	<b>33</b>
2.1 HISTORY OF THE STUDY OF DAMAGE IN COMPOSITE MATERIALS	33
2.2 FIRST DAMAGE THRESHOLD: HETEROGENEOUS MICROSCALE	40
2.3 CONTINUUM FRACTURE MECHANICS FIRST DAMAGE THRESHOLD: HOMOGENEOUS MICROSCALE	43
2.4 DAMAGE EVOLUTION	45
<b>3 MULTISCALE METHODOLOGY</b>	<b>49</b>

3.1	MACROSCALE ANALYSIS METHODOLOGY	52
3.2	MICROSCALE ANALYSIS METHODOLOGY	59
<b>4</b>	<b><u>MACROSCALE MECHANICAL MODELS: SHELL THEORIES</u></b>	<b>65</b>
4.1	COMPOSITE CONSTITUTIVE EQUATIONS	65
4.2	OVERVIEW OF SHELL DEFORMATION THEORIES AND SHEAR LOCKING	69
4.3	UNIFIED FORMULATIONS	71
4.4	CLASSIC "CLASSIC" FORMULATION	72
4.5	MIXED FORMULATION	82
4.6	BOUNDARY CONDITIONS IMPLEMENTATION	89
4.7	FINITE ELEMENT IMPLEMENTATION	92
4.8	ORDER OPTIMIZATION IMPLEMENTATION	93
4.9	RESULTS	97
4.9.1	FIRST TEST: FLAT RECTANGULAR PLATE UNDER PURE TENSILE LOADS	98
4.9.2	SECOND TEST: FLAT SQUARE PLATE UNDER TRANSVERSAL PRESSURE	101
4.9.3	THIRD TEST: HALF CYLINDER UNDER UNIFORM PRESSURE	107
<b>5</b>	<b><u>MICROSCALE MECHANICAL MODELS: DAMAGE EVOLUTION AND</u></b>	
	<b><u>HOMOGENIZATION</u></b>	<b>111</b>
5.1	COD DAMAGE EVOLUTION MODEL OVERVIEW	113
5.2	UNBALANCING AND OPENING VS. SLIDING STUDIES	120
5.3	GEOMETRIC CONVERGENCE TESTS, ADAPTATIONS AND SOLUTIONS	124
5.4	HOMOGENIZATION MODEL	128
5.5	RESULTS	133
<b>6</b>	<b><u>FINAL DISCUSSIONS, CONCLUSIONS AND FUTURE DEVELOPMENTS</u></b>	<b>139</b>
<b>7</b>	<b><u>PUBLICATIONS</u></b>	<b>141</b>
<b>8</b>	<b><u>REFERENCES</u></b>	<b>145</b>
	<b><u>APPENDIX I – MACROSCALE CODE FLOWCHART (GUF)</u></b>	<b>153</b>
	<b><u>APPENDIX II – MICROSCALE CODE FLOWCHART (DAMAGE EVOLUTION)</u></b>	<b>155</b>

## 1 INTRODUCTION, MOTIVATION AND OBJECTIVES

---

### 1.1 Problem description and applications

Since the introduction of composite materials between the 1950 and 1960 decades, their use has been steadily increasing in areas with high structural demand and efficiency, such the high-end automobilist, rail transport, aeronautical and aerospace industries. In particular, in the aerospace industry, some recent projects incorporate composite materials extensively through primary and secondary structural elements, such as the Boeing 787 and the Airbus 350 and 380 aircrafts (Figure 1).

Figure 1 – (a) Boeing 787; (b) Airbus 380; (c) Airbus 350



(a)

(b)

(c)

Source: (a) Boeing (2017); (b) Airbus (2017); (c) Airbus (2017)

As such, both academia and industry dedicated extensive study and research time for the correct prediction and simulation of structures manufactured using composite materials. While several categories and classifications of composite materials exist, for most primary structural applications in the previously mentioned industries, composite materials refer to laminated plates manufactured from two phases: a matrix embedded with continuous fiber reinforcements. These materials in most applications are made of polymeric matrix – such as epoxy, Polyether Ether Ketone (PEEK), Polyphenylene Sulfide (PPS), and others – and continuous unidirectional fibers – such as more commonly used ones (carbon or glass fibers), or uncommon ones like organic fibers (cotton, sisal), metal fibers (boron, aluminum) or polymeric fibers (nylon, Kevlar, Nomex). This assemble creates a heterogeneous and

anisotropic medium that mechanically behaves in a complex manner, and introduces several design variables and optimization problems: the use of different fiber orientations lay-ups, constituents and thicknesses creates the possibility of controlling the anisotropy, and in turn mechanical properties, optimizing the structure behavior both in static and dynamic cases (Talreja and Singh, 2014).

This inherent anisotropy and heterogeneity also cause different damage and failure mechanisms to occur simultaneously in different materials scales and phases. This particular characteristic of composite materials changes its mechanical behavior in ways that increases the complexity of damage and failure prediction. As such, damage and failure models that do not contemplate the fact that different mechanisms may occur simultaneously and interact may lead to inconsistent results, as these interactions may both advance or delay damage and failure (Talreja, 2014). Several researches observed this fact in the World-Wide Failure Exercises (WWFE – Hinton et al., 2004; WWFE-II – Kaddour and Hinton, 2012; Kaddour and Hinton, 2013; Hinton et al., 2011; and WWFE-III – Kaddour et al., 2013). These were exercises in which different research groups around the World tried different models to predict the stress and/or strain levels to failure in different laminates for known experiments and cases found in the literature. According to Hinton et al. (2011), the general results up to the second edition of the exercises were that “There is no universal definition for what constitutes ‘failure’ of a composite structure [...]” and “[...] none of the current predictive failure theories were considered to be credible for use in practical engineering applications”. The third exercise showed similar results, while also showing that multiscale theories, while promising, still need more development and study to be used in practical applications (Kaddour et al., 2013). In particular, this led to the belief that models based on metallic material behavior, such as Tsai-Wu and Tsai-Hill (Talreja, 2014), or that are based on semi-empirical damage and failure parameters, such as Hashin’s, Puck’s or Ladevèze’s models, which are still common in the industrial environment, are outdated and unreliable in terms of physic meaning.

This problem introduced some conceptual changes in the numerical and analytical modelling of damage and failure of composite materials. Starting in the second half of the 1990-decade, the damage and failure prediction models switched from analysis based only on homogenized materials and stress states to problems based on the behavior of the material microstructure and the interaction between separate phases – different layers or fibers and

matrix (Talreja, 2016). For that, researchers started developing models and analysis that use or apply to two or more different materials scales – macro and microscales –, which are referred to multiscale analysis. In addition, models and methodologies, as well as studies that better detailed several different mechanisms such as crack propagation and multiplication, delamination onset, propagation and fiber cracking started to appear in the literature. This view changes brought a shift on the focus from damage prediction based on phenomenological and semi-empirical models to models based on the actual physic-based failure mechanisms, thus moving to theories based upon thermodynamic consistent models (Lemaitre, 1996; Lemaitre and Desmorat, 2005; Ladevèze and LaDantec, 1996) or fracture mechanics (Varna and Berglund, 1991; Varna et al., 1993; Varna et al., 1999; Singh et al., 2009; Singh and Talreja, 2010; Carraro and Quaresimin, 2014). However, those shifts introduced several challenges for the prediction analysis; above all, the high computational cost required for multiscale analysis and the difficulty in obtaining design level applicable damage and/or failure data from such models (Carraro and Quaresimin, 2014).

In addition, because of the extensive research on the problem of finding homogenized properties in damaged materials by using several known methods, such as finite element analysis of Representative Volume Elements (RVEs), holistic approaches, and different homogenization techniques, the problem of obtaining degraded elastic properties has become trivial, given that one knows the damage profile. As such, the main problem resides in how to predict the damage profile of a certain laminate for a certain load level or history; and how to obtain ways to link macroscopic metrics – i.e. applied load, displacement, deformation energy – to microscopic metrics – i.e. crack density, local stress/strain states at critical points, delaminated area.

On the problem of ways to link the different scales, the literature shows a lack of works that approach the problem by using macroscopic computational mechanics, focusing for example in cinematic models, and material mechanics, focusing for example in damage and fracture prediction models. For example, Figure 2 shows a qualitative study counting the scientific papers found between 1988 and 2018 on the Web of Science database for combinations of keywords that deal with either sides of the problem, which clearly shows this gap.



aforementioned industries largely sought damage prediction analysis using numerical simulations via the FEM, because of the possibility of creating optimization routines and simulating virtual tests and structures.

## 1.2 Objectives

The general objective of the present thesis consists in contributing and adding to the study and development of intralaminar damage models applicable to composite materials; i.e. the development of models that are based upon physic-based damage mechanisms using multiscale models and finite element analysis. In particular, the focus of the present study is in the analysis of composite laminated beams and plates manufactured from unidirectional (UD) plies under different types of loads: uniaxial pure tensile, bending, combined membrane-bending and multiaxial loads.

As such, the present work as the following specific objectives:

- Investigate, select and adapt computational multiscale models and methodologies from the literature for the prediction of intralaminar damage in composite materials.
- Develop new models and methodologies that applied to the load cases of interest: tensile, bending, combined tensile-bending, and that can be used for generalized laminates, including the angled-ply and asymmetric cases.
- Identify the limitations for the selected, adapted and/or developed models and methodologies and proposed solutions for these applications, modifying and improving these models and methodologies, discussing, validating and/or analyzing the limitations and potentialities of said solutions.
- Implement the models and methodologies in sub-routines, either using stand-alone Python codes or linked to the commercial FEM package Abaqus<sup>TM</sup>, using modelling automatization Python scripts, as well as user subroutines in Fortran (UEL – User Element Subroutine) linked to Abaqus.
- Validate the models using experimental and computational tests, as well as data and analytical solutions found in the literature.

### 1.3 Chapter organization

In order to keep a better organization and help the reading of the work, the present thesis is divided into 7 (seven) chapters, which are summarized as follows:

**Chapter 1. Introduction, Motivations and Objectives** – the first chapter presents the introduction, motivation, objectives as well as the thesis organization.

**Chapter 2. On the Mechanisms of Damage and Failure on Composite Materials** – the second chapter presents a brief literature review of the history of the studies on damage and failure prediction on composite materials and the current studies regarding damage initiation, evolution and failure. In addition, the chapter describes the different concepts and methodologies used on the present work, such as the concept of multiscale analysis and the logic used for the choice of this approach.

**Chapter 3. Multiscale Methodology** – the third chapter discusses and details the multiscale methodology developed in the present work for the prediction of intralaminar damage evolution in composite materials. The chapter proceeds to show the different phases and the iteration loop used in the computational simulations for this methodology, and their different implementations using stand-alone in-house Python codes and automation Python scripts interpreted using the finite element commercial software Abaqus.

**Chapter 4. Macroscale Mechanical Models: Shell Theories** – the fourth chapter focus on the macroscale analysis phases of the developed methodology, showing a brief literature review on the history of shear deformation theories for shells, showing the differences between linear and high-order theories, as well as between equivalent single layer and layer-wise theories. Following that, the chapter shows the formulation used in the present work to obtain an accurate stress distribution over the thickness of the laminate, explaining an adapted Generalized Unified Formulation (GUF), which was first proposed by Demasi (2009). Thus, the main equations, its implementation through a finite element solution, discussions on open problems and proposed solutions for the formulation such as application of boundary conditions are presented. Then, the chapter shows an interactive algorithm for obtaining the least computational costly deformation theory for a given problem. Finally, the chapter ends



showing numerical experiments for validation of the adapted formulation and implementation via UEL linked to Abaqus, and other results.

**Chapter 5. Microscale Mechanical Models: Damage Evolution and Homogenization** – the fifth chapter describes the microscale models and simulations phases of the developed methodology, focusing on crack multiplication analysis, used to obtain the damage quantities, and the homogenization models. The first subsection presents a brief literature review of crack multiplication models based on Crack Opening Displacements (COD) and/or Crack Sliding Displacements (CSD), as well as its adaption and implementation by the present work. In addition, subsections present issues found in the original models regarding angled laminates and the generalizations and solutions developed in the present work. Following that, another subsection of the chapter shows the homogenization model used to obtain the degenerated properties of a damaged laminate. Finally, the chapter ends showing numerical experiments for validation of the adapted formulation using analytical solutions found on the literature and experimental results.

**Chapter 6. Final Discussions, Conclusions and Future Developments** – the sixth chapter presents a brief discussion of the results presented on the previous chapters and the developed methodology, and summarizes the conclusions of the work presented on the thesis based on these results, correlating them with the established objectives. Finally, a final paragraph presents a brief discussion of issues and improvements over the developed methodology.

**Chapter 7. References** – the last chapter presents the different references used to develop the present PhD Thesis, including scientific papers, books and technical manuals.



## 2 ON THE MECHANISMS OF DAMAGE AND FAILURE ON COMPOSITE MATERIALS

---

This chapter presents a brief literature review of the history of the studies on damage and failure prediction on composite materials and the current studies regarding damage initiation, evolution and failure. In addition, the chapter describes the different concepts and methodologies used on the present work, such as the concept of multiscale analysis, Representative Volume Elements (RVE), Unit Cells (UC) and the logic used for the choice of this approach and a brief literature review on the topic.

### 2.1 History of the study of damage in composite materials

The prediction of damage in composite materials has an evolution throughout history. In general, the earlier criterions were based upon the premise that composite failure could be obtained from basic material rupture properties in the composite principal directions: aligned to the fibers, i.e.  $X_T$  and  $X_C$  – obtained from tensile and compression tests using a unidirectional laminate with all fibers oriented at  $0^\circ$  degree angle, transversal to the fiber direction, i.e.  $Y_T$  and  $Y_C$  – obtained from tensile and compression tests using a unidirectional laminate with all fibers oriented at  $90^\circ$  angle and under maximum shear, i.e.  $S_{12}$  – obtained from tensile tests using a laminate with fibers oriented at  $\pm 45^\circ$  angle. Initially, in the decades of 1950 and 1960 when orthotropic and anisotropic materials were starting to be used in practical applications; laminated composite structures were calculated using simple models based upon maximum stresses and strains criteria; using experimental data from tensile tests of laminates oriented with different angles as explained earlier. These models use simple comparisons between the stresses or strains over the laminate and the rupture values obtained from the experimental tests for a given orientation.

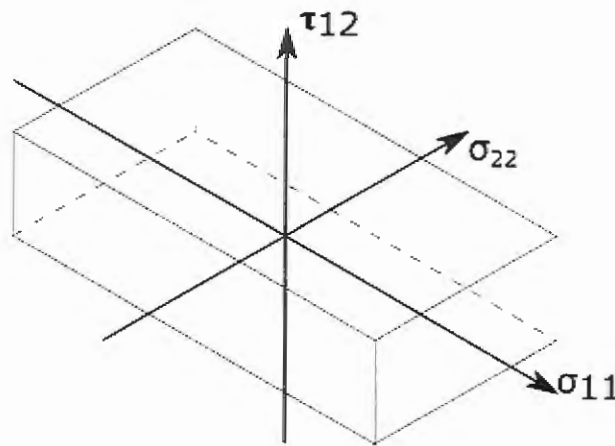
For example, Equation 1 summarizes the Maximum Stress Criterion, which compares the in-plane stresses ( $\sigma_{11}$ ,  $\sigma_{22}$  and  $\tau_{12}$ ) with the resistance values for a composite found in the fiber direction. By the same logic, Equation 2 shows the Maximum Strain Criterion, which can be constructed using the in-plane strains ( $\epsilon_{11}$ ,  $\epsilon_{22}$  and  $\gamma_{12}$ ) and the maximum strains values corresponding to the tests and directions mentioned in the Maximum Stresses Criterion

$(X'_{T/C}, Y'_{T/C}, S'_{12})$ . These criterion can be understood as a failure surface with a parallelepiped shape shown in Figure 3.

$$-X_C \leq \sigma_{11} \leq X_T, -Y_C \leq \sigma_{22} \leq Y_T, |\tau_{12}| \leq S_{12} \quad (1)$$

$$-X'_C \leq \varepsilon_{11} \leq X'_T, -Y'_C \leq \varepsilon_{22} \leq Y'_T, |\gamma_{12}| \leq S'_{12} \quad (2)$$

Figure 3 – Maximum Stress Criterion Failure Surface

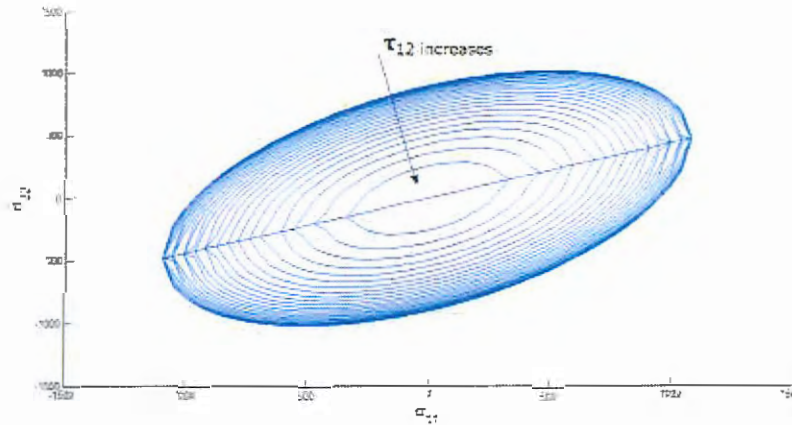


Source: Developed by the author

One of the first failure criteria developed specifically for composite materials was the Tsai-Hill criterion (Azzi and Tsai, 1965). This model was based upon the Hill criterion (Hill, 1948) for yielding of anisotropic metals, using hypothesis of plane state of stresses, and thus, altering Hill's original yielding resistances to the maximum resistances of each layer principal directions. Under this prerogative is implied the hypothesis that every failure in composite materials is a brittle failure. This model generates a different conic failure surface for each of the quadrants for a  $(\sigma_1, \sigma_2)$  pair for each stress state in the ply  $(\sigma_1, \sigma_2, \sigma_{12})$ , shown in Equation 3 and Figure 4. This happens because of the different resistance values for failure under traction and compression tests in the fiber and transverse directions, and a single shear resistance value.

$$g(\sigma) = \left(\frac{\sigma_{11}}{X_{T|C}}\right)^2 + \left(\frac{\sigma_{22}}{Y_{T|C}}\right)^2 - \frac{|\sigma_1\sigma_2|}{X_{T|C}^2} + \left(\frac{\sigma_{12}}{S_{12}}\right)^2 - 1 \leq 0 \quad (3)$$

Figure 4 – Tsai-Hill Failure Surface



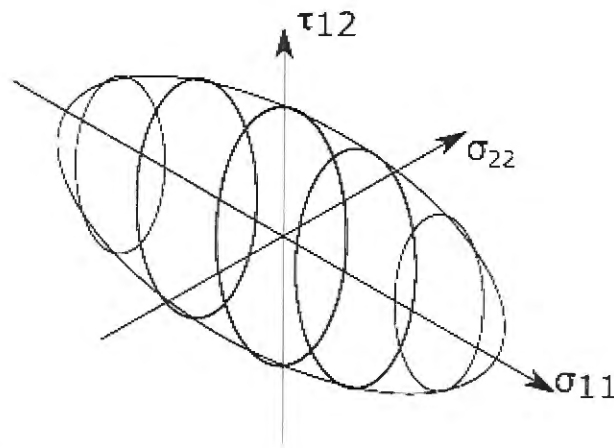
Source: Developed by the author

Years later, the same approach of the creation of a failure surface was used to develop the Tsai-Wu criterion (Tsai e Wu, 1971). This criterion uses a conic failure surface to bypass the plane stress state hypothesis, by using three quadratic inequalities, each one containing three of the six terms of a full stress tensor and five coefficients, which are obtained from an orthotropic material ultimate strengths in the principal directions. Its mathematical expression and schematic shape are found in Equations 4 and 5 and Figure 5 respectively.

$$g(\sigma) = F_1\sigma_{11} + F_2\sigma_{22} + F_{11}\sigma_{11}^2 + F_{22}\sigma_{22}^2 + F_{66}\sigma_{12}^2 + 2F_{12}\sigma_1\sigma_2 - 1 \leq 0 \quad (4)$$

$$F_1 = \frac{1}{X_T} + \frac{1}{X_C}, F_2 = \frac{1}{Y_T} + \frac{1}{Y_C}, F_{66} = \frac{1}{S_{12}^2}, F_{11} = -\frac{1}{X_T X_C}, F_{22} = -\frac{1}{Y_T Y_C} \quad (5)$$

Figure 5 – Tsai-Wu Criterion Failure Surface



Source: Developed by the author

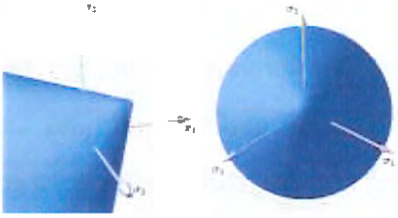
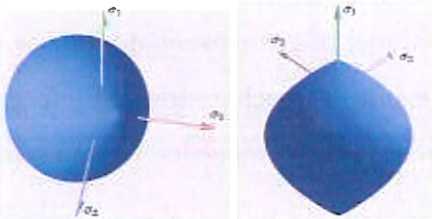
In particular, one of these coefficients –  $F_{12}$  – related to the shear in the failure plane was not mathematically proven to be unique, and as such, cannot be obtained experimentally. Several subsequent works, such as Wu e Stachurski (1984), Evans e Zhang (1987), Benzeggagha et al., (1995) were published with a focus in finding a mathematical expression or an experimental methodology to obtain  $F_{12}$ . However, several methods use as an estimative approximation for  $F_{12}$  the half of the geometric average  $F_{11}$  and  $F_{22}$ , which is the module of the maximum values of  $F_{12}$  that may be obtained by experimental tests, as proposed by Hashin (1980) and found in Equation 6.

$$F_{12} = -\frac{1}{2}\sqrt{F_{11}F_{22}} \quad (6)$$

In the following years, several authors used the same approach of creating a mathematical failure surface based on the invariants of anisotropic materials, altering the basic expression or adding new terms to include a given phenomenon of interest. As such, several works exist on the literature that adapt classic yielding failure surfaces for the use with composite materials, such as the Ducker-Prager yield surface (Drucker e Prager, 1952) commonly used for the polymeric matrix phases, or Bresler-Pister yield surface (Bresler e Pister, 1985) used for foam core in sandwich composites. This approach culminates in the use of Altenbach-Bolchoun-Kolupaev yield surface (Altenbach et al., 2013), which tries to

generalize an expression for multiple material types. Nowadays, these three criteria are most commonly used in microscale analysis for which the failure of each different heterogeneous phase is considered and non-linear behavior, such as polymeric matrix plasticity, is modelled, and the mathematical representation can be found in Table 1.

Table 1 – Other failure surfaces based criteria

Criteria	Mathematical Formulation	Failure Surface
Ducker-Prager	$\frac{m-1}{2}(\sigma_{11} + \sigma_{22}) + \frac{m+1}{2}\sqrt{ \sigma_{11}\sigma_{22} }$ $- X_C \leq 0, \quad m = X_C/X_T$	<p>Figure 6 – Ducker-Prager failure surface</p>  <p>Source: Adapted from Wikipedia (2017)</p>
Bresler-Pister	$X_C = \sqrt{ \sigma_{11}\sigma_{22} } - c_0 - c_1(\sigma_{11} + \sigma_{22}) - c_2(\sigma_{11} + \sigma_{22})^2,$ $c_1 = \frac{(X_T - X_C)}{X_T + X_C} \left( \frac{4X_B^2 - X_B(X_C + X_T) + X_C X_T}{4X_B^2 + X_B(X_C + X_T) - X_C X_T} \right)$ $c_2 = \left( \frac{1}{X_T + X_C} \right) \left( \frac{X_B(3X_T - X_C) - 2X_C X_T}{4X_B^2 + 2X_B(X_T - X_C) - X_C X_T} \right)$ $c_0 = c_1 X_C - c_2 X_C^2$	<p>Figure 7 – Bresler-Pister failure surface</p>  <p>Source: Adapted from Wikipedia (2017)</p>
Altenbach - Bolchoun-Kolupaev	$27I_2^3 \frac{1 + c - 3 \cos 3\theta + c_6 \cos^2 3\theta}{1 + c_3 + c_6}$ $= \left( \frac{\sigma_{eq} - \gamma_1 I_1}{1 - \gamma_1} \right)^{6-l-m} \left( \frac{\sigma_{eq} - \gamma_2 I_1}{1 - \gamma_2} \right)^l \sigma_{eq}$	<p>(Impossible to represent in the plane stress space)</p>

Source: Developed by the author

Gradually, during the 1970s, the failure criteria for composite materials started to grow more complex. Researches started to question the hypothesis used on the Tsai-Wu criterion and similar approaches of adapting anisotropic equations to create failure surfaces, in particular due to their inability to correct simulate the behavior of unidirectional composites (UD). Then, in 1980, Hashin (Hashin, 1980) introduced the idea to separate the different failure modes existing for the different phases of composite materials, altering Tsai-Wu's failure surface to a surface assembled "by parts", in which, for each different quadrant, and stress state values, different expressions and coefficients are used. This hypothesis is based on the fact that, for most common used fibers – glass and carbon –, the failure is brittle and in the direction normal to the fiber, as for the polymeric matrix, the failure may not occur in the direction of the fiber, but in a "critical plane" that is aligned in any direction.

This premise introduces different failure modes: failure of the polymeric matrix under compression and traction, and failure of the fibers under compression and traction. Even though several studies showed a good efficiency and consistency for the Hashin criterion when used for UD composites (Paris, 2001), there are some problems with the criterion. In particular, the experimental results of the strength values of the polymeric matrix in the direction of the "failure plane", as this direction varies with the material stress state. Several methodologies exist to obtain these coefficients, however, even nowadays, this is still a problem that may hamper or even invalidate the use of Hashin's criterion (Tita, 2008). Following Hashin's work, several researchers tried to improve his modelling in particular (Tita, 2003). Because of the introduced complexity, Hashin's criterion do not have a simple mathematical expression or given failure surface shape, as those depend on the angle of the critical plane, which by itself depends on the stress state of the material.

Expanding Hashin's idea, Puck in a sequence of several works (Puck and Schürmann, 1996; Puck et al. 2002 and Puck and Schürmann, 2002) introduced the concept of inter-fiber failure, by proposing a process to identify the "critical plane" of the polymeric matrix based upon the Cauchy stresses over this plane. Thus, the failure expressions for the polymeric matrix for Hashin's criterion were improved upon with the addition of four constants that describe the orientation of the matrix's failure plane. Using these constants, one may generate Puck's "master failure surface". Hence, Puck's full criterion is based on a quadratic expression containing seven constants – three strength values and four parameters for the orientation of



the failure plane –, and needs at least seven distinct experimental tests to obtain its parameters. The four constants used to obtain the failure plane are particularly difficult to obtain, demanding complex and low precision experimental tests (Angélico, 2009). Moreover, Puck's criterion along with all the aforementioned criteria are binary, predicting only the material final failure, and not calculating the damage evolution over the load or life of the structure. Some studies exist that tried to introduce a degenerating law for the criteria parameters or the material constants for Puck and/or Hashin for some specific load cases, for instance:

- Chang and Chang (1987a and 1987b) (Hashin, bending)
- Tita et al. (2008) (Hashin – low energy impact and bending)
- Daniel et al. (2012) (Hashin – bending)
- Batra et al. (2012) (Hashin – low energy impact e shear)
- Riccio et al. (2014) (Hashin, general impact)
- Angélico et al. (2009) (Puck – bending)
- Carraro e Quaresimin (2014) (Hashin – high energy impact and fatigue).

However, no general model that works consistently for any load case, laminate lay-up and analysis condition exist.

Trying to solve these problems, using an approach of different damage evolution occurring for different phenomena, Ladevèze (Ladevèze e LeDantec, 1996) found expressions for the evolution of damage with the load mathematically, and based upon the definition of Lemaitre (Lemaitre, 1996, Lemaitre and Desmorat, 2005) of thermodynamic forces. Three damage modes exists for Ladevèze's model: fiber brittle failure, matrix damage evolution and failure under either traction or compression, which evolve with the load, altering the constitutive matrix. These expressions are dependent on three damage constants –  $d_1$ ,  $d_2$ , and  $d_6$  –, which may be obtained from specific experimental tests (more simple than Puck's identification process) and a failure surface obtained from a quadratic expression based on strength values measured in a direction normal to the fiber reinforcements and under pure in-plane shear, as well as the stress components  $\sigma_2$  and  $\sigma_{12}$ .

Overall, the aforementioned criteria have some common limitations. First, the experiments to obtain the parameters need to generate the failure surfaces and/or expressions, which tend to be difficult to reproduce and shows low precision. Second, the separation of the several damage and failure mechanisms in different equations is not accounted for the simultaneity and interactions between these mechanisms. Finally, the use of failure surfaces adjusted from semi-empirical parameters, as several manufacturing and experimental errors may be carried over to the models (Talreja, 2014).

## 2.2 First damage threshold: Heterogeneous microscale

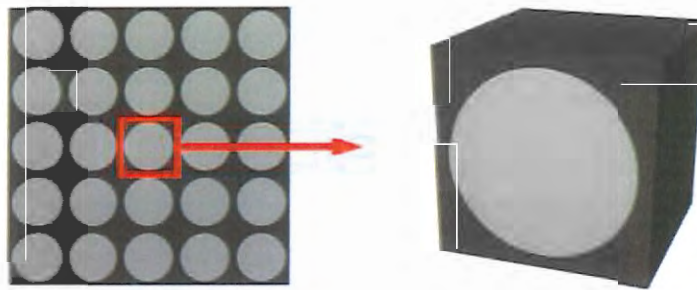
In general, the existing problems in multiscale analysis are related to the difficulties in modelling materials in the microscale due to its geometric complexity and the different damage mechanisms, which occur simultaneously and each needs a different mathematical model (Talreja, 2014). For instance, even for UD composites, the random dispersion of fibers inside the polymeric matrix introduces a numerical problem in the modelling due to the need of complex algorithms to calculate the positioning of the fibers (Yang et al., 2003). For weaved composite, bi or tridimensional, the challenge of obtaining precise information of the geometry of the fabric increases the problem. There are possible approaches that have been taken in works of the literature, which regard this issue (Huang, 2000; Barbero et al., 2005; Ha-Minh et al., 2011), but it is observed that this is still an open problem.

However, after the modelling barrier is handled, several approaches exist for the usage of multiscale analysis to evaluate damage evolution and failure in composite materials. Overall, the existing works in the literature uses multiscale analysis to include damage and failure mechanisms that are difficult or impossible to include in macroscale analysis. For instance: interface debonding between fiber and matrix, different constitutive behavior between each of the phases, the occurrence of different mechanisms in a simultaneous manner, and to model tridimensional effects that do not appear in a homogenized environment.

In particular, two concepts widely spread in the literature for the use of multiscale analysis consists on Unit Cells (UC) and Representative Volume Elements (RVE). Unit Cells can be defined as the smallest repeating volume that has a geometry that, through symmetry and

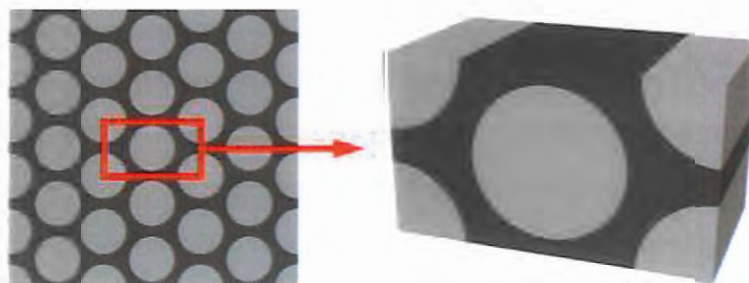
periodic boundary conditions, represents the whole heterogeneous material. For unidirectional composite materials this usually means repeating geometries containing a single or small amount of fibers, depending on the initial fiber distribution, that through the use of periodic boundary conditions may simulate the behavior of a material when repeated over a uniform grid (Figure 8), which shows uniform distributed singularities, such as fibers in a composite material (Asp et al., 1996). Examples of square and hexagon UCs for uniform fibers distributed in a composite structure can be seen in Figure 8 and Figure 9, respectively.

Figure 8 – Square Unit Cell



Source: Adapted from Wikipedia (2017)

Figure 9 – Hexagonal Unit Cell

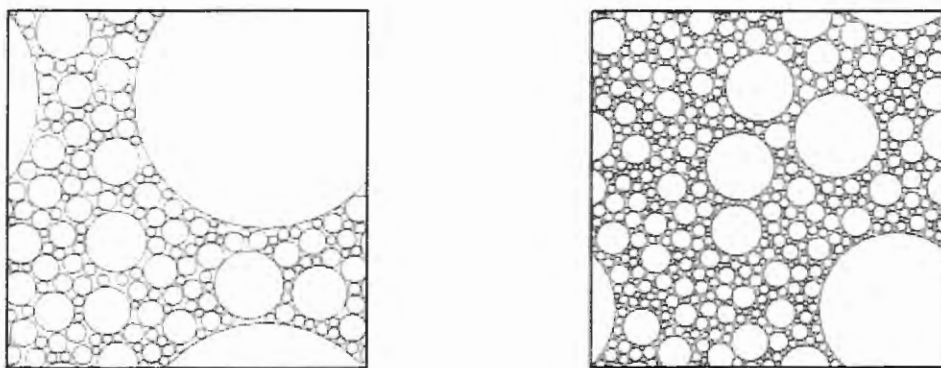


Source: Adapted from Wikipedia (2017)

Representative Volume Elements are volumes of realization of a material which statistically represent the material's thermomechanical behavior. For composite materials this means a random generated distribution of fiber positions and radii that can be obtained from

a statistical distribution with properties found from experimental data, such as microscopy or scanning electron microscopes, or correlated to given desired properties, such as fiber volume fraction, fiber clustering intensity and fiber clustering occurrence. It is important to note that RVEs do not necessarily need geometrical symmetry, repeating periodicity grids or be modelled with periodic boundary conditions as they, by definition, are already a statistical representation of a material volume. This fact however, only holds true provided that the statistical average behavior of the given area of the RVE that is being analyzed correctly simulates the physical behavior of the material and this area is not influenced by the boundary conditions of the model. Examples of RVEs for composite materials are shown in Figure 10.

Figure 10 – Examples of RVEs for composite materials.



Source: Adapted from Wikipedia (2017)

Another approach is to use cohesive elements together with different types of damage and failure models to simulate locally damage evolution or crack propagation. These cracked or damaged microstructures are used within homogenization techniques or global-local criteria to find the effective degenerated elastic, elastoplastic properties and/or strength of a structure. Cohesive elements may be used in conjunction with layer-wise shell finite element formulations to model delamination. This approach is specially indicated for some specific cases, such as modelling adhesive joints. However, the main disadvantage of cohesive models is the difficulty to find the parameters for the traction-separation laws.

In this context, some works are of interest to the present PhD Thesis. Prabhakar et al. (2013) employed a mesoscale approach with cohesive elements and diffuse damage theories to predict and simulate kink bands in cross-ply laminates and laminates with  $\pm 45^\circ$  layers under

compression. Vaughan and McCarthy (2011) used bi-dimensional analysis with plane-strain state elements and non-linear plastic constitutive laws to trace the crack path in 90° layers, and propagate these cracks via cohesive elements. In their work, the cracks could be nucleated from interface debonding failure between fiber and matrix, matrix failure or fiber failure. Murani and Upadhyad (2012) and Murari and Upadhyad (2013) used the same approach, but applying a Representative Volume Element (RVE), which contains a single fiber to obtain damage evolution over cyclic tensile loads. Shojaei et al. (2014) used hypothesis from linear elastic CDM with cohesive elements to evaluate damage evolution under tensile loads in cruciform UD coupons, considering brittle failure of both matrix and fiber. Yang et al. (2012) considered a similar approach, however including interface-debonding failure in the cracks nucleation.

Another possible approach is to use full 3D simulations of the microstructures to generate stress or strain field that feed the damage nucleation, evolution and failure calculations. However, this is a computationally expensive approach and, in general, is outside the scope of models applicable to complex structures (Maimi et al. 2010a).

### **2.3 Continuum fracture mechanics first damage threshold: Homogeneous microscale**

In general, material models neglect the inherent heterogeneity of composite materials, not in its formulations, but in the way damage metrics, such as local stress states are obtained and treated. This heterogeneity may cause several different failure mechanisms that occur simultaneously in different materials scales and phases.

One possible solution to this problem is to use and/or develop new damage and failure models based on multiscale analysis and physical failure mechanisms, as well as known continuum fracture and damage mechanics relations. Several works in this area already exist in the literature; however, most of them is focused in microstructural analysis, but the prediction and cause for the first failure phenomena. In particular, works that focus in the damage evolution of composites are dedicated on life analysis, including prediction of the fatigue limit and stress vs. number of cycles curves.

For the study of monotonic loads, the damage evolution models based upon continuous damage mechanics formulation are able to describe damage evolution in function of crack density and energy and/or displacement metrics from the cracks, such as energy needed to open new cracks and crack opening and sliding displacements. For instance, several works by the same group of researchers (Varna and Berglund, 1991; Varna et al., 1993; Varna et al., 1999) showed how damage caused by tensile loads in angle-ply composites –  $[0^\circ_\mu/\theta_v/\psi_o]_\Sigma$  lay-ups – may be modelled as multiple matrix cracks parallel to the direction of the fibers using the crack opening, sliding and density as damage metrics. Afterwards, Joffe et al. (2001) mathematically proved the hypothesis of reversibility in the damage modelled by matrix cracks, from which one can describe the energy necessary to double the amount of cracks from a given damaged state, and how to relate this energy with the average crack opening displacement for  $90^\circ$  layers.

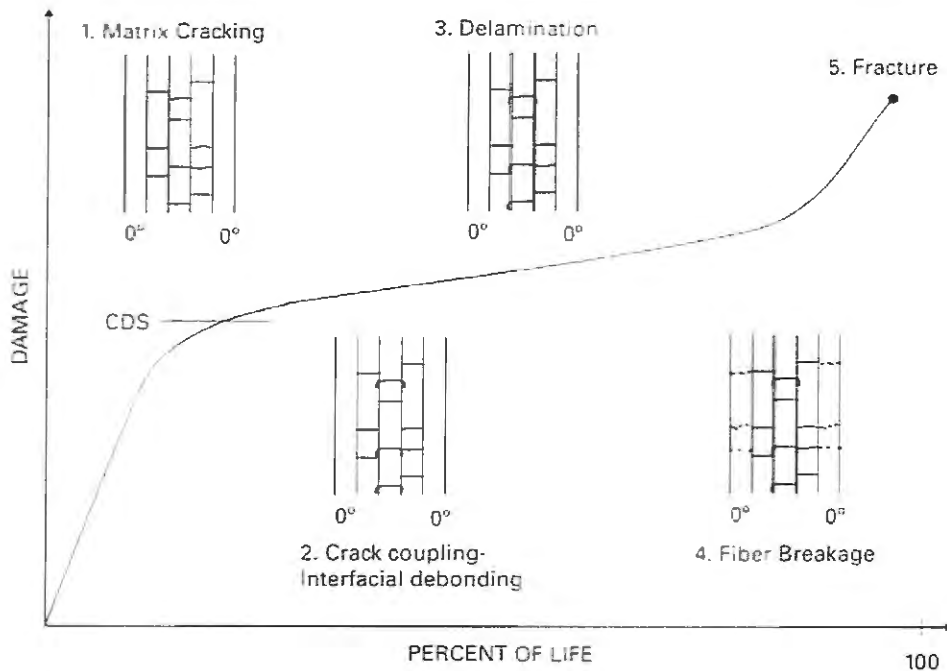
In addition, some works model either analytically or numerically the property degradation of composite materials as function of the crack density, such as the works of Joffe and Varna (1999), Hajikazemi et al. (2015), Barbero et al. (2015) and Barbero et al. (2016). Besides, the simplifications needed for an analytical solution implicate in specific kinds of lay-ups. In particular, existing analytical solutions uses either Navier or Levi's solution to solve the equilibrium equations of the laminate, and as such implicates that  $A_{16} = A_{26} = B_{16} = B_{26} = D_{16} = D_{26} = 0$  (Reddy, 2004). This situation only occurs in antisymmetric balanced lay-ups, which would invalidate the method for UD off-axis analysis, and  $\pm\theta$  lay-ups, or angle-ply. In addition, these works focus on the damage evolution of laminates containing single damaged  $90^\circ$  layer bundles. Benzerga et al. (2009) and Singh et al. (2010) improved upon the aforementioned works by combining both approaches, and applying it on some angle-ply laminates,  $[0^\circ_m/90^\circ_n/\theta_o]_S$  or  $[0^\circ_m/\theta_n/90^\circ_o]_S$ , using numerical solution for the degradation problem.

## 2.4 Damage evolution

As Figure 11 shows, the damage and failure mechanisms in composite materials follow a known evolution pattern. For example, delaminations tend to occur only after intralaminar damage is present and was already initiated. As such, a logical approach for the evolution of damage is important, as well. Figure 11 also shows how the largest response change in the stress-strain curve for composite materials occurs in the initial part of damage evolution, which mainly compromises intralaminar damage. In addition, most structural projects that use composite materials apply relatively large safety factors for structure designs, either from necessity originated from uncertainties in manufacture processes or from impositions given by different regulations and standards used in homologation processes. Together, these two factors can guarantee that designed structures will work in the first damage region of the curve. Thus, it makes sense for the present work to focus only on intralaminar damage. However, it is well known that some kinds of laminates and/or types of loadings (like impact) can show more delaminations and/or fiber breakage than intralaminar failures.

The main difference between the pure bending and the pure tensile load case is the formation of a non-uniform displacement field over the thickness of the laminate, due to the curvature imposed by bending loads (Maio et al., 2013). This fact creates a distribution of stress field over the thickness that may results in a stress state in which both traction and compression are found in the material. As such, different levels of stresses and strains exist over different layers of the composite, even those with the same orientation. Hence, layers closer to the bottom of a laminate under a right handed pure bending load display larger normal stresses and strains comparing to those closer to the middle, and layers closer to the top of the laminate display negative normal stresses and strain levels.

Figure 11 – General behavior of damage evolution in composite materials



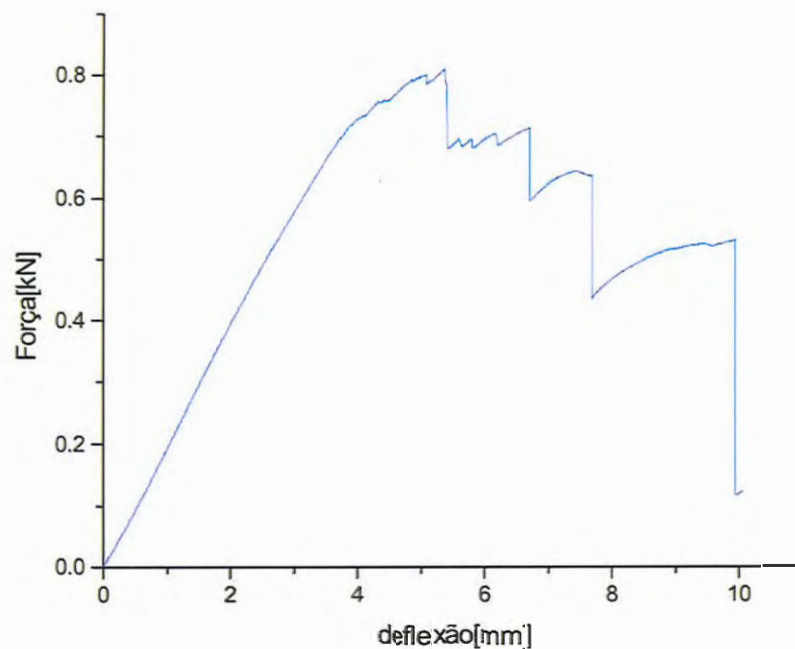
Source: Talreja (2016)

Under pure tensile loads, layers with the same orientation fail at practically the same time, and this leads to premature failure of other layers, which in turn leads to catastrophic failure of the material. However, under bending loads, the non-uniform distribution of displacements leads to a behavior known as progressive failure, in which different layers fail at different load levels (Batra et al., 2012). The general behavior of a composite structure under progressive damage shown by Figure 12 is exemplified by Tita (2003), which consists of a bending test of a  $[0^\circ/90^\circ/0^\circ/90^\circ/0^\circ]_S$  carbon fiber-epoxy laminate. In this test, the damage and failure history of a laminate under bending can be seen clearly. The mechanical behavior of the laminate, as previously discussed, is complex because of the interaction between different damage progression and failure mechanisms. However, the progressive behavior of damage and failure is easily identifiable. At first, about the 0.75 kN/3.5 mm point, crack nucleation and multiplication started at the bottommost  $90^\circ$  layers, as shown by the non-linearity induced in the curve in this load level. At the 0.85 kN/5.7 mm point, the first drop in force occurs, being characterized in the test by delamination close to the force applicator. The trend of increased non-linear response as more damage is accumulated in the  $90^\circ$  layers continues, until the second drop, corresponding to fiber failure of the bottommost  $0^\circ$  layer. These trends of



damage accumulation in 90° layers and failure, either by intralaminar fiber cracking in the 0° layers or delamination between the 0° and 90° layers continue until the final failure (Tita, 2003).

Figure 12 – Three point bending test of a  $[0^\circ/90^\circ/0^\circ/90^\circ/0^\circ]_s$  laminate showing progressive failure of the layers, highlighted by the red circles. Force [kN] vs. deflection [mm].



Source: Tita (2003)

Another important aspect to be highlighted is that the most of multiscale analysis of composite materials focus on fatigue life and in-plane loads where the damage can be induced by simpler and easier experimental setups. However, some works can be accounted for the progressive failure problem. Zhang and Zhang (2010) used the approach to alter the layer constitutive laws to include both an exponential and a “step function” property degeneration due to progressive failure under four point bending tests. Maio et al. (2013) used some bending predictions during analysis via Hashin based criterion for low energy impact loads. Ivančević and Smojver (2014) used a multiscale approach via several failure criteria for different phases and scales – Tsai-Hill, plane stress state Hashin, full 3D stress state Hashin and multi continuous theories – to simulate the damage caused by three point bending analysis. Meng et al. (2015) expanded the hypothesis of the classical laminate theory in a

multiscale simulation of 3D bending and concluded that the influence of out-of-plane efforts cannot be neglected. Xu et al. (2015) studied the fatigue life under bending problem, as well. Therefore, these are some scientific contributions about experimental observations and simulations of damage evolution in composite materials. Thus, in the next chapter, it will be shown how the present author decided to approach the problem of damage evolution in composite materials, focusing on intralaminar failures.

### 3 MULTISCALE METHODOLOGY

---

Given the objectives shown in Chapter 1.2 - Objectives, this chapter presents an overview of the scientific methodology used in the present PhD Thesis to develop the models and procedures that predict the intralaminar damage evolution of a composite laminate with UD fibers. As such, the main objective of the present work is to develop a methodology based on a computational procedure, using physically consistent concepts, that links the external loads applied to a given structure and the resulting damage is associated with this particular set of loads. This methodology is accomplished by the use of a multiscale approach.

At first, it is emphasized that there is no universal definition of damage (Talreja and Singh, 2016). Hence, for the present work, damage is defined as a collection of irreversible changes in the material caused by either physical or chemical phenomena resulted from the presence of external loads. Damage can happen in the nanostructure, as atomic bond breakage between polymer chains; in the microstructure, as several different mechanisms, such as fiber or matrix cracking. In the macroscale damage can be understood and modelled as a change in the material properties that dictates the material behavior, such as elastic properties, plasticity or residual resistance (Talreja and Singh, 2014). Damage by itself is a concept, and should not be confused with Damage Mechanics, which is the field of study of damage initiation and evolution, as well as its consequences on the response of a material and/or structural element to external loads.

The main premise of the present approach is that damage, based on Continuum Damage Mechanics (CDM) concepts, is modelled in the macroscopic scale by treating a damaged material as a homogenized material with degenerated elastic properties with lesser values than the ones found in the intact material (undamaged material). Meanwhile, in a microscale physically consistent, metrics such as crack density, crack profiles, crack opening and sliding displacements and different energy values, which are related to the external load level and subsequent damage, are calculated.

Keeping that in mind, Figure 13 shows the general scientific methodology behind the creation of the computational procedure, clearly highlighting the different scales – macro and microscales –the multiscale approach and the iterative process between both scales. Figure

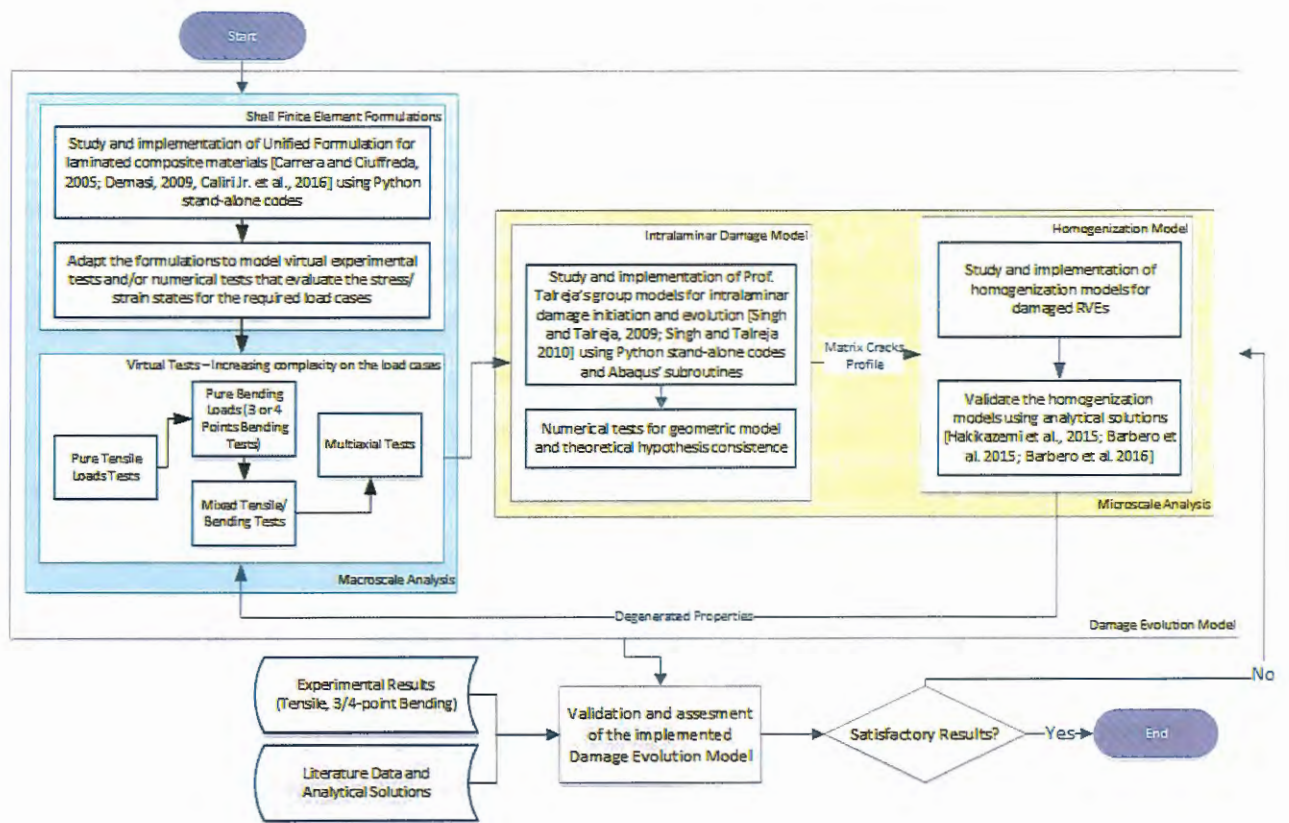
13 also highlights the main load cases of interest for the present work such as pure tensile loads, pure bending loads, mixed tensile-bending loads and multiaxial loads, which were studied in an increasing complexity manner.

In particular, it should be noted that, at first, the different models and theories applied to both the macroscale and microscale analysis were based on works found in the literature, such as Demasi (2009a), Singh and Talreja (2009), Singh and Talreja (2010), Danielson et al. (2006). However, due to the development of the present work, limitations of these theories were identified and studied. Consequently, these works were adapted and improved upon, generating new models, as some limitation of the original models prevented the integration with computational analysis or with the other models. The theoretical formulations, methodologies and results obtained for each model are shown in the following chapters.

Likewise, it is of interest to say that the linking of these different models in a single multiscale procedure is not trivial (Ladevèze and LeDantec, 1996), and may be seen, by itself, as an innovation made in the present PhD Thesis.

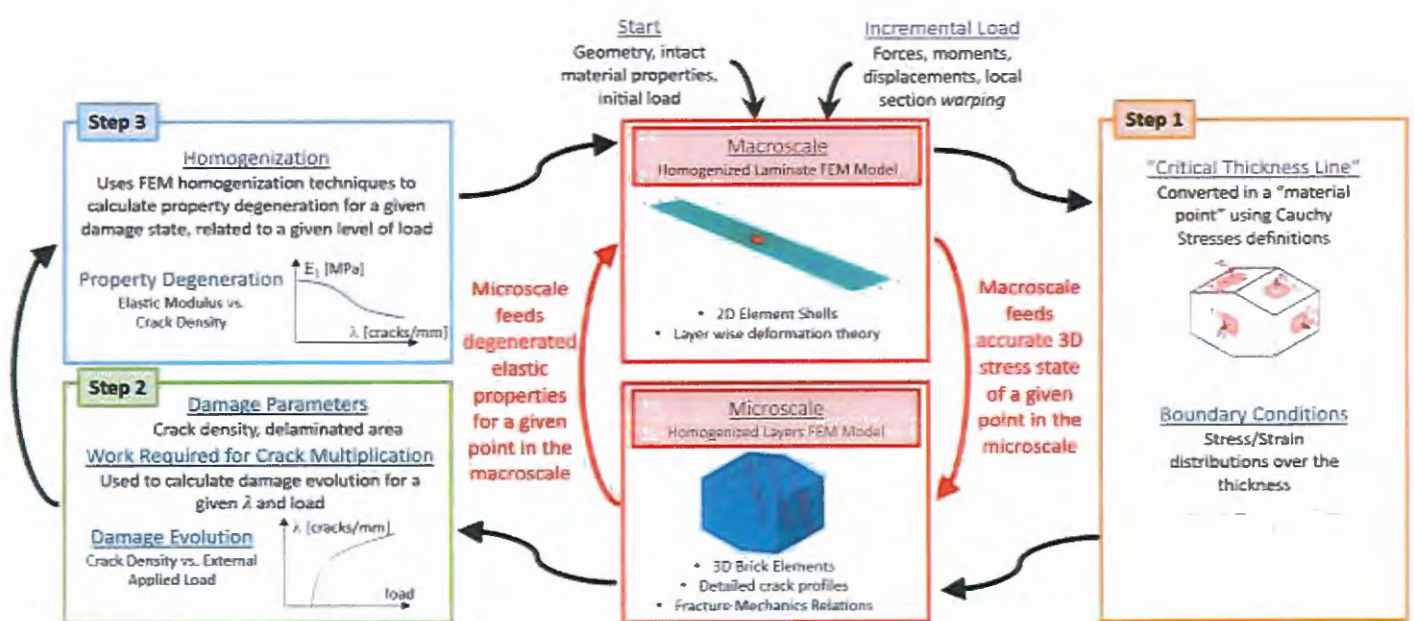
Figure 14 shows, schematically, the procedure developed in its current form. The basic premise of the methodology is that to evaluate the damage evolution of a given structure for a starting given level of load, the first phase of the methodology performs a macroscale finite element analysis to obtain the stress field, strain field and elastic deformation energy available at different points of the structure. This phase of the procedure can be compared to a virtual test, where different kinds of loadings can be applied on the composite structure. With this information, the methodology proceeds to a microscale model of selected critical points or regions on the structure, or points that are representative of the average stress state found in different materials points in the macroscale analysis. The microscale model is used to obtain, through CDM, the damage characteristics of the critical material point for that level of applied loading. Thus, it is calculated crack density, crack profile, crack opening displacements, crack sliding displacements, work done by opening and closing new cracks, and energy released by the creation of new cracks in the microscale model. These damage characteristics are used with homogenization techniques in order to obtain the degenerated elastic properties of that particular material point.

Figure 13 - Scientific methodology used on the present PhD Thesis



Source: Developed by the author

Figure 14 – Computational procedure developed in the present work



Source: Developed by the author



For this reason, the proposed procedure is composed by two separate phases – macroscale analysis and microscale analysis – with three different steps, each step utilizing different theoretical models:

- **Step 1:** Macroscale analysis for obtaining the through the thickness stress and strains distributions of a given point and the accumulated elastic deformation energy;
- **Step 2:** Microscale analysis for obtaining damage parameters, such as crack density, for that lay-up under the current load conditions (described by the stress distributions);
- **Step 3:** Microscale analysis for obtaining homogenized degenerated properties (layer-by-layer), given a certain level of damage described by the previously found damage parameters.

These three steps, while independent and having each its own development interact and supplement each other with information for every iteration of the methodology loop. For that, the procedure is separated into macroscale analysis for the prediction of accurate stress states, microscale analysis for the initiation and evolution of intralaminar damage (matrix cracks), and homogenization of the damaged material points for obtaining the degenerated homogenized elastic properties (layer-by-layer). For each of these analyses, the loads cases of pure tensile loads, pure bending loads, mixed tensile-bending loads and multiaxial loads, and, as such, are studied in a progressive order from the simplest (pure tensile load) to the more complexes.

### 3.1 Macroscale analysis methodology

As shown in Figure 14, the computational procedure is a closed iterative loop on the applied load and behaves as a predictor-corrector algorithm that is always one load step behind the solution. As such, for the loop to converge to accurate and satisfying results, the computational loop must be carried out in small load steps, even if individual steps converge for larger load steps.

In this computational loop, for every load step, a virtual test of a given laminate – the macroscale model – is made to obtain the stress and strain states at the most critical region

of the structure. For the uniaxial tensile and bending tests, this usually means the center region. For the pure tensile cases; the stress and strain tensors are usually uniform over the coupon, however, depending on the geometry of the structure and the applied loads, this stress and strain states are not be simple to predict. This fact occurs as, for most laminates, due to the lay-up the stress and/or strain states cannot be uniform, or not even purely tensile or in plane loading. Even unidirectional composites show a mixture of tensile and shear in-plane stresses for off-axis cases or angled-ply (non  $0^\circ$  or  $90^\circ$  layer). In particular, angled-ply show varying out-of-plane stresses and non-symmetrical laminates generally have a full 3D stress tensor due to the coupling of membrane and bending loads. In addition, damage incorporates asymmetry and unbalancing to the material, creating a full coupling of membrane, bending and shearing loads, further complicating the correct prediction of stresses, strains and accumulated elastic deformation energy. Besides, laminates with holes or tapered structures present full 3D stress state close to the stress concentration regions.

Moreover, the fact that the computational loop intrinsically needs small load increments to accurately predict damage can generate a large number of load steps per analysis. This makes computationally heavy simulations an issue. In light of all these facts, the macroscale step demands some particular characteristics for the model implemented for its simulations:

- Requires accurate prediction of the through the thickness distribution of stresses inside each layer, including the out-of-plane normal and shear stresses and strains;
- Requires correct simulation and prediction of general laminates, including angled-ply and asymmetric lay-ups;
- Requires relative low computational time, at least on the same order of magnitude of the time used in the microscale analysis phase;
- Due to the simple tests that are relevant to the load cases of interest for the present work, the implemented formulation can be simplified to only be applicable to flat rectangular and/or circular laminated plates.

For these reasons, given the costly computational of full 3D analysis that obtain accurate through the thickness stresses distributions, especially over bending (Reddy, 2004), and the limitations of most analytical solutions – i.e. antisymmetric laminates – the author

decided on the use of shell finite elements implemented using mapped rectangular and/or circular meshes.

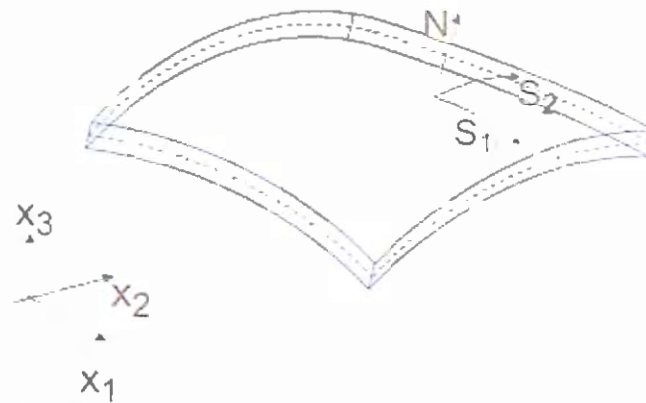
In particular, the main problem with existing analytical solutions is twofold. First, the existing analytical solutions for shell problems are usually obtained from either Navier's or Levi's type solution to solve the equilibrium equations of the laminate through trigonometrical series. These solutions exist only for the cases in which the laminate matrix parameters  $A_{16}, A_{26}, B_{16}, B_{26}, D_{16}, D_{26}$  are null (Reddy, 2004). The main problem arising from this fact is that only anti-symmetric lay-ups can be solved. As previously discussed, the progressive failure of different damage found in different layers due to bending or the lay-up may introduce asymmetry in problem. In addition, in general, analytical solutions are only possible for simple geometry like rectangular and radial ones. Finally, in future works, the present methodology could be expanded to include interlaminar damage, such as delaminations, to simulate low-energy non-penetrative impact load cases, which easier to be implemented and encompass broader boundary condition solutions using numerical approaches such as the FEM.

Shell finite elements are a family of "quasi-3D" finite elements (Figure 15). They are three-dimensional finite elements in the sense of being surfaces freely distributed in the space and having the capacity possessing tri-axial displacements and full stress/strain tensors compatibility. However, they are less computationally heavy than brick elements as the thickness characteristics degenerated into surfaces by the use of pre-described through the thickness displacement distribution functions (Bathe, 1996). These functions are called deformation theories, a huge amount existing on the literature, some being shown in Table 2.

In addition, this type of elements is more suitable to be model more complex surfaces and structures as usually applied in aircrafts. They are easily connected to beam elements, which normally represent reinforcements – such as stringers, ribs and spars – in more complex geometries. Moreover, shell elements are particularly well suited for simulating simple or double curved geometries, often found in the automobilist, aeronautical and aerospace industries



Figure 15 – Shell finite element



Source: Developed by the author

Table 2 – Shell deformation theories

Formulation	Deformation Theory
Classic Laminate Theory (Reddy and Ochoa, 1996)	$u_1(x, y, z) = u_1^0(x, y) - zu_{3,2}(x, y)$ $u_2(x, y, z) = u_2^0(x, y) - zu_{3,1}(x, y)$ $u_3(x, y, z) = u_3^0(x, y)$
First Order Shear Theory (Reddy and Ochoa, 1996)	$u_1(x, y, z) = u_1^0(x, y) - zu_1^1(x, y)$ $u_2(x, y, z) = u_2^0(x, y) - zu_2^1(x, y)$ $u_3(x, y, z) = u_3^0(x, y)$
Reddy's Plate (Reddy and Ochoa, 1996)	$u_1(x, y, z) = u_1^0(x, y) + z \left[ 1 - \frac{4}{3} \left( \frac{z}{h} \right)^2 \right] [u_1^1(x, y) + zu_{3,1}(x, y)]$ $u_2(x, y, z) = u_2^0(x, y) + z \left[ 1 - \frac{4}{3} \left( \frac{z}{h} \right)^2 \right] [u_2^1(x, y) + zu_{3,2}(x, y)]$ $u_3(x, y, z) = u_3^0(x, y)$
Murakami Zig-zag Theory (Reddy and Ochoa, 1996)	$u_1(x, y, z) = u_1^0(x, y) + zu_1^1(x, y) + (-1)^k u_1^k(x, y) z_k$ $u_2(x, y, z) = u_2^0(x, y) + zu_2^1(x, y) + (-1)^k u_2^k(x, y) z_k$ $u_3(x, y, z) = u_3^0(x, y)$
Ferreira Sine Theory (Ferreira et al., 2005)	$u_i(x, y, z) = u_i^0(x, y) + zu_i^1(x, y) + \sin\left(\frac{z\pi}{h}\right) u_i^3(x, y)$
Soldatos Hyperbolic Theory (Soldatos, 1992)	$u_1(x, y, z) = u_1^0(x, y) + \left[ z \cosh\left(\frac{z}{2}\right) - h \sinh\left(\frac{z}{h}\right) \right] u_1^1(x, y)$

	$u_2(x, y, z) = u_2^0(x, y) + \left[ z \cosh\left(\frac{1}{2}\right) - h \sinh\left(\frac{z}{h}\right) \right] u_2^1(x, y)$ $u_3(x, y, z) = u_3^0(x, y)$
Soldatos Unified Theory (Soldatos, 1993)	$u_1(x, y, z) = u_1^0(x, y) - zu_{3,1}^0(x, y) + F_1^k(z)u_1^k(x, y)$ $u_2(x, y, z) = u_2^0(x, y) - zu_{3,2}^0(x, y) + F_2^k(z)u_2^k(x, y)$ $u_3(x, y, z) = u_3^0(x, y)$
Carrera's Unified Theory (Carrera and Ciuffreda, 2005)	$u_i(x, y, z) = F_k(z)u_{ik}(x, y)$
Demasi's Generalized Unified Theory (Demasi, 2009a)	$u_i(x, y, z) = F_{ki}(z)u_{ik}(x, y)$
Caliri's Generalized Unified Theory (Caliri et al. 2017)	$u_i(x, y, z) = F_{ki}(z)u_{ik}(x, y) + G_{ki}(z)u_{ik,j}(x, y) +$ $H_{ki}(z)u_{ik,jl}(x, y)$

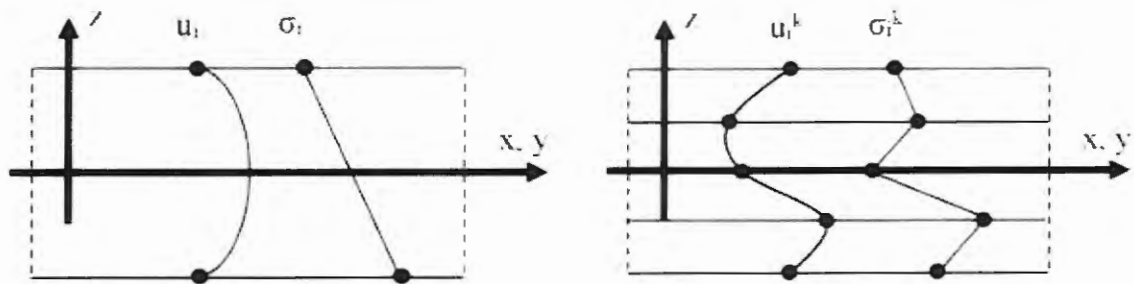
Source: Developed by the author

Given the necessary accuracy of the stresses for the correct use of boundary conditions on the microscale phase of the methodology, several shell deformations theories were studied, and the unified formulations (Carrera and Ciuffreda, 2005, Demasi, 2009a, Caliri et al. 2017) were chosen as the optimal candidates basis for the implemented macroscale formulation. The unified formulation describe the main variables of the problem – displacements in the case of classic solutions, displacements and out-of-plane stresses in the case of mixed solutions – mathematically through a sum of linear-independent terms, multiplied by generic functions over the thickness. They are called unified formulations for having procedures to change these functions and variables at will, generalizing the deformation functions (Ferreira et al., 2011).

In particular, unified formulations exist in the literature for both Equivalent Single Layer (ESL) and Layer-Wise (LW) formulations (Qatu et al., 2010). ESL formulations treat the laminated shells as a single homogeneous equivalent material, whose displacement distributions are homogenized through the thickness in a single function. These distributions of displacements and secondary variables (such stresses and strains) are obtained from variables that describe the quantities as they appear in a given reference surface, usually taken as the top, bottom or mid-surfaces of the laminate. LW formulations, on the other hand, describe the through the thickness distributions using several degrees of freedom for the top

and bottom boundaries of each layer of the laminate, using pre-determined functions only to interpolate the variables inside each layer. Figure 16 schematically shows the differences between ESL and LW formulations.

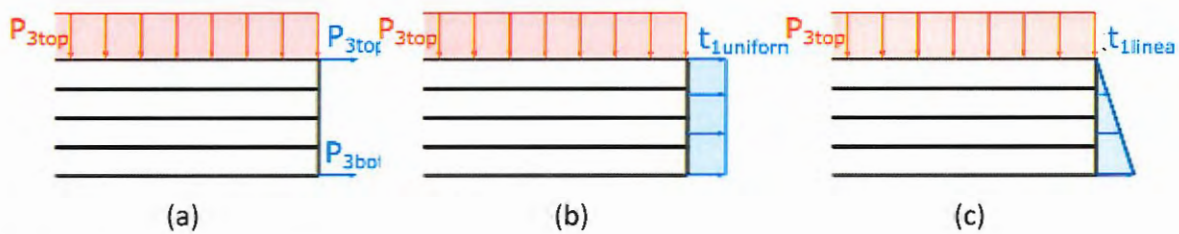
Figure 16 – Schematic difference between ESL theories (left) and LW theories (right)



Source: Caliri et al., 2016

Given that the distribution of stresses, strains and elastic deformation energy through the thickness of the laminate are requirements for the macroscale analysis of the damage evolution procedure. Based on recommendations and studies found on the literature of several authors (Carrera and Ciuffreda, 2005, Demasi, 2009, Qatu, 2010, Ferreira, 2011, Caliri, 2017), LW formulations were chosen for the present work. Another advantage of LW formulations is that the boundary conditions are more generalized than their counterpart in ESL formulations. For example, for tensile loads, the application of pressures can be made such as they exist only in the top or bottom layers, simulating claws (Figure 17a), through the whole thickness, simulating forces from external bodies (Figure 17b), and with different distributions, simulating the working internal stresses of different layers (Figure 17c). These different possibilities for the application of loads are schematized in Figure 17 and represent the potentialities of LW formulations regarding external load application and boundary conditions.

Figure 17 – Different types of applied loads in laminates compatible with unified theories



Source: Developed by the author

Another approach about the macroscale analysis, that was chosen, regards the use of mixed shell finite element formulations. Mixed formulation expand the problem variables from only using the displacements to include the out-of-plane stresses. That is, while the variables describing the mechanical behavior of a shell in the classic formulations are the  $u_1$ ,  $u_2$  and  $u_3$  displacements, in mixed formulations the out-of-plane stresses  $\sigma_{23}$ ,  $\sigma_{13}$  and  $\sigma_{33}$  are also taken as variables of the problem (Demasi, 2009b). This is made as, due to the boundary conditions of null out-of-plane shear stresses in the top and bottom of shells, these stresses are usually the ones, which need higher-order polynomials to be correctly predicted, avoiding numerical problems such as Shear Locking (Bathe, 1996). In particular, depending on the problem parameters, such as the structure and element dimension per thickness aspect ratio and the type of integration methods used for the thickness direction, a good choice of a high-order theory may mitigate or negate the Shear Locking problem. However, depending on different factors, it may still occur and techniques such as reduced or selective integration may still be needed.

By setting the stresses as independent variables and using Reissner's Mixed Variational Theorem (RMVT) as the main equilibrium equations, it is possible to pick high-order polynomials for only these stresses, using less computational costly functions for the displacements. Furthermore, these formulations avoid the need of making derivatives in relation to the thickness direction. These facts contribute to the computational effectiveness of these theories and, under some circumstances, creates faster simulations than its classic counterparts, even considering the increased number of variables in the final system of equations.

For these reasons, both classic and mixed formulations were used in the macroscale analysis, considering studies over which one held the most advantages being made. The adapted Unified Formulations were coded using an in-house Python code. In fact, Python was chosen as the programming language due to the capacity of being interpreted within Abaqus, which could be used to link with the microscale analysis.

### 3.2 Microscale analysis methodology

Based on data obtained for the macroscale analysis of stresses, strains and elastic deformation energy for a given point and a given load level, the microscale analysis should predict the damage associated to the calculated metrics, and homogenize this damage in degenerated elastic properties layer-by-layer.

A microscale model containing physically consistent damage is created for each material point identified in the macroscale as a candidate for damage initiation or propagation. For the base model that is proposed, all intralaminar damage contained in a given layer is modelled as trespassing cracks through a homogenized orthotropic material that follows the fiber directions. In the Chapter 5, there will be highlights and discussions about the reasons for this way of modelling. However, in summary, other damage modes, such as fiber-matrix debonding and fiber bridging contribute only to the earliest stages of damage initiation, and not damage evolution.

This argument is especially important to discard inelastic effects in the matrix. In the most commonly used polymeric matrixes in composite materials, such as epoxy, PPS and PEEK, which are the focus of the present work, the maximum hydrostatic energy supported by the material is higher than the maximum deviatoric energy. This fact summed with the geometry and constraints implied by the fibers, inelastic effects in the matrices may only contribute to the first incidence of damage in “matrix rich areas”, where due to non-uniform distribution of fibers, some fibers are far away from each other in an enough distance that the shear effects are dominant (Elnekhaily and Talreja, 2017). However, in composite with high volume fraction of fibers (>40%), “matrix rich areas” are rare. Also, after this contribution occurs and initiates damage, cracks will grow, multiply and dominate the composite behavior, and further

incidences of inelastic behavior may be ignored. So, intrinsically, inelastic effects with damage evolution is low, and they can be disregarded in these kinds of matrices. As such, for simplicity sake, all intralaminar damage inside a given lamina is taken as cracks without inelastic effects (Talreja and Singh, 2014).

The selection of candidate points for damage depends on the current situation of the analysis, which is related if the current load level initiates damage at some point of the structure or not. In the cases when no previous damage is found, the candidate points are taken as the group that shows the highest deformation energy. More than one point may be taken candidates for damage as, depending on the geometry and boundary conditions of the problem, a set of points over the whole structure may present the same, or approximately the same level of deformation energy. Once the first set of points taken as damage candidates nucleates damage by having absorbed to a set level of deformation energy that leads to damage initiation, this set of points is taken to be permanently damaged and enters an evolution phase. During this evolution phase, the elastic properties for this groups of points in the structure degenerates as damage progresses. This degeneration of properties rebalances the stress distribution in the neighborhood, which may lead to a different group of points to get to an energy deformation level that initiates damage, as such a loop analysis has to be made until all the possible damaged points are identified. If no new points are identified to nucleate damage due to the stress redistribution, the current load step, and as such the external applied load, increases.

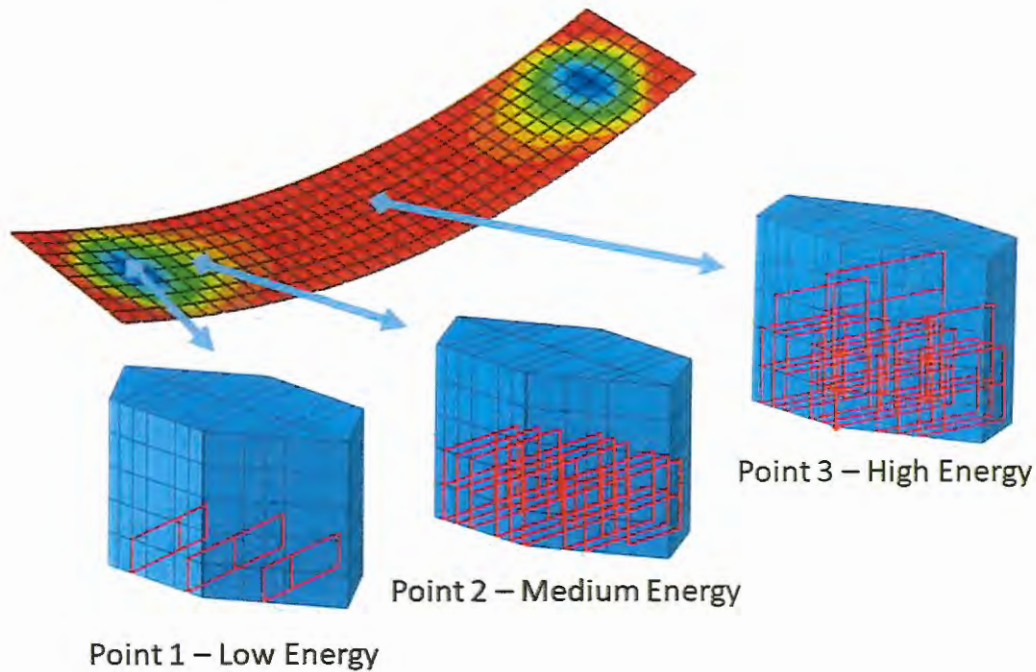
The stress state for these points is used as boundary conditions to a finite element analysis of a full 3D model, which considers homogenized layers and trespassing cracks. This microscale model can be seen as a RVE (Representative Volume Element) for that particular material point, depending on the definition for RVE used. However, it is not a representation of the whole material or structure, but actually a model of that particular material point immediate vicinity as it would be if the whole structure was subjected to uniform damage. In this regard, each microscale model associated to a macroscale point can be understood as a representation of the physical behavior of damage of a material that has uniformly distributed damage. In actuality, this microscale model does not follow the formal concept of a RVE – a model that statistically represents the macroscale material behavior –, but can be interpreted as a material point from which the stresses tensors are able to be represented into Cauchy

Stress Vectors over the model faces, and homogenized damage modelled as intralaminar cracks are observed. In this way, the model will create RVEs that represent the behavior of that single point, no matter its dimension, and its neighbor points will have different RVEs that represent themselves. Figure 18 schematically clarifies this approach.

A second way of understanding this concept is through the comparison to the equilibrium of a free body cuts. Each 3D model of what is called in the present work as RVE is an expanded volumetric representation of a “Free Point” or a “Representative Point” of the structure at a material level in that given point. The reason that point needs to be expanded in a representative volume is so that the stress state can be correctly applied using different polyhedral faces as Navier type boundary conditions for different Cauchy stress vectors acting in those faces.

At first, this approach ignores that damage cannot be uniformly distributed in the structure and the interaction of the different damage modes of neighboring regions. However, due to the boundary conditions of each RVE being the stress/strain distributions for that particular material point, each point is actually being modelled with all the influences of its neighboring region. A simple way to understand this fact is to interpret this approach as if each “RVE” is actually the differential representation of that point used in Cauchy’s Stresses definitions, but given a large enough dimension that damage is physically incorporated in this model.

Figure 18 – Approach of modelling each material point with a different “RVE” considering different amounts of damage, dependent on the deformation energy available at the material point



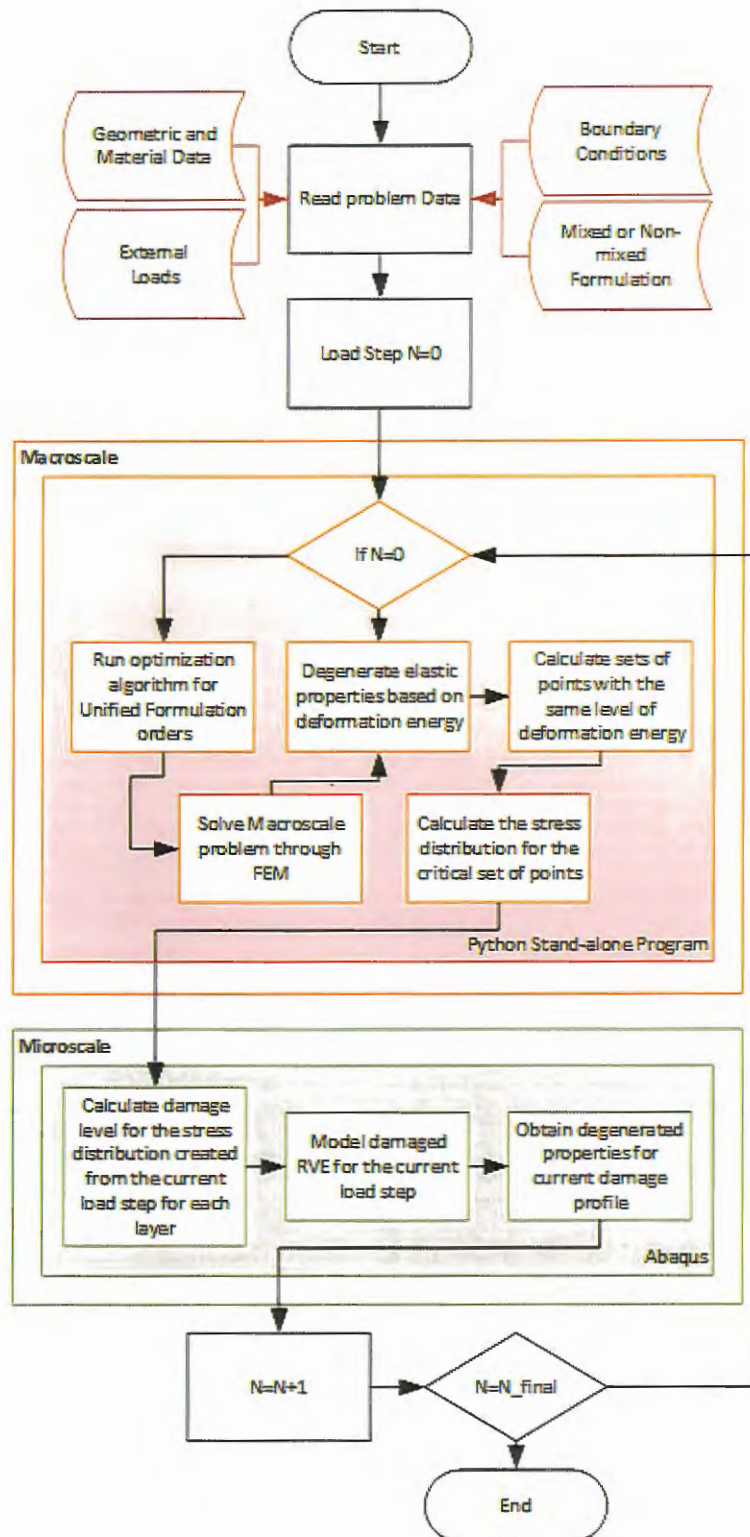
Source: Developed by the author

The proposed RVE is used to feed damage metrics such as crack opening displacements, crack sliding displacements and energy released by the formation of new cracks into models based on Continuum Damage Mechanics (CDM) such as the ones proposed by (Varna and Joffe, 1999, Singh and Talreja, 2010). These theories model intralaminar damage as only matrix cracks, and are used as a base to obtain the level of damage that particular point will show for the given load step. With the damage profile of the laminate obtained – i.e. crack density for each layer of the laminate – a homogenization algorithm for this particular damage instance is used to obtain degenerated elastic properties of each layer (i.e. layer-by-layer), which is then used to feed the next load step in the macroscale analysis.

The methodology implementation, including the integration between Python stand-alone (macroscale analysis) and Abaqus™ (microscale analysis), is shown in the flowchart in Figure 19.



Figure 19 – Methodology implementation flowchart





## 4 MACROSCALE MECHANICAL MODELS: SHELL THEORIES

---

This chapter presents the models and formulations used in the macroscale analysis phase of the proposed methodology, as well as details about its implementation. That is the finite element formulations used and implemented in stand-alone Python scripts for the simulation of accurate stress and strain distribution through the thickness of general laminates under different types of loads of interest. As previously discussed in Chapter 3. Multiscale Methodology, the author decided to use implementations for normal and mixed shell element formulations based on Demasi's GUF (Generalized Unified Formulation) and compare the results obtained for both. An important note is that the results obtained from such models do not need to be validated, as the general model was previously validated in the literature, neither it needs to be able to simulate edge cases such as extreme aspect ratios, as that falls outside the scope of the objective of the present work.

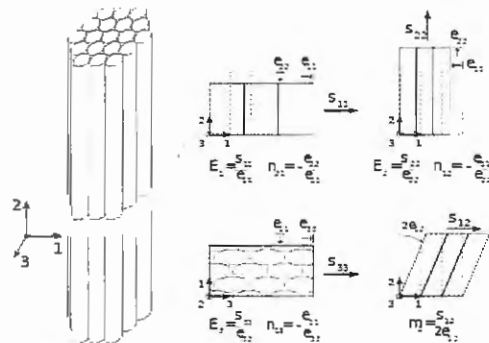
With this in mind, this chapter starts by presenting the constitutive equations for laminas of composite material used in both normal and mixed formulations, an overview of different classic shell deformation theories and its relation to the unified formulations. Following that, the adapted GUF for both normal and mixed formulations. Thereupon, the chapter shows the adaptations for the solution through the FEM for the formulations, which were implemented in the present work, including studies of different boundary conditions applications and the algorithm for finding the optimal deformation theory for a given case. Finally, the chapter ends with validation and results, comparing different formulations.

### 4.1 Composite constitutive equations

For most applications and structural analysis, a structural lamina manufactured from unidirectional fibers may be modeled as a transversal isotropic material, i.e. a material which behaves the same way in the 1 and 3 directions than in the 2 direction (orientations according to Figure 20). Equation 7 gives the constitutive equation for a transversal isotropic material.

$$\begin{Bmatrix} \sigma_{11} \\ \sigma_{22} \\ \sigma_{12} \\ \sigma_{13} \\ \sigma_{23} \\ \sigma_{33} \end{Bmatrix} = \begin{bmatrix} C_{11} & C_{12} & 0 & 0 & 0 & C_{13} \\ C_{12} & C_{22} & 0 & 0 & 0 & C_{23} \\ 0 & 0 & C_{66} & 0 & 0 & 0 \\ 0 & 0 & 0 & C_{55} & 0 & 0 \\ 0 & 0 & 0 & 0 & C_{44} & 0 \\ C_{13} & C_{23} & 0 & 0 & 0 & C_{33} \end{bmatrix} \begin{Bmatrix} \epsilon_{11} \\ \epsilon_{22} \\ \gamma_{12} \\ \gamma_{13} \\ \gamma_{23} \\ \epsilon_{33} \end{Bmatrix} \quad (7)$$

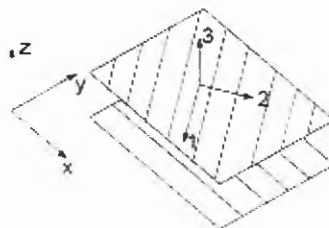
Figure 20 – Transversal Isotropic Material



Source: Adapted from Wikipedia (2017)

Due to the anisotropy of the material, the fiber orientation may not be aligned to the axis of the coordinate system, which results in the rotation of the matrix found in Equation 7 to the one found in Equation 8, with its explicit elements described in Equation 8 to 21. In the following equations,  $s$  represents  $\sin \theta$ ,  $c$  represents  $\cos \theta$  and  $\theta$  represents the angle of rotation of the fiber orientation for a given layer in relation to the global axis (x-y-z), as shown in Figure 21.

Figure 21 – Lamina coordinate system rotation



Source: Ribeiro et al., 2012

$$\begin{Bmatrix} \sigma_{xx} \\ \sigma_{yy} \\ \sigma_{xy} \\ \sigma_{xz} \\ \sigma_{yz} \\ \sigma_{zz} \end{Bmatrix} = \begin{bmatrix} \bar{C}_{11} & \bar{C}_{12} & \bar{C}_{16} & 0 & 0 & \bar{C}_{13} \\ \bar{C}_{12} & \bar{C}_{22} & \bar{C}_{26} & 0 & 0 & \bar{C}_{23} \\ \bar{C}_{16} & \bar{C}_{26} & \bar{C}_{66} & 0 & 0 & \bar{C}_{36} \\ 0 & 0 & 0 & \bar{C}_{55} & \bar{C}_{45} & 0 \\ 0 & 0 & 0 & \bar{C}_{45} & \bar{C}_{44} & 0 \\ \bar{C}_{13} & \bar{C}_{23} & \bar{C}_{36} & 0 & 0 & \bar{C}_{33} \end{bmatrix} \begin{Bmatrix} \varepsilon_{xx} \\ \varepsilon_{yy} \\ \gamma_{xy} \\ \gamma_{xz} \\ \gamma_{yz} \\ \varepsilon_{zz} \end{Bmatrix} \quad (8)$$

$$\bar{C}_{11} = c^4 C_{11} + 2scC_{12} + s^4 C_{22} + 4s^2 c^2 C_{66} \quad (9)$$

$$\bar{C}_{12} = s^2 c^2 C_{11} + s^4 C_{12} + c^4 C_{12} + s^2 c^2 C_{22} - 4s^2 c^2 C_{66} \quad (10)$$

$$\bar{C}_{16} = sc^3 C_{11} + s^3 c C_{12} - sc^3 C_{12} - s^3 c C_{22} - 2sc^3 C_{66} + 2s^3 c C_{66} \quad (11)$$

$$\bar{C}_{13} = c^2 C_{13} + s^2 C_{23} \quad (12)$$

$$\bar{C}_{22} = s^4 C_{11} + 2s^2 c^2 C_{12} + c^4 C_{22} + 4s^2 c^2 C_{66} \quad (13)$$

$$\bar{C}_{26} = s^3 c C_{11} + sc^3 C_{12} - s^3 c C_{12} - sc^3 C_{22} + 2sc^3 C_{66} - 2s^3 c C_{66} \quad (14)$$

$$\bar{C}_{23} = s^2 C_{13} + c^2 C_{23} \quad (15)$$

$$\bar{C}_{66} = s^2 c^2 C_{11} - 2s^2 c^2 C_{12} + s^2 c^2 C_{22} + c^4 C_{66} - 2s^2 c^2 C_{66} + s^4 C_{66} \quad (16)$$

$$\bar{C}_{36} = scC_{13} - scC_{23} \quad (17)$$

$$\bar{C}_{55} = c^2 C_{55} + s^2 C_{44} \quad (18)$$

$$\bar{C}_{45} = scC_{55} - scC_{44} \quad (19)$$

$$\bar{C}_{44} = s^2 C_{55} + c^2 C_{44} \quad (20)$$

$$\bar{C}_{33} = C_{33} \quad (21)$$

Composite lamina constitutive equations can be written in different forms depending on the chosen independent and dependent variables. For a mixed formulation, both the constitutive and equilibrium are changed from the aforementioned commonly used ones. The constitutive equation must be manipulated such as the membrane stresses  $-\sigma_{xx}$ ,  $\sigma_{yy}$  and  $\sigma_{xy}$  – and out-of-plane strains and distortions  $-\varepsilon_{zz}$ ,  $\gamma_{xz}$  and  $\gamma_{yz}$  – are obtained in function of its counterparts. To use this approach for composite materials, one must start with the rotated orthotropic constitutive equation found in Equation 8. This equation can be written in a condensed form, found in Equation 22, by separating membrane (represented by subscript m) and out-of-plane terms (represented by subscript s). From this, it is possible to write the “mixed formulation constitutive equation” (Demasi 2009) as shown in Equation 23 to 25. For simplicity, the terms are renamed using the letter  $Q$  as shown in Equation 26.

$$\begin{Bmatrix} \sigma_m \\ \sigma_s \end{Bmatrix} = \begin{bmatrix} \tilde{C}_{mm} & \tilde{C}_{ms} \\ \tilde{C}_{ms}^T & \tilde{C}_{ss} \end{bmatrix} \begin{Bmatrix} \varepsilon_m \\ \varepsilon_s \end{Bmatrix} \quad (22)$$

$$\begin{aligned} \sigma_m &= \{\sigma_{xx} \quad \sigma_{yy} \quad \sigma_{xy}\}^T, \quad \sigma_s = \{\sigma_{xz} \quad \sigma_{yz} \quad \sigma_{zz}\}^T \\ \varepsilon_m &= \{\varepsilon_{xx} \quad \varepsilon_{yy} \quad \gamma_{xy}\}^T, \quad \varepsilon_s = \{\gamma_{xz} \quad \gamma_{yz} \quad \gamma_{zz}\}^T \end{aligned} \quad (23)$$

$$\begin{aligned} \sigma_m &= (\tilde{C}_{mm} - \tilde{C}_{ms}\tilde{C}_{ss}^{-1}\tilde{C}_{ms}^T)\varepsilon_m + \tilde{C}_{ms}\tilde{C}_{ss}^{-1}\sigma_s \\ \varepsilon_s &= \tilde{C}_{ss}^{-1}\sigma_s - \tilde{C}_{ss}^{-1}\tilde{C}_{ms}^T\varepsilon_m \end{aligned} \quad (24)$$

$$\begin{Bmatrix} \sigma_{xx} \\ \sigma_{yy} \\ \sigma_{xy} \\ \gamma_{xz} \\ \gamma_{yz} \\ \varepsilon_{zz} \end{Bmatrix} = \begin{bmatrix} \bar{C}_{11} - \frac{\bar{C}_{13}^2}{\bar{C}_{33}} & \bar{C}_{12} - \frac{\bar{C}_{13}\bar{C}_{23}}{\bar{C}_{33}} & \bar{C}_{16} - \frac{\bar{C}_{13}\bar{C}_{36}}{\bar{C}_{33}} & 0 & 0 & \frac{\bar{C}_{13}}{\bar{C}_{33}} \\ \bar{C}_{12} - \frac{\bar{C}_{13}\bar{C}_{23}}{\bar{C}_{33}} & \bar{C}_{22} - \frac{\bar{C}_{23}^2}{\bar{C}_{33}} & \bar{C}_{26} - \frac{\bar{C}_{23}\bar{C}_{36}}{\bar{C}_{33}} & 0 & 0 & \frac{\bar{C}_{23}}{\bar{C}_{33}} \\ \bar{C}_{16} - \frac{\bar{C}_{13}\bar{C}_{36}}{\bar{C}_{33}} & \bar{C}_{26} - \frac{\bar{C}_{23}\bar{C}_{36}}{\bar{C}_{33}} & \bar{C}_{66} - \frac{\bar{C}_{36}^2}{\bar{C}_{33}} & 0 & 0 & \frac{\bar{C}_{36}}{\bar{C}_{33}} \\ 0 & 0 & 0 & \frac{\bar{C}_{55}}{\bar{C}_{44}\bar{C}_{55} - \bar{C}_{45}^2} & \frac{\bar{C}_{45}}{\bar{C}_{44}\bar{C}_{55} - \bar{C}_{45}^2} & 0 \\ 0 & 0 & 0 & \frac{\bar{C}_{45}}{\bar{C}_{44}\bar{C}_{55} - \bar{C}_{45}^2} & \frac{\bar{C}_{44}}{\bar{C}_{44}\bar{C}_{55} - \bar{C}_{45}^2} & 0 \\ -\frac{\bar{C}_{13}}{\bar{C}_{33}} & -\frac{\bar{C}_{23}}{\bar{C}_{33}} & -\frac{\bar{C}_{36}}{\bar{C}_{33}} & 0 & 0 & \frac{1}{\bar{C}_{33}} \end{bmatrix} \begin{Bmatrix} \varepsilon_{xx} \\ \varepsilon_{yy} \\ \gamma_{xy} \\ \sigma_{xz} \\ \sigma_{yz} \\ \sigma_{zz} \end{Bmatrix} \quad (25)$$

$$\begin{Bmatrix} \sigma_{xx} \\ \sigma_{yy} \\ \sigma_{xy} \\ \gamma_{xz} \\ \gamma_{yz} \\ \varepsilon_{zz} \end{Bmatrix} = \begin{bmatrix} Q_{11} & Q_{12} & Q_{16} & 0 & 0 & Q_{13} \\ Q_{12} & Q_{22} & Q_{26} & 0 & 0 & Q_{23} \\ Q_{16} & Q_{26} & Q_{66} & 0 & 0 & Q_{36} \\ 0 & 0 & 0 & Q_{55} & Q_{45} & 0 \\ 0 & 0 & 0 & Q_{45} & Q_{44} & 0 \\ -Q_{13} & -Q_{23} & -Q_{36} & 0 & 0 & Q_{33} \end{bmatrix} \begin{Bmatrix} \varepsilon_{xx} \\ \varepsilon_{yy} \\ \gamma_{xy} \\ \sigma_{xz} \\ \sigma_{yz} \\ \sigma_{zz} \end{Bmatrix} \quad (26)$$

## 4.2 Overview of shell deformation theories and shear locking

For the macroscale model, as previously discussed on Chapter 3, the desired output are accurate distributions of stresses and strains through the thickness of the laminate and accumulated elastic deformation energies, different authors from the literature Reddy and Ochoa (2000), Carrera and Ciuffreda (2005), Qatu (2010) and Ferreira (2009) recommend higher order theories. In particular, unified formulations such as Soldatos' Unified Formulation (1993), Carrera's Unified Formulation (Carrera and Ciuffreda, 2005), Demasi's Generalized Unified Formulation (Demasi, 2009) or Caliri's Generalized Formulation (Caliri et al., 2016, Caliri et al., 2017) offer a simple way to generate high order theory in a fast and systematically way for both ESL and LW formulations. However, most of these formulations, as found in the literature, are based on axiomatic deformation theories. Thus, by only having polynomials as through the thickness functions, this offers limitations to the cases where shear locking may happen (Bathe, 1996) and to implement the boundary condition of null out-of-plane stresses over the top and bottom of the shell boundary conditions. Shear locking is the virtual increase of shear stiffness that may occur in plate and shell elements due to the incapacity of low-order displacement based elements to correctly simulate the shear strains behavior. As Bathe (1996, p. 424-425) put:

*"[...] the basic difficulty is that spurious shear stresses are predicted with the displacement based elements. These spurious shear stresses result in a strong artificial stiffening of the elements as the thickness/length ratio decreases. This effect of shear locking is more pronounced for low-order element because, simply, the error in the shear stresses is larger. To arrive in reliable plate bending elements, the pure displacement-based formulation must be extended, and a successful approach is to use a mixed interpolation of transverse displacement, section rotation and transverse shear."*

These limitations emerge due to the incapacity of unified formulations to use the variables in different order terms. For example, for Reissner-Mindlin shells Equation 27 and

28, the shear locking and out-of-plane stresses boundary conditions are usually forced either through reduced integration, selective integration, or by including a parabolic distribution for the out-of-plane distortions Equation 29 (Bathe, 1996). From the author's previous experience with unified formulations, these three solutions are both hard to implement in a unified formulation, and may introduce numerical instability in the problem solution.

$$u_i = u_i^0 + zH_{ij}\theta_j \quad (27)$$

$$H_{ij} = \begin{cases} 1, & \text{if } (i,j) = (1,2); (2,1) \\ 0, & \text{otherwise} \end{cases} \quad (28)$$

$$\gamma_{ij}(x,y,z) = \left(1 - \frac{z^2}{h^2}\right)\gamma_{ij}(x,y,z), (i,j) = (1,3), (2,3) \quad (29)$$

Another example can be seen in Reddy's shell theory (Reddy and Ochoa, 2000). The basic deformation theory used is shown in Equation 30, and is reproducible using unified theories. However, when the out-of-plane shear boundary conditions are included, the theory is changed to its mathematical final form in Equation 31 to 33. This form, due to have C1 characteristic and linear variables ( $\theta$ ) appearing in multiple terms, it is not usable with unified formulations, if it is considered in their axiomatic forms.

$$\left\{ \begin{array}{l} u_i = u_i^0 + z\theta_i + z^3\psi_i, i = 1..2 \\ u_3 = u_3^0 + z^2\theta_3 \end{array} \right\} \quad (30)$$

$$u_1 = u_1^0 + z\theta_1 + z^3 \left( \theta_1^* - \frac{\partial w}{\partial y} \right) \quad (31)$$

$$u_2 = u_2^0 + z\theta_2 + z^3 \left( \theta_2^* - \frac{\partial w}{\partial x} \right) \quad (32)$$

$$u_1 = u_1^0 + z\theta_1 + z^2\theta_3^* \quad (33)$$



Two different solutions may solve this problem: either by the use of high order polynomials in the formulation, at least cubic, which guarantee quadratic out-of-plane displacements; or by the use of mixed formulations, in which the out-of-plane stresses are variables to the problem. Furthermore, for LW formulations, the introduction of the boundary conditions only in the top and bottom for the most layers may be applied. This, however, can introduce unrealistic solutions, for which the displacements in the top and bottom layers can be discontinuous, or null, even in cases when they should not be. Section 4.6 will present more details about these facts.

### 4.3 Unified formulations

One of the first researchers to do work with unified formulations for laminate composite materials was Soldatos, who in a series of papers (Soldatos, 1992; Soldatos, 1993; Soldatos and Tomarçi, 1993) introduced a simple expansion based deformation theory to use in pressure vessels and cylindrical geometries. These works considered that the normal Kirchhoff plate theory could be expanded in the plane directions by adding a variable number of degrees of freedom multiplied by pre-defined thickness functions. It should be noted that these functions could take any form, polynomial, axiomatic, trigonometric. Results for these theories were found analytically to test which expansions were more advantageous. However, as the first works on the field, the approach was still limited, not considering kernels or that the constant and linear terms could be also included within the unified formulation.

Years later, using a similar deformation theory than the one used in the works by Soldatos, but identifying patterns that are created from such expanded approach, Carrera and Ciuffreda (2006) first presented unified formulations for composite laminated materials by introducing Carrera's Unified Theory (CUF). These formulations have the premise that, when using axiomatic functions to describe the displacement distribution through the thickness of the plate, the stiffness and mass matrixes as well as the load vectors may be mathematically described by immutable sub-matrices called kernels. These kernels follow a pattern dependent only on the order of the polynomials used for describing the displacements, and as such, may be mathematically described through unique single equations. That way, the

unified formulations can generate any kind of axiomatic deformation theory, using the order of the expansion as an input.

This particular approach derived in several subsequent studies with different improvements for the formulations in the following years, such as investigations about cylinders, single and double-curved shell elements (Cineffra et al., 2014a), delamination (Kumar et al., 2014), modal analysis (Cineffra et al., 2014b), and including different effects such as thermal and damping effect.

Demasi (2009) introduced the Generalized Unified Formulation (GUF). The difference from Carrera's Unified Formulation being that the functions that generate each displacement now is independent and may be any function that follows some mathematical restrictions. Demasi published GUF for axiomatic polynomials and mixed formulations.

Caliri et al. (2016) made further improvements creating Caliri's Generalized Formulation (CGF), which includes the derivatives of displacements as variables, turning the formulation into a true C1 formulation, which provides improvements for the simulation of thick laminated structures or ones with huge elastic property difference between layers, such as sandwich structures.

Due to the reasons discussed in Chapters 3 and herein, for the current work, an adapted GUF formulation was chosen as the basic formulation.

#### 4.4 Classic "classic" formulation

The basic expansion for the displacement and out-of-plane stress fields, using GUF for a LW theory is found in Equation 34. In this equation:  $u$  are the displacements;  $k = 1..N_k$  represents a counter for the layer of the composite, and  $N_k$  is the number of layers in the lay-up;  $i = 1..3$  is the coordinate versor direction counter;  $\alpha_{u_i} = 1..N_{u_i} + 1$  defines the order counter for a given displacement.  $N_{u_i}$  gives maximum the order of the axiomatic polynomial that describes the  $u_i$  distribution through the thickness of the layer. For example, if  $N_{u_1} = 3$ ,  $\alpha_{u_1}$  varies between 1 and 4, and there are four different  $F$  polynomials with the maximum order being cubic.

$$u_i^k = {}^k F_{\alpha_{u_i}} u_{i_{\alpha_{u_i}}}^k, i = 1..3; \alpha_{u_i} = 1..N_{u_i} + 1 \quad (34)$$

Where the  $F$  functions that discretize the displacements through the thickness of each layer need to have the following properties for the compatibility between layers to be possible:

- The functions must guarantee that at the top and bottom edges of each lamina, the displacements correspondent to only that point, i.e.  $u^k(z = z_{top}) = u_{i_1}$  and  $u^k(z = z_{bot}) = u_{i_{N_{u_i}}}$ . As such, the  $F$  functions must be such that:

$$F_{\alpha_{u_i}}(z = z_{top}^k) = \begin{cases} 1, & \text{if } \alpha_{u_i} = 1 \\ 0, & \text{otherwise} \end{cases} \quad (35)$$

$$F_{\alpha_{u_i}}(z = z_{bot}^k) = \begin{cases} 1, & \text{if } \alpha_{u_i} = N_{u_i} + 1 \\ 0, & \text{otherwise} \end{cases} \quad (36)$$

The following group of equations summarizes these conditions:

$$\begin{cases} F_{\alpha_{u_i}}(z = z_{bot}^k) = 0, F_{\alpha_{u_i}}(z = z_{top}^k) = 1; \alpha_{u_i} = 1 \\ F_{\alpha_{u_i}}(z = z_{bot}^k) = 1, F_{\alpha_{u_i}}(z = z_{top}^k) = 0; \alpha_{u_i} = N_{u_i} + 1 \\ F_{\alpha_{u_i}}(z = z_{bot}^k) = 0, F_{\alpha_{u_i}}(z = z_{top}^k) = 0; 1 < \alpha_{u_i} < N_{u_i} + 1 \end{cases} \quad (37)$$

- As per Demasi et al (2006) polynomial functions of the type  $z^n$  create ill conditioned through the thickness distributions for the shear stresses and strains, as well as

discontinuities on the derivatives of the distributions, it is recommended to use orthogonal polynomials.

As such, even if any function may be chosen, Demasi et al (2006) recommends the use of sums of Legendre polynomials defined by the following Equations 38 to 40. In these equations  $\xi^k \in [-1, +1]$  is the local coordinate system for the  $k$ -th layer,  $z_{top}^k$  and  $z_{bot}^k$  are the thickness coordinates of the top and bottom of the  $k$ -th layer and  $P_n$  is the Legendre polynomial of order  $n$ , given by Bonnet's recursion (Kreyszig, 1999) found in Equations 41 to 43:

$$\xi_k(z) = \frac{2}{z_{top}^k - z_{bot}^k} z + \frac{z_{top}^k + z_{bot}^k}{z_{top}^k - z_{bot}^k} \quad (38)$$

$$F_{\alpha_{u_i}}(\xi) = P_{\alpha_{u_i}}(\xi) - P_{\alpha_{u_i}-2}(\xi) \quad (39)$$

$$\begin{cases} F_{\alpha_{u_i}} = \frac{P_0 + P_1}{2}; \alpha = 1 \\ F_{\alpha_{u_i}} = P_\alpha - P_{\alpha-2}; \alpha = N_{u_i} \\ F_{\alpha_{u_i}} = \frac{(P_0 - P_1)}{2}; 1 < \alpha < N_{u_i} \end{cases} \quad (40)$$

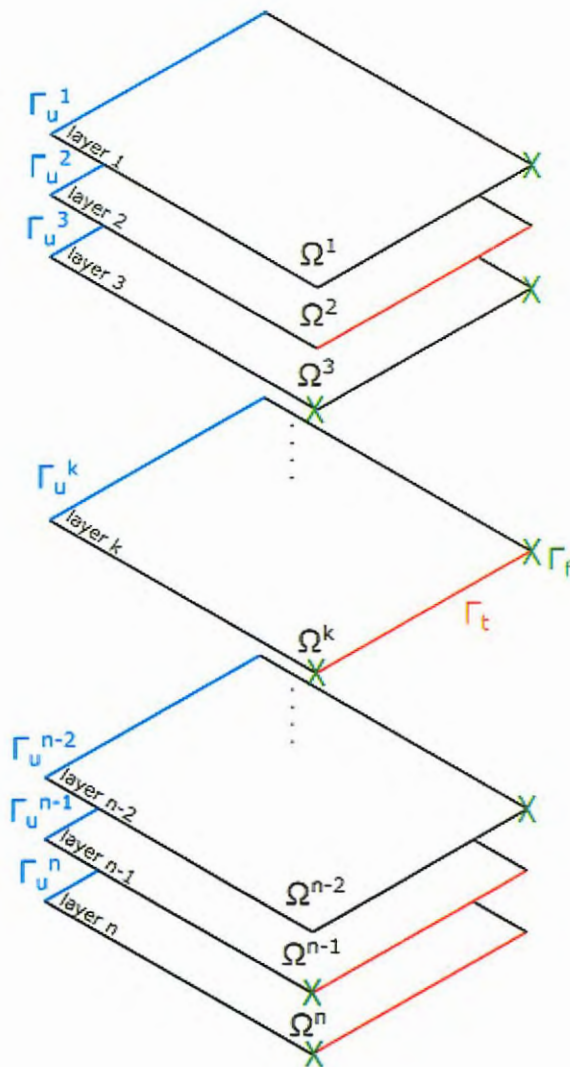
$$P_0(\xi_k) = 1 \quad (41)$$

$$P_1(\xi_k) = \xi_k \quad (42)$$

$$P_{n+1}(\xi_k) = \frac{(2n+1)\xi_k P_n(\xi_k) - n P_{n-1}(\xi_k)}{n+1} \quad (43)$$

Given a  $\Omega$  domain of a shell finite element with mechanical virtual work  $\delta L$  being done in  $\Gamma_t$  and with prescribed boundary conditions in  $\Gamma_u$ , schematized in Figure 22, the Principle of Stationarity establish equilibrium as a system of equations that contains the equilibrium between the internal virtual deformation energy and external virtual work done in each layer  $k$  (Zienkiewicz and Taylor, 2000).

Figure 22 – Shell finite element domain representation



Source: Developed by the author

$$\int_{\Omega} \delta \varepsilon^{k^t} \sigma^k d\Omega = \delta L^k \tag{44}$$

The virtual work of the external loads  $\delta L^k$  can be described in terms of body forces over the whole  $\Omega - \Gamma_u$  domain, surface loads over the  $\Gamma_t$  domain and concentrated loads located over specific  $\bar{x}$  points.

$$\delta L = \int_{\Omega} \delta u \cdot b \, d\Omega + \oint_{\Gamma_t} \delta u \cdot t \, d\Gamma_t + [\delta u \cdot F] \Big|_{x=\bar{x}} \quad (45)$$

Simplifying the virtual work of external loads  $\delta L^k$  to just done by distributed pressure components  $P_i$  working on the top and bottom of each layer over  $\Omega$ , and internal tractions  $t_i$  working over the thickness of each layer over  $\Gamma_t$ , it is possible to written Equation 46.

$$\begin{aligned} \int_{\Omega} \int_{z_{bot}^k}^{z_{top}^k} \delta \varepsilon^{k,t} \sigma^k \, dz \, d\Omega &= \int_{\Omega} \delta u_i^k \Big|_{z=z_{top}} P_i^k \Big|_{z=z_{top}} \, d\Omega + \int_{\Omega} \delta u_i^k \Big|_{z=z_{bot}} P_i^k \Big|_{z=z_{bot}} \, d\Omega + \\ &\int_{\Gamma_t} \int_{z_{bot}^k}^{z_{top}^k} \delta u_i^k t_i \, dz \, d\Gamma_t \end{aligned} \quad (46)$$

Which may be expanded using the constitutive Equations previous presented in Equation 7 to:

$$\begin{aligned} \delta \varepsilon^t \sigma &= +\delta \varepsilon_{xx} \bar{C}_{11} \varepsilon_{xx} + \delta \varepsilon_{xx} \bar{C}_{12} \varepsilon_{yy} + \delta \varepsilon_{xx} \bar{C}_{16} \gamma_{xy} + \delta \varepsilon_{xx} \bar{C}_{13} \sigma_{zz} + \delta \varepsilon_{yy} \bar{C}_{12} \varepsilon_{xx} + \\ &\delta \varepsilon_{yy} \bar{C}_{22} \varepsilon_{yy} + \delta \varepsilon_{yy} \bar{C}_{26} \gamma_{xy} + \delta \varepsilon_{yy} \bar{C}_{23} \sigma_{zz} + \delta \gamma_{xy} \bar{C}_{16} \varepsilon_{xx} + \delta \gamma_{xy} \bar{C}_{26} \varepsilon_{yy} + \delta \gamma_{xy} \bar{C}_6 \gamma_{xy} + \\ &\delta \gamma_{xy} \bar{C}_{36} \sigma_{zz} + \delta \sigma_{xz} \bar{C}_{55} \sigma_{xz} + \delta \sigma_{xz} \bar{C}_{45} \sigma_{yz} + \delta \sigma_{yz} \bar{C}_{45} \sigma_{xz} + \delta \sigma_{yz} \bar{C}_{44} \sigma_{yz} + \\ &\delta \sigma_{zz} \bar{C}_{13} \varepsilon_{xx} + \delta \sigma_{zz} \bar{C}_{23} \varepsilon_{yy} + \delta \sigma_{zz} \bar{C}_{36} \gamma_{xy} + \delta \sigma_{zz} \bar{C}_{36} \gamma_{xy} + \delta \sigma_{zz} \bar{C}_{33} \sigma_{zz} \end{aligned} \quad (47)$$

Using the strain definition found in Equation 48 and applying it to Equation 47, then it is possible to obtain 9 immutable kernels for stiffness matrices for each layer, and three identical kernels for the load vector. As such, a final equilibrium equation is found in Equation 49 and 50.

$$\varepsilon = \{\varepsilon_{xx} \quad \varepsilon_{yy} \quad \gamma_{zz}\}^T = \left\{ \frac{\partial u_1}{\partial x_1} \quad \frac{\partial u_2}{\partial x_2} \quad \frac{\partial u_1}{\partial x_2} + \frac{\partial u_2}{\partial x_1} \right\}^T \quad (48)$$

$$\begin{aligned} \delta \varepsilon_m^T \sigma_m = & +\delta \varepsilon_{xx} \bar{C}_{11} \varepsilon_{xx} + \delta \varepsilon_{xx} \bar{C}_{12} \varepsilon_{yy} + \delta \varepsilon_{xx} \bar{C}_{16} \gamma_{xy} + \delta \varepsilon_{xx} \bar{C}_{13} \sigma_{zz} + \delta \varepsilon_{yy} \bar{C}_{12} \varepsilon_{xx} + \\ & \delta \varepsilon_{yy} \bar{C}_{22} \varepsilon_{yy} + \delta \varepsilon_{yy} \bar{C}_{26} \gamma_{xy} + \delta \varepsilon_{yy} \bar{C}_{23} \sigma_{zz} + \delta \gamma_{xy} \bar{C}_{16} \varepsilon_{xx} + \delta \gamma_{xy} \bar{C}_{26} \varepsilon_{yy} + \delta \gamma_{xy} \bar{C}_{6} \gamma_{xy} + \\ & \delta \gamma_{xy} \bar{C}_{36} \sigma_{zz} \end{aligned} \tag{49}$$

$$\delta u_i = 0 \in \Gamma_u \tag{50}$$

For simplicity sake, the terms indicating the integration of the product of two different  $F$  functions, its derivatives in relation to the thickness direction, and/or a corresponding elastic property  $C_{ij}$  are grouped together in a single variable  ${}^k Z_{ij}^{\alpha_{u_i}, \beta_{u_j}, m}$  shown in Table 3. The same was made for the load vector and with the  $D$  variables, explained in Equation 51 and 52.

Table 3 – Z meaning for classic formulation

Symbol	Meaning
${}^k Z_{ij}^{\alpha_{u_m}, \beta_{u_n}}$	$\bar{C}_{ij} \int_{z_{bot}^k}^{z_{top}^k} F_{\alpha_{u_m}} F_{\beta_{u_n}} dz$
${}^k Z^{\alpha_{u_m}, \beta_{u_n}}$	$\int_{z_{bot}^k}^{z_{top}^k} F_{\alpha_{u_m}} F_{\beta_{u_n}} dz$
${}^k Z_{ij}^{\alpha_{u_m}, 3\beta_{u_n}, 3}$	$\bar{C}_{ij} \int_{z_{bot}^k}^{z_{top}^k} F_{\alpha_{u_m}, 3} F_{\beta_{u_n}, 3} dz$
${}^k Z_{ij}^{\alpha_{u_m}, 3\beta_{u_n}}$	$\bar{C}_{ij} \int_{z_{bot}^k}^{z_{top}^k} F_{\alpha_{u_m}, 3} F_{\beta_{u_n}} dz$
${}^k Z_{ij}^{\alpha_{u_m}, \beta_{u_n}, 3}$	$\bar{C}_{ij} \int_{z_{bot}^k}^{z_{top}^k} F_{\alpha_{u_m}} F_{\beta_{u_n}, 3} dz$
${}^k Z^{\alpha_{u_m}, 3\beta_{u_n}, 3}$	$\int_{z_{bot}^k}^{z_{top}^k} F_{\alpha_{u_m}, 3} F_{\beta_{u_n}, 3} dz$
${}^k Z^{\alpha_{u_m}, 3\beta_{u_n}}$	$\int_{z_{bot}^k}^{z_{top}^k} F_{\alpha_{u_m}, 3} F_{\beta_{u_n}} dz$
${}^k Z^{\alpha_{u_m}, \beta_{u_n}, 3}$	$\int_{z_{bot}^k}^{z_{top}^k} F_{\alpha_{u_m}} F_{\beta_{u_n}, 3} dz$

Source: Developed by the author

$${}^k D_{top}^{\alpha_{um}\beta_{un}} = F_{N_{um}} \Big|_{z=z_{top}} F_{N_{un}} \Big|_{z=z_{top}} \quad (51)$$

$${}^k D_{bot}^{\alpha_{um}\beta_{un}} = F_{N_{um}} \Big|_{z=z_{bot}} F_{N_{un}} \Big|_{z=z_{bot}} \quad (52)$$

Using these simplifications, Equations 53 to 62 shows the nine stiffness matrix kernels and the load vector kernels.

$$\begin{aligned} K_{11}^k &= {}^k Z_{11}^{\alpha_{u_1}\beta_{u_1}} \int_{\Omega} \delta u_{1\alpha_{u_1},1} u_{1\beta_{u_1},1} d\Omega + {}^k Z_{16}^{\alpha_{u_1}\beta_{u_1}} \int_{\Omega} \delta u_{1\alpha_{u_1},1} u_{1\beta_{u_1},2} d\Omega + \\ & {}^k Z_{16}^{\alpha_{u_1}\beta_{u_1}} \int_{\Omega} \delta u_{1\alpha_{u_1},2} u_{1\beta_{u_1},1} d\Omega + {}^k Z_{66}^{\alpha_{u_1}\beta_{u_1}} \int_{\Omega} \delta u_{1\alpha_{u_1},2} u_{1\beta_{u_1},2} d\Omega + \\ & {}^k Z_{55}^{\alpha_{u_1,3}\beta_{u_1,3}} \int_{\Omega} \delta u_{1\alpha_{u_1}} u_{1\beta_{u_1}} d\Omega \end{aligned} \quad (53)$$

$$\begin{aligned} K_{12}^k &= {}^k Z_{12}^{\alpha_{u_1}\beta_{u_2}} \int_{\Omega} \delta u_{1\alpha_{u_1},1} u_{2\beta_{u_2},2} d\Omega + {}^k Z_{16}^{\alpha_{u_1}\beta_{u_2}} \int_A \delta u_{1\alpha_{u_1},1} u_{2\beta_{u_2},1} d\Omega + \\ & {}^k Z_{26}^{\alpha_{u_1}\beta_{u_2}} \int_{\Omega} \delta u_{1\alpha_{u_1},2} u_{2\beta_{u_2},2} d\Omega + {}^k Z_{66}^{\alpha_{u_1}\beta_{u_2}} \int_A \delta u_{1\alpha_{u_1},2} u_{2\beta_{u_2},1} d\Omega + \\ & {}^k Z_{45}^{\alpha_{u_1,3}\beta_{u_2,3}} \int_{\Omega} \delta u_{1\alpha_{u_1}} u_{2\beta_{u_2}} d\Omega \end{aligned} \quad (54)$$

$$\begin{aligned} K_{13}^k &= {}^k Z_{13}^{\alpha_{u_1}\beta_{u_3,3}} \int_{\Omega} \delta u_{1\alpha_{u_1},1} u_{3\beta_{u_3}} d\Omega + {}^k Z_{36}^{\alpha_{u_1}\beta_{u_3,3}} \int_{\Omega} \delta u_{1\alpha_{u_1},2} u_{3\beta_{u_3}} d\Omega + \\ & {}^k Z_{55}^{\alpha_{u_1,3}\beta_{u_3}} \int_{\Omega} \delta u_{1\alpha_{u_1}} u_{3\beta_{u_3},1} d\Omega + {}^k Z_{45}^{\alpha_{u_1,3}\beta_{u_3}} \int_{\Omega} \delta u_{1\alpha_{u_1}} u_{3\beta_{u_3},2} d\Omega \end{aligned} \quad (55)$$

$$\begin{aligned} K_{21}^k &= {}^k Z_{12}^{\alpha_{u_2}\beta_{u_1}} \int_{\Omega} \delta u_{2\alpha_{u_2},2} u_{1\beta_{u_1},1} d\Omega + {}^k Z_{26}^{\alpha_{u_2}\beta_{u_1}} \int_{\Omega} \delta u_{2\alpha_{u_2},2} u_{1\beta_{u_1},2} d\Omega + \\ & {}^k Z_{16}^{\alpha_{u_2}\beta_{u_1}} \int_{\Omega} \delta u_{2\alpha_{u_2},1} u_{1\beta_{u_1},1} d\Omega + {}^k Z_{66}^{\alpha_{u_2}\beta_{u_1}} \int_{\Omega} \delta u_{2\alpha_{u_2},1} u_{1\beta_{u_1},2} d\Omega + \\ & {}^k Z_{45}^{\alpha_{u_2,3}\beta_{u_1,3}} \int_{\Omega} \delta u_{2\alpha_{u_2}} u_{1\beta_{u_1}} d\Omega \end{aligned} \quad (56)$$



$$\begin{aligned}
 K_{22}^k &= {}^k Z_{22}^{\alpha_{u_2} \beta_{u_2}} \int_{\Omega} \delta u_{2\alpha_{u_2},2} u_{2\beta_{u_2},2} d\Omega + {}^k Z_{26}^{\alpha_{u_2} \beta_{u_2}} \int_{\Omega} \delta u_{2\alpha_{u_2},2} u_{2\beta_{u_2},1} d\Omega + \\
 & {}^k Z_{26}^{\alpha_{u_2} \beta_{u_2}} \int_{\Omega} \delta u_{2\alpha_{u_2},1} u_{2\beta_{u_2},2} d\Omega + {}^k Z_{66}^{\alpha_{u_2} \beta_{u_2}} \int_{\Omega} \delta u_{2\alpha_{u_2},1} u_{2\beta_{u_2},1} d\Omega + \\
 & {}^k Z_{55}^{\alpha_{u_2},3\beta_{u_2},3} \int_{\Omega} \delta u_{2\alpha_{u_2}} u_{2\beta_{u_2}} d\Omega
 \end{aligned} \tag{57}$$

$$\begin{aligned}
 K_{23}^k &= {}^k Z_{23}^{\alpha_{u_2} \beta_{u_3},3} \int_{\Omega} \delta u_{2\alpha_{u_2},2} u_{3\beta_{u_3}} d\Omega + {}^k Z_{36}^{\alpha_{u_2} \beta_{u_3},3} \int_{\Omega} \delta u_{2\alpha_{u_2},1} u_{3\beta_{u_3}} d\Omega + \\
 & {}^k Z_{45}^{\alpha_{u_2},3\beta_{u_3}} \int_{\Omega} \delta u_{2\alpha_{u_2}} u_{3\beta_{u_3},1} d\Omega + {}^k Z_{44}^{\alpha_{u_2},3\beta_{u_3}} \int_{\Omega} \delta u_{2\alpha_{u_2}} u_{3\beta_{u_3},2} d\Omega
 \end{aligned} \tag{58}$$

$$\begin{aligned}
 K_{31}^k &= {}^k Z_{55}^{\alpha_{u_3} \beta_{u_1},3} \int_{\Omega} \delta u_{3\alpha_{u_3},3} u_{1\beta_{u_1}} d\Omega + {}^k Z_{45}^{\alpha_{u_3} \beta_{u_1},3} \int_{\Omega} \delta u_{3\alpha_{u_3},2} u_{1\beta_{u_1}} d\Omega + \\
 & {}^k Z_{13}^{\alpha_{u_3},3\beta_{u_1}} \int_{\Omega} \delta u_{3\alpha_{u_3}} u_{1\beta_{u_1},1} d\Omega + {}^k Z_{36}^{\alpha_{u_3},3\beta_{u_1}} \int_{\Omega} \delta u_{3\alpha_{u_3}} u_{1\beta_{u_1},2} d\Omega
 \end{aligned} \tag{59}$$

$$\begin{aligned}
 K_{23}^k &= {}^k Z_{55}^{\alpha_{u_3} \beta_{u_2},3} \int_{\Omega} \delta u_{3\alpha_{u_3},1} u_{2\beta_{u_2}} d\Omega + {}^k Z_{44}^{\alpha_{u_3} \beta_{u_2},3} \int_{\Omega} \delta u_{3\alpha_{u_3},2} u_{2\beta_{u_2}} d\Omega + \\
 & {}^k Z_{23}^{\alpha_{u_3},3\beta_{u_2}} \int_{\Omega} \delta u_{3\alpha_{u_3}} u_{2\beta_{u_2},2} d\Omega + {}^k Z_{36}^{\alpha_{u_3},3\beta_{u_2}} \int_{\Omega} \delta u_{3\alpha_{u_3}} u_{2\beta_{u_2},1} d\Omega
 \end{aligned} \tag{60}$$

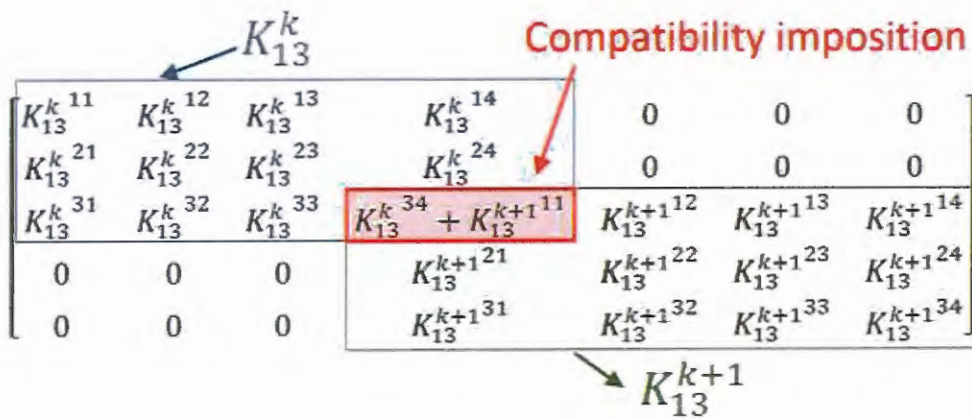
$$\begin{aligned}
 K_{33}^k &= {}^k Z_{55}^{\alpha_{u_3} \beta_{u_3}} \int_{\Omega} \delta u_{3\alpha_{u_3},1} u_{3\beta_{u_3},1} d\Omega + {}^k Z_{45}^{\alpha_{u_3} \beta_{u_3}} \int_{\Omega} \delta u_{3\alpha_{u_3},1} u_{3\beta_{u_3},2} d\Omega + \\
 & {}^k Z_{45}^{\alpha_{u_3} \beta_{u_3}} \int_{\Omega} \delta u_{3\alpha_{u_3},2} u_{3\beta_{u_3},1} d\Omega + {}^k Z_{44}^{\alpha_{u_3} \beta_{u_3}} \int_{\Omega} \delta u_{3\alpha_{u_3},1} u_{3\beta_{u_3},1} d\Omega + \\
 & {}^k Z_{55}^{\alpha_{u_2},3\beta_{u_2},3} \int_{\Omega} \delta u_{2\alpha_{u_2}} u_{2\beta_{u_2}} d\Omega
 \end{aligned} \tag{61}$$

$$\begin{aligned}
 R_{\alpha_{u_i}}^k &= \oint_{\Omega} {}^i F_{1u_i} {}^i F_{1u_i} {}^i p_{\beta_{u_i}}^t dx dy + \oint_{\Omega} {}^i F_{Nu_i} {}^i F_{Nu_i} {}^i p_{\beta_{u_i}}^b dx dy + \\
 & \frac{h_k}{2} \oint_{\Omega} \int_{-1}^{+1} {}^i F_{\alpha_{s_i}} {}^i F_{\beta_{s_i}} \overline{s_n^k} dz dx dy
 \end{aligned} \tag{62}$$

By taking sums of normalized Legendre polynomials as the functions for the deformations over the thickness of each layer, and functions with the properties previous mentioned, the compatibility of displacements and stresses between layers is automatically imposed, and as such, can be applied by a simple summation of the matrix kernels and vectors of each layer.

This compatibility is accomplished by making sure the terms in each matrix and vector kernels for each layer is summed to term corresponding to the same degree of freedom, which corresponds to the matrices and vector kernels for the next layer. For example, in a laminate with three layers (stacked from top to bottom), the bottom degrees of freedom of the first layer correspond to the top degrees of freedom of the second layer, and the bottom degrees of freedom of the second layer correspond to the top degrees of freedom of the third layer. This can be mathematically described as:  $u_{iN_{u_i}}^1 = u_{i1}^2$  and  $u_{iN_{u_i}}^2 = u_{i1}^3$ . As such, laminate kernels  $K_{ij}$  and  $R_{j\alpha_{u_i}}$  may be assembled using the layer kernels as shown in the Figure 23 for the  $K_{13}$  kernel in the case of  $N_{u_1} = 2$  and  $N_{u_3} = 3$ . Notice that each individual  $K_{13}^k$  layer matrix has 3 lines ( $N_{u_1} = 2$  so there are 3 variables that compose  $u_1^k$ ), 4 columns ( $N_{u_3} = 3$  so there are 4 variables that compose  $u_3^k$ ). Also, in this case the terms 34 from the k-th layer and 11 from the k+1-th layer are summed, as compatibility is imposed by guaranteeing that the displacements at the top of the k-th layer (34) is equal to the bottom displacements at the k+1-th layer (11), and as such receive stiffness contributions from both layers.

Figure 23 – Compatibility imposition between layers. Example for the  $K_{13}$  matrix,  $N_{u_1} = 2$  and  $N_{u_3} = 3$



Source: Developed by the author

Which forms the system of equations shown in Equation 63. Where each element  $K_{ij}$ ,  $U_i$  and  $R_i$  represents a one of the nine stiffness kernels  $K$ , displacements  $U$  or loads  $R$ ,

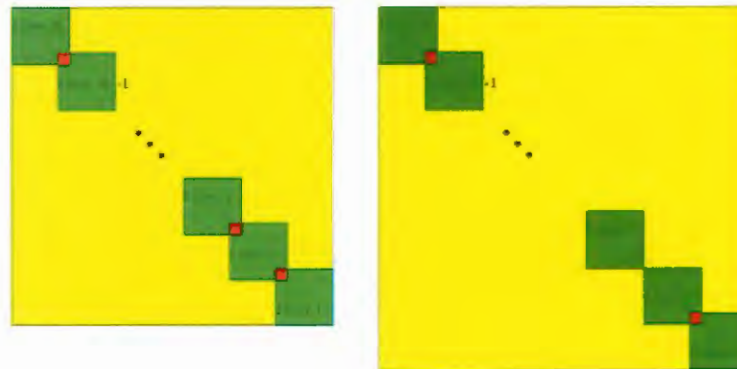
which compromise all the different degrees of freedom corresponding to the different orders of  $N_{u_i}$ , as shown in Equation 64.

$$\begin{bmatrix} K_{11} & K_{12} & K_{13} \\ K_{21} & K_{22} & K_{23} \\ K_{31} & K_{23} & K_{33} \end{bmatrix} \begin{Bmatrix} U_1 \\ U_2 \\ U_3 \end{Bmatrix} = \begin{Bmatrix} R_1 \\ R_2 \\ R_3 \end{Bmatrix} \tag{63}$$

$$U_i = \{ u_{i_1}^1 \quad \dots \quad u_{i_{\alpha_{u_i}}}^1 \quad \dots \quad u_{i_{N_{u_i}}}^1 \quad u_{i_1}^2 \quad \dots \quad u_{i_{\alpha_{u_i}}}^2 \quad \dots \quad u_{i_{N_{u_i}}}^2 \quad u_{i_1}^3 \quad \dots \quad u_{i_{\alpha_{u_i}}}^k \quad \dots \quad u_{i_{N_{u_i}}}^{N_k} \}^t \tag{64}$$

An important note about the assemble of laminate kernels from layer kernels when using the sum of Legendre polynomials is that, as some researchers showed (Kumar et al. 2014), using these type of formulations, delaminations may be easily simulated by, in the delaminated area, inserting additional degrees of freedom between the delaminated layers, and completely separating the matrices kernels. Figure 24 shows this procedure. This approach will address in future works (See Chapter 7. Final Discussions, Conclusions and Future Works), for which the delamination models may interact with the macroscale analysis.

Figure 24 – Compatibility imposition between layers in the presence of delamination, example between Layers 2 and 3



Source: Kumar et al. (2014)

#### 4.5 Mixed formulation

The formulation for the mixed shell elements is similar to the previous formulation for the classic element, and as such, when applicable, some steps will be skipped for brevity. The basic expansion for the displacement and out-of-plane stress fields, using Demasi's GUF for LW, is found in Equations 65 and 66. In the following equations  $s_i$  corresponds to  $\sigma_{i3}$  for  $i = 1..3$  for simplicity of notation.

$$u_i^k = {}^kF_{\alpha_{u_i}} u_{i\alpha_{u_i}}^k, i = 1..3; \alpha_{u_i} = 1..N_{u_i} + 1 \quad (65)$$

$$s_i = {}^kG_{\alpha_{s_i}} s_{i\alpha_{s_i}}^k; i = 1..3; \alpha_{s_i} = 1..N_{s_i} + 1 \quad (66)$$

where, in a similar manner to the classic formulation previously discussed,  $i$  are local directional indexes;  $k = 1..N_k$  represents a counter for the layer of the composite, and  $N_k$  is the number of layers in the lay-up. As for variables:  $u_i^k$  are the displacements at the bottom and top of each layer;  $s_i^k$  are the out-of-plane stresses at the top and bottom of each layer;  $N_{u_i}$  and  $N_{\sigma_{ij}}$  are the order of the desired discretization of each variable, following the same logic as the one for the classical theory.

In particular, the functions  $F$  and  $G$  are picked in such a way that compatibility is imposed between layers, following the same logic and requirements as the classic formulation, but now also applied to the out-of-plane stresses, which incur additional boundary conditions:

$$F_{\alpha_{u_i}}(z = z_{top}^k) = \begin{cases} 1, & \text{if } \alpha_{u_i} = 1 \\ 0, & \text{otherwise} \end{cases} \quad (67)$$

$$F_{\alpha_{u_i}}(z = z_{bot}^k) = \begin{cases} 1, & \text{if } \alpha_{u_i} = N_{u_i} + 1 \\ 0, & \text{otherwise} \end{cases} \quad (68)$$

$$G_{\alpha_{s_i}}(z = z_{top}^k) = \begin{cases} 1, & \text{if } \alpha_{s_i} = 1 \\ 0, & \text{if } \alpha_{s_i} \neq 1 \text{ or } k = 1 \end{cases} \quad (69)$$

$$G_{\alpha_{s_i}}(z = z_{bot}^k) = \begin{cases} 1, & \text{if } \alpha_{s_i} = N_{s_i} + 1 \\ 0, & \text{if } \alpha_{s_i} \neq N_{s_i} + 1 \text{ or } k = N_k \end{cases} \quad (70)$$

The following group of equations summarizes these conditions. Again, by taking  $F$  and  $G$  as sums of Legendre polynomials defined the same way as for the classic formulation in Equations 71 to 74, these boundary conditions are satisfied (Demasi et al, 2006).

$$\begin{cases} F_{\alpha_{u_i}}(z = z_{bot}^k) = 0, F_{\alpha_{u_i}}(z = z_{top}^k) = 1; \alpha_{u_i} = 1 \\ F_{\alpha_{u_i}}(z = z_{bot}^k) = 1, F_{\alpha_{u_i}}(z = z_{top}^k) = 0; \alpha_{u_i} = N_{u_i} + 1 \\ F_{\alpha_{u_i}}(z = z_{bot}^k) = 0, F_{\alpha_{u_i}}(z = z_{top}^k) = 0; 1 < \alpha_{u_i} < N_{u_i} + 1 \end{cases} \quad (71)$$

$$\begin{cases} G_{\alpha_{s_i}}(z = z_{bot}^k) = 0, G_{\alpha_{s_i}}(z = z_{top}^k) = 1; \alpha_{s_i} = 1 \\ G_{\alpha_{s_i}}(z = z_{bot}^k) = 1, G_{\alpha_{s_i}}(z = z_{top}^k) = 0; \alpha_{s_i} = N_{s_i} + 1 \\ G_{\alpha_{s_i}}(z = z_{bot}^k) = 0, G_{\alpha_{s_i}}(z = z_{top}^k) = 0; 1 < \alpha_{s_i} < N_{s_i} + 1 \end{cases} \quad (72)$$

$$G_{\alpha_{s_i}}^k(z = z_{top}^k) = 0, \text{ if } k = 1 \quad (73)$$

$$G_{\alpha_{s_i}}^k(z = z_{bot}^k) = 0, \text{ if } k = N_k \quad (74)$$

As for the equilibrium equation, instead of the classic one, an adapted equilibrium expression is needed to ensure the continuity of stresses through the thickness and to guarantee the strains compatibility through the deformable body (Fung, 1994). For that to happen, additional terms appear due to the mixed terms.

One such way to write the equilibrium equation considering these problems consists on using Reissner's Mixed Variational Theorem (RMVT) (Reissner, 1984; Reissner, 1986). This formulation defines that the variational of the deformation energy that comes from the out-of-plane must be taken into account from both its geometric effect ( $\varepsilon_{SG}$ ) and from the work generated from the out-of-plane stresses ( $\sigma_{sS}$ ). As such, the strains are calculated as Equation

75 to 77, and the equilibrium equation is found in Equation 78, in weak form, where  $\delta L$  is the variational of the work of the external loads, which is the same as the one for the classic formulation, found in Equations 46. A final note is that the out-of-planes stresses, even as degrees of freedom, do not generate compatible external loads.

$$\varepsilon_m = \{\varepsilon_{xx} \quad \varepsilon_{yy} \quad \gamma_{zz}\}^T = \left\{ \frac{\partial u_1}{\partial x_1} \quad \frac{\partial u_2}{\partial x_2} \quad \frac{\partial u_1}{\partial x_2} + \frac{\partial u_2}{\partial x_1} \right\}^T \quad (75)$$

$$\varepsilon_{SG} = \{\gamma_{xz} \quad \gamma_{yz} \quad \varepsilon_{zz}\}_G^t = \left\{ \frac{\partial u_1}{\partial x_3} + \frac{\partial u_3}{\partial x_1} \quad \frac{\partial u_2}{\partial x_3} + \frac{\partial u_3}{\partial x_2} \quad \frac{\partial u_3}{\partial x_3} \right\}^t \quad (76)$$

$$\varepsilon_{SS} = \{\gamma_{xz} \quad \gamma_{yz} \quad \varepsilon_{zz}\}_S^t = \{Q_{55}\sigma_{xz} + Q_{45}\sigma_{yz} \quad Q_{45}\sigma_{xz} + Q_{44}\sigma_{yz} \quad -Q_{13}\varepsilon_{xx} - Q_{23}\varepsilon_{yy} - Q_{36}\gamma_{xy} + Q_{33}\sigma_{zz}\}^t \quad (77)$$

$$\int_{\Omega} \delta \varepsilon_m^k \sigma_m^k + \delta \varepsilon_{SG}^k \sigma_{SG}^k + \delta \sigma_{SS}^k (\varepsilon_{SS}^k - \varepsilon_{SS}^k) d\Omega = \delta L^k \quad (78)$$

Using this notation, the terms of the equilibrium equation are shown in explicit form in Equation 79 to 82.

$$\begin{aligned} \delta \varepsilon_m^T \sigma_m &= +\delta \varepsilon_{xx} Q_{11} \varepsilon_{xx} + \delta \varepsilon_{xx} Q_{12} \varepsilon_{yy} + \delta \varepsilon_{xx} Q_{16} \gamma_{xy} + \delta \varepsilon_{xx} Q_{13} \sigma_{zz} + \delta \varepsilon_{yy} Q_{12} \varepsilon_{xx} + \\ &\quad \delta \varepsilon_{yy} Q_{22} \varepsilon_{yy} + \delta \varepsilon_{yy} Q_{26} \gamma_{xy} + \delta \varepsilon_{yy} Q_{23} \sigma_{zz} + \delta \gamma_{xy} Q_{16} \varepsilon_{xx} + \delta \gamma_{xy} Q_{26} \varepsilon_{yy} + \\ &\quad \delta \gamma_{xy} Q_{66} \gamma_{xy} + \delta \gamma_{xy} Q_{36} \sigma_{zz} \end{aligned} \quad (79)$$

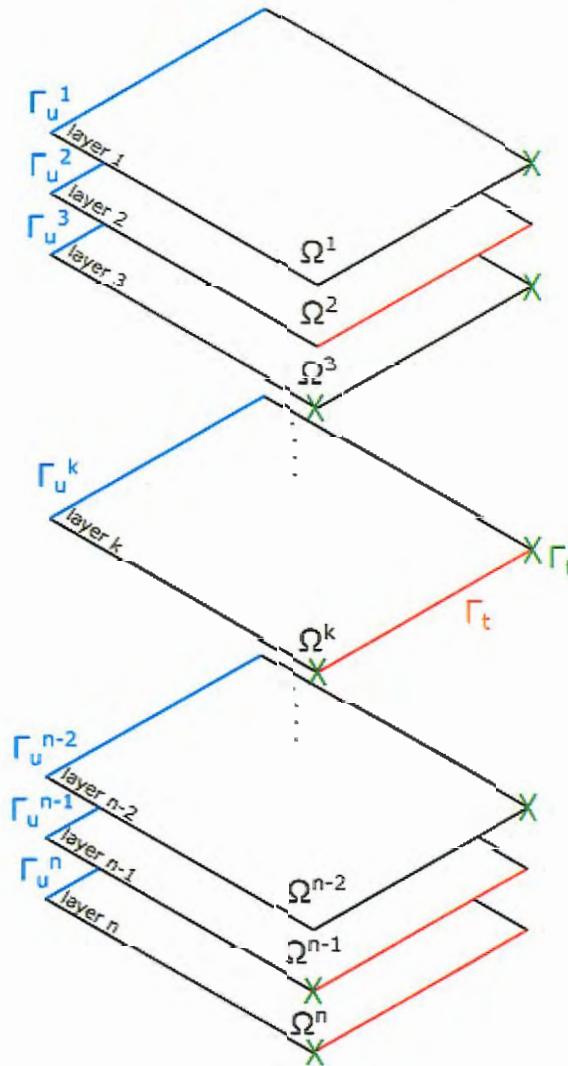
$$\delta \varepsilon_{SG} \sigma_S = \delta \gamma_{xz} \sigma_{xz} + \delta \gamma_{yz} \sigma_{yz} + \delta \varepsilon_{zz} \sigma_{zz} \quad (80)$$

$$\delta \sigma_S \varepsilon_{SG} = \delta \sigma_{xz} \gamma_{xz} + \delta \sigma_{yz} \gamma_{yz} + \delta \sigma_{zz} \varepsilon_{zz} \quad (81)$$

$$\begin{aligned} -\delta \sigma_S \varepsilon_{SS} &= -\delta \sigma_{xz} Q_{55} \sigma_{xz} - \delta \sigma_{xz} Q_{45} \sigma_{yz} - \delta \sigma_{yz} Q_{45} \sigma_{xz} - \delta \sigma_{yz} Q_{44} \sigma_{yz} + \delta \sigma_{zz} Q_{13} \varepsilon_{xx} + \\ &\quad \delta \sigma_{zz} Q_{23} \varepsilon_{yy} + \delta \sigma_{zz} Q_{36} \gamma_{xy} + \delta \sigma_{zz} Q_{36} \gamma_{xy} - \delta \sigma_{zz} Q_{33} \sigma_{zz} \end{aligned} \quad (82)$$

Similarly to the classic formulation, given the domains of a shell element  $\Omega$  and boundaries  $\Gamma$  defined in Figure 25, the external load work can be separated into body loads (b), boundary loads (t) and concentrated forces (F) as shown by Equation 83 (Bathe, 1996).

Figure 25 - Shell finite element domain representation



Source: Developed by the author

$$\delta L = \int_{\Omega} \delta u \cdot b \, d\Omega + \oint_{\Gamma_t} \delta u \cdot t \, d\Gamma_t + [\delta u \cdot F]_{x=\bar{x}} \quad (83)$$

Where  $i$  are local directional indexes; and  $k$  is an index counting every layer in the laminate. Simplifying the virtual work of external loads  $\delta L^k$  to just done by distributed pressure components  $P_i$  working on the top and bottom of each layer over  $\Omega$ , and internal tractions  $t_i$  working over the thickness of each layer over  $\Gamma_t$ , it is possible to obtain Equation 84 and 85.

$$\int_{\Omega} \int_{z_{bot}^k}^{z_{top}^k} \delta \varepsilon_m^k \sigma_m^k + \delta \varepsilon_{SG}^k \sigma_{SG}^k + \delta \sigma_{SS}^k (\varepsilon_{SS}^k - \varepsilon_{SS}^k) dz d\Omega = \int_{\Omega} \delta u_i^k \Big|_{z=z_{top}} P_i^k \Big|_{z=z_{top}} d\Omega + \int_{\Omega} \delta u_i^k \Big|_{z=z_{bot}} P_i^k \Big|_{z=z_{bot}} d\Omega + \int_{\Gamma_t} \int_{z_{bot}^k}^{z_{top}^k} \delta u_i^k t_i dz d\Gamma_t \quad (84)$$

$$\delta u_i = 0 \in \Gamma_u \quad (85)$$

For simplicity sake, the same way as for the classic formulation, the terms of the integration for the product of two different  $F$  functions multiplied by the elastic property  $\bar{Q}_{ij}$  are grouped together in a single variable  ${}^k Z_{ij}^{\alpha_{u_i} \beta_{u_j}}$ , where the meaning is shown by Table 4. The same was made for the load vector and for the  $D$  variables as shown by Equations 86 and 87. The difference to the classic formulation is that, as the mixed-formulation does not require through the thickness derivatives, the definitions are simpler.

$${}^k D_{top}^{\alpha_{u_m} \beta_{u_n}} = F_{N_{u_m}} \Big|_{z=z_{top}} F_{N_{u_n}} \Big|_{z=z_{top}} \quad (86)$$

$${}^k D_{bot}^{\alpha_{u_m} \beta_{u_n}} = F_{N_{u_m}} \Big|_{z=z_{bot}} F_{N_{u_n}} \Big|_{z=z_{bot}} \quad (87)$$



Table 4 – Z meaning for mixed formulations

Symbol	Meaning
${}^k Z_{ij}^{\alpha_{um}\beta_{un}}$	$\bar{Q}_{ij} \int_{z_{hot}^k}^{z_{top}^k} F_{\alpha_{um}} F_{\beta_{un}} dz$
${}^k Z^{\alpha_{um}\beta_{un}}$	$\int_{z_{hot}^k}^{z_{top}^k} F_{\alpha_{um}} F_{\beta_{un}} dz$

Source: Developed by the author

Using these simplifications, Equations 88 to 111 show twenty-two stiffness matrix kernels and load vector kernels.

$$\begin{aligned}
 K_{11}^k &= {}^k Z_{11}^{\alpha_{u_1}\beta_{u_1}} \int_{\Omega} \delta u_{1\alpha_{u_1},1} u_{1\beta_{u_1},1} d\Omega + {}^k Z_{16}^{\alpha_{u_1}\beta_{u_1}} \int_{\Omega} \delta u_{1\alpha_{u_1},1} u_{1\beta_{u_1},2} d\Omega + \\
 & {}^k Z_{16}^{\alpha_{u_1}\beta_{u_1}} \int_{\Omega} \delta u_{1\alpha_{u_1},2} u_{1\beta_{u_1},1} d\Omega + {}^k Z_{66}^{\alpha_{u_1}\beta_{u_1}} \int_{\Omega} \delta u_{1\alpha_{u_1},2} u_{1\beta_{u_1},2} d\Omega
 \end{aligned} \quad (88)$$

$$\begin{aligned}
 K_{12}^k &= {}^k Z_{12}^{\alpha_{u_1}\beta_{u_2}} \int_{\Omega} \delta u_{1\alpha_{u_1},1} u_{2\beta_{u_2},2} d\Omega + {}^k Z_{16}^{\alpha_{u_1}\beta_{u_2}} \int_{\Omega} \delta u_{1\alpha_{u_1},1} u_{2\beta_{u_2},1} d\Omega + \\
 & {}^k Z_{26}^{\alpha_{u_1}\beta_{u_2}} \int_{\Omega} \delta u_{1\alpha_{u_1},2} u_{2\beta_{u_2},2} d\Omega + {}^k Z_{66}^{\alpha_{u_1}\beta_{u_2}} \int_{\Omega} \delta u_{1\alpha_{u_1},2} u_{2\beta_{u_2},1} d\Omega
 \end{aligned} \quad (89)$$

$$K_{14}^k = {}^k Z^{\alpha_{u_1}\beta_{s_1}} \int_{\Omega} \delta u_{1\alpha_{u_1}} s_{1\beta_{s_1}} d\Omega \quad (90)$$

$$K_{16}^k = {}^k Z_{13}^{\alpha_{u_1}\beta_{s_3}} \int_{\Omega} \delta u_{1\alpha_{u_1},1} s_{3\beta_{s_3}} d\Omega + {}^k Z_{36}^{\alpha_{u_1}\beta_{s_3}} \int_{\Omega} \delta u_{1\alpha_{u_1},2} s_{3\beta_{s_3}} d\Omega \quad (91)$$

$$K_{21}^k = K_{12}^{k^t} \quad (92)$$

$$\begin{aligned}
 K_{22}^k &= {}^k Z_{22}^{\alpha_{u_2}\beta_{u_2}} \int_{\Omega} \delta u_{2\alpha_{u_2},2} u_{2\beta_{u_2},2} d\Omega + {}^k Z_{26}^{\alpha_{u_2}\beta_{u_2}} \int_{\Omega} \delta u_{2\alpha_{u_2},1} u_{2\beta_{u_2},2} d\Omega + \\
 & {}^k Z_{26}^{\alpha_{u_2}\beta_{u_2}} \int_{\Omega} \delta u_{2\alpha_{u_2},2} u_{2\beta_{u_2},1} d\Omega + {}^k Z_{66}^{\alpha_{u_2}\beta_{u_2}} \int_{\Omega} \delta u_{2\alpha_{u_2},1} u_{2\beta_{u_2},1} d\Omega
 \end{aligned} \quad (93)$$

$$K_{25}^k = {}^k Z^{\alpha_{u_2}\beta_{s_3}} \int_{\Omega} \delta u_{2\alpha_{u_2}} s_{3\beta_{s_3}} d\Omega \quad (94)$$

$$K_{26}^k = {}^k Z_{23}^{\alpha_{u_2}\beta_{s_3}} \int_{\Omega} \delta u_{2\alpha_{u_2},2} s_{3\beta_{s_3}} d\Omega + {}^k Z_{36}^{\alpha_{u_2}\beta_{s_3}} \int_{\Omega} \delta u_{2\alpha_{u_2},1} s_{3\beta_{s_3}} d\Omega \quad (95)$$

$$K_{34}^k = {}^k Z^{\alpha_{u_1} \beta_{s_1}} \int_{\Omega} \delta u_{1\alpha_{u_1}, 1} s_{1\beta_{s_1}} d\Omega \quad (96)$$

$$K_{35}^k = {}^k Z^{\alpha_{u_2} \beta_{s_2}} \int_{\Omega} \delta u_{2\alpha_{u_2}, 2} s_{2\beta_{s_2}} d\Omega \quad (97)$$

$$K_{36}^k = {}^k Z^{\alpha_{u_3} \beta_{s_3}} \int_{\Omega} \delta u_{3\alpha_{u_3}} s_{3\beta_{s_3}} d\Omega \quad (98)$$

$$K_{41}^k = K_{14}^{k\ t} \quad (99)$$

$$K_{43}^k = K_{34}^{k\ t} \quad (100)$$

$$K_{44}^k = -{}^k Z_{55}^{\alpha_{s_1} \beta_{s_1}} \int_{\Omega} \delta s_{1\alpha_{s_1}} s_{1\beta_{s_1}} d\Omega \quad (101)$$

$$K_{45}^k = -{}^k Z_{45}^{\alpha_{s_1} \beta_{s_2}} \int_{\Omega} \delta s_{1\alpha_{s_1}} s_{2\beta_{s_2}} d\Omega \quad (102)$$

$$K_{52}^k = K_{25}^{k\ t} \quad (103)$$

$$K_{53}^k = K_{35}^{k\ t} \quad (104)$$

$$K_{54}^k = K_{45}^{k\ t} \quad (105)$$

$$K_{55}^k = -{}^k Z_{44}^{\alpha_{s_2} \beta_{s_2}} \int_{\Omega} \delta s_{2\alpha_{s_2}} s_{2\beta_{s_2}} d\Omega \quad (106)$$

$$K_{61}^k = K_{16}^{k\ t} \quad (107)$$

$$K_{62}^k = K_{26}^{k\ t} \quad (108)$$

$$K_{63}^k = K_{36}^{k\ t} \quad (109)$$

$$K_{66}^k = -{}^k Z_{33}^{\alpha_{s_3} \beta_{s_3}} \int_{\Omega} \delta s_{3\alpha_{s_3}} s_{3\beta_{s_3}} d\Omega \quad (110)$$

$$R_{\alpha_{u_i}}^k = \oint_{\Omega} {}^i F_{1u_i} {}^i F_{1u_i} {}^i P_{\beta_{u_i}}^t dx dy + \oint_{\Omega} {}^i F_{Nu_i} {}^i F_{Nu_i} {}^i P_{\beta_{u_i}}^b dx dy + \frac{h_k}{2} \oint_{\Omega} \int_{-1}^{+1} {}^i F_{\alpha_{s_i}} {}^i F_{\beta_{s_i}} \overline{s_n^k} dz dx dy \quad (111)$$

Demasi's work showed that, using this formulation, the elemental equilibrium equation may be written as the system of equations found in Equation 106. Where each element  $K_{ij}$ ,  $U_i$ ,  $S_i$  and  $R_i$  represent one of the nine stiffness kernels  $K$ , displacements  $U$ , out-of-plane stresses  $S$  or loads  $R$ , which compromise all different degrees of freedom corresponding to the different orders of  $N_{u_i}$  as shown in Equations 113 and 114.

The difference from the classic theory is that the out-of-plane stresses do not have associated external work loads, and as such do not produce extra load kernels, including the extra zero vectors on the right-hand vector.

$$\begin{bmatrix} K_{11} & K_{12} & 0 & K_{14} & 0 & K_{16} \\ & K_{22} & 0 & 0 & K_{25} & K_{26} \\ & & 0 & K_{34} & K_{35} & K_{36} \\ & & & K_{44} & K_{45} & 0 \\ & sym & & & K_{55} & 0 \\ & & & & & K_{66} \end{bmatrix} \begin{pmatrix} U_1 \\ U_2 \\ U_3 \\ S_1 \\ S_2 \\ S_3 \end{pmatrix} = \begin{pmatrix} R_1 \\ R_2 \\ R_3 \\ 0 \\ 0 \\ 0 \end{pmatrix} \quad (112)$$

$$U_i =$$

$$\left\{ u_{i_1}^1 \quad \dots \quad u_{i_{\alpha u_i}}^1 \quad \dots \quad u_{i_{N u_i}}^1 \quad u_{i_1}^2 \quad \dots \quad u_{i_{\alpha u_i}}^2 \quad \dots \quad u_{i_{N u_i}}^2 \quad u_{i_1}^3 \quad \dots \quad u_{i_{\alpha u_i}}^k \quad \dots \quad u_{i_{N u_i}}^{N_k} \right\}^t \quad (113)$$

$$S_i =$$

$$\left\{ s_{i_1}^1 \quad \dots \quad s_{i_{\alpha u_i}}^1 \quad \dots \quad s_{i_{N u_i}}^1 \quad s_{i_1}^2 \quad \dots \quad s_{i_{\alpha u_i}}^2 \quad \dots \quad s_{i_{N u_i}}^2 \quad s_{i_1}^3 \quad \dots \quad s_{i_{\alpha u_i}}^k \quad \dots \quad s_{i_{N u_i}}^{N_k} \right\}^t \quad (114)$$

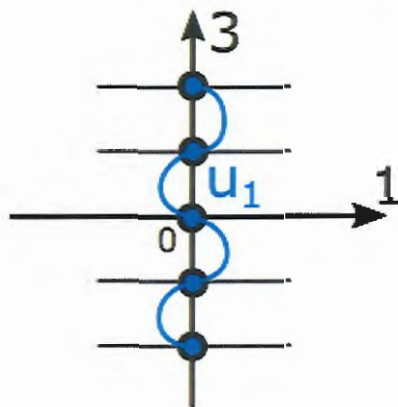
#### 4.6 Boundary conditions implementation

Over the studies of the GUF, one problem was detected with the formulation on the application of boundary conditions: the correct application of boundary conditions of

displacements over just a line or a single layer of the laminate, and the correct application of pin (simply supported) or encastre (fixed) of a complete side of the laminate.

It is possible to find unstable static solutions that increase the non-linear terms of the  $F$  and  $G$  functions unnecessarily when using penalization (Zienkiewicz and Taylor, 2000) or substitution techniques (Zienkiewicz and Taylor, 2000) to introduce the boundary conditions to the problem. This can happen because of the nature of the auto-generation  $F$  and  $G$  functions as sums of Legendre polynomials due to the imposition of the boundary and compatibility conditions. In the case of laminates, it can be considered structures under high shear stresses such as angled-plyies simulated via high-order deformation theories. Figure 26 schematizes this problem, showing possible solutions found by the formulation for angled-plyies of the type  $[\pm\theta_n]$ .

Figure 26 – Representation of possible problem of unified formulations with boundary conditions applied through penalty or substitution methods



Source: Developed by the author

The solution developed for this problem is to use Lagrange Multipliers (Kreyszig, 1999) for the application of boundary conditions. However, due to the nature of the GUF, the introduced Lagrange multipliers must have a distribution through the thickness of at least the same order as the displacement, because they need to force a given boundary. As such, Lagrange multipliers  $\lambda_{\alpha_{u_i}}$  and  $\lambda_{\alpha_{s_i}}$  are introduced as functions of the thickness using the same  $F$  and  $G$  functions as the displacements and stresses as shown in Equation 115.

$$\lambda_i^k = {}^k F_{\alpha_{u_i}} \lambda_{i\alpha_{u_i}}^k, i = 1..3; \alpha_{u_i} = 1..N_{u_i} + 1, \forall k \in \Gamma_u \quad (115)$$

This change expands the equilibrium expression as shown in Equation 116, the first expression being the equilibrium for the classic formulation and the second for mixed formulation. In addition, it changes the final system of equations to the ones found in Equation 117 and 118 for classic and mixed formulation respectively. In these equations,  $\Lambda_i$  is the vector that contains every single Lagrange multiplier used over the boundary conditions sub-domain for the  $i$ -th degree of freedom.

$$\left\{ \begin{array}{l} \int_{\Omega} \delta \varepsilon^{k^t} \sigma^k d\Omega + \int_{\Gamma_u} \delta \lambda^{k^t} u_{\alpha_{u_i}}^k d\Gamma_u = \delta L^k + \delta u_{\alpha_{u_i}}^k \lambda^{k^t} \Big|_{\Gamma_u} \\ \int_{\Omega} \int_{z_{bot}^k}^{z_{top}^k} \delta \varepsilon_m^{k^t} \sigma_m^k + \delta \varepsilon_{SG}^{k^t} \sigma_{SG}^k + \delta \sigma_{SS}^{k^t} (\varepsilon_{SS}^k - \varepsilon_{SS}^k) dz d\Omega + \int_{\Gamma_u} \delta \lambda^{k^t} u_{\alpha_{u_i}}^k d\Gamma_u = \delta L^k + \delta u_{\alpha_{u_i}}^k \lambda^{k^t} \Big|_{\Gamma_u} \end{array} \right. \quad (116)$$

$$\begin{bmatrix} K_{11} & K_{12} & K_{13} & L_1 & 0 & 0 \\ K_{21} & K_{22} & K_{23} & 0 & L_2 & 0 \\ K_{31} & K_{23} & K_{33} & 0 & 0 & L_3 \\ L_1^t & 0 & 0 & 0 & 0 & 0 \\ 0 & L_2^t & 0 & 0 & 0 & 0 \\ 0 & 0 & L_3^t & 0 & 0 & 0 \end{bmatrix} \begin{Bmatrix} U_1 \\ U_2 \\ U_3 \\ \Lambda_1 \\ \Lambda_2 \\ \Lambda_3 \end{Bmatrix} = \begin{Bmatrix} R_1 \\ R_2 \\ R_3 \\ 1 \\ 1 \\ 1 \end{Bmatrix} \quad (117)$$

$$\begin{bmatrix} K_{11} & K_{12} & 0 & K_{14} & 0 & K_{16} & L_1 & 0 & 0 \\ & K_{22} & 0 & 0 & K_{25} & K_{26} & 0 & L_2 & 0 \\ & & 0 & K_{34} & K_{35} & K_{36} & 0 & 0 & L_3 \\ & & & K_{44} & K_{45} & 0 & 0 & 0 & 0 \\ & & & & K_{55} & 0 & 0 & 0 & 0 \\ & & & & & K_{66} & 0 & 0 & 0 \\ sym & & & & & & 0 & 0 & 0 \\ & & & & & & & 0 & 0 \\ & & & & & & & & 0 \end{bmatrix} \begin{Bmatrix} U_1 \\ U_2 \\ U_3 \\ S_1 \\ S_2 \\ S_3 \\ \Lambda_1 \\ \Lambda_2 \\ \Lambda_3 \end{Bmatrix} = \begin{Bmatrix} R_1 \\ R_2 \\ R_3 \\ 0 \\ 0 \\ 0 \\ 1 \\ 1 \\ 1 \end{Bmatrix} \quad (118)$$

The  $L$  matrices are assembled as kernels in the same way as the stiffness matrices, based upon the layer kernels  $L^k$  found in the Equation 119, with the difference that they exist

only in the layers where exist a boundary condition. For example, if the selected boundary condition for a plate is simply supported, one may choose to introduce Lagrange multipliers only for the bottom most layer, which means only  $L^{k=N_{u_i}+1}$  exist.

$$L_i^k = \oint_{\Gamma_u} {}^kF_{\alpha_{u_i}} {}^kF_{\beta_{u_i}} dx dy \quad (119)$$

This procedure guarantees that the boundary conditions are applied uniformly through the whole thickness of the laminate, or only over chosen layers or lines in the macroscale model.

#### 4.7 Finite element implementation

A stand-alone implementation of this theory using a classic finite element solution, exemplified for one of the kernels in Equation 120. The element coordinate, displacements and out-of-plane shear degrees of freedom, as well as possible Lagrange multipliers, are discretized into nodal values per layer using  $\phi_n$  shape functions. While these do not need to be the same for the coordinates, displacements, stresses and Lagrange multipliers, they are taken as that for simplicity sake. For the FEM code, three possible elements were implemented: classical Hermite polynomials shape functions for linear four-node elements or quadratic nine node elements and Legendre polynomials shape functions, in which  $\xi_1$ ,  $\xi_2$  and  $\xi_3$  are local parametric coordinates varying from -1 to +1 (Bathe, 1996).

$$\begin{aligned} x_i &= x_i^n \phi_n, \quad i = 1..2, \quad x_3^k = \frac{z_{top}^k - z_{bot}^k}{2} \xi_3 + \frac{z_{top}^k + z_{bot}^k}{z_{top}^k - z_{bot}^k} \\ u_i^k &= u_i^{k,n} \phi_n, \quad s_i^k = s_i^{k,n} \phi_n, \quad \lambda_i^k = \lambda_i^{k,n} \phi_n, \quad i = 1..3 \end{aligned} \quad (120)$$

Using this discretization, each stiffness matrix and force vector kernel is easily calculated by its definitions from Equations 53 to 62 and 88 to 111 applying appropriate derivatives when necessary. Gauss integration over the plane was used with a varying order, which depends on the orders necessary for exact integration, depending on the number of nodes per element used. Equation 121 gives an example of the  $K_{26}^k$  kernel assembly and integration for the  $\alpha_{u_2}, \beta_{s_3}$  position terms of the  $u_2$  and  $s_3$  degrees of freedom. In this equation  $J$  is the jacobian matrix of the coordinate transformation from global to local  $J_{ij} = \partial x_i / \partial \xi_j$ , and  $ng$  is the Gauss integration order and  $\omega$  is the corresponding Gauss weight.

$$\begin{aligned}
 K_{26}^k(\alpha_{u_2}, \beta_{s_3}) &= {}^k Z_{23}^{\alpha_{u_2} \beta_{s_3}} \int_{\Omega} \delta u_{2\alpha_{u_2}, 2} s_{3\beta_{s_3}} d\Omega + {}^k Z_{36}^{\alpha_{u_2} \beta_{s_3}} \int_{\Omega} \delta u_{2\alpha_{u_2}, 1} s_{3\beta_{s_3}} d\Omega = \\
 & {}^k Z_{23}^{\alpha_{u_2} \beta_{s_3}} \sum_{g_2=1}^{ng} \sum_{g_1=1}^{ng} \phi_{n,2}(\xi_{g_1}, \xi_{g_2}) \phi_n(\xi_{g_1}, \xi_{g_2}) |\det J| \omega(\xi_{g_1}) \omega(\xi_{g_2}) + \\
 & {}^k Z_{36}^{\alpha_{u_2} \beta_{s_3}} \sum_{g_2=1}^{ng} \sum_{g_1=1}^{ng} \phi_{n,1}(\xi_{g_1}, \xi_{g_2}) \phi_n(\xi_{g_1}, \xi_{g_2}) |\det J| \omega(\xi_{g_1}) \omega(\xi_{g_2}) \quad (121)
 \end{aligned}$$

#### 4.8 Order optimization implementation

Different from the general implementation of unified theories found in the literature, in which the wanted order for a given variable is an input of the problem, and the kernels are preemptively generated, in the present work, a subroutine for finding the optimal orders for each case being simulated was implemented.

For that, an internal loop at the start of the damage model analysis was implemented that uses the orders  $N_{u_i}$  and  $N_{s_i}$  as variables, and this procedure generates the kernels.

For the classic formulations, the discretization orders start at linear  $N_{u_1} = N_{u_2} = N_{u_3} = 1$ . Then, inside a loop, each k-th order  $N_{u_k}$  may increase when the relative difference between stresses  $f_{ij}$ , found in Equation 122, is found to be higher than a given tolerance, when either  $i=k$  or  $j=k$ . For example, if  $f_{13}$  does not get lesser than a given tolerance for the current step, then  $N_{u_1}$  and  $N_{u_3}$  would be incremented by one. For the mixed-formulation,

analogously, the discretization orders start from linear  $N_{u_1} = N_{u_2} = N_{u_3} = N_{s_1} = N_{s_2} = N_{s_3} = 1$  and increase inside a loop until providing the same objective function in Equation 122, when the values are lower than a given tolerance. The difference lies in the fact that now, the transversal stress orders increase when the out-of-plane stresses  $\sigma_{13}$ ,  $\sigma_{23}$  and  $\sigma_{33}$  functions do not meet the criteria. Meanwhile, the displacement orders are changed when the in-plane stresses  $\sigma_{11}$ ,  $\sigma_{22}$ , and  $\sigma_{12}$  do not meet the criteria, or when the out-of-plane stresses do not meet the criteria, and the increment of the out-of-plane stresses orders does not change the relative error found by more than a given tolerance.

$$f_{ij} = \frac{\int_{z_{bot}}^{z_{top}} \sigma_{ij}^{n+1} dz}{\int_{z_{bot}}^{z_{top}} \sigma_{ij}^n dz} - 1, \text{ for } i = 1..6 \quad (122)$$

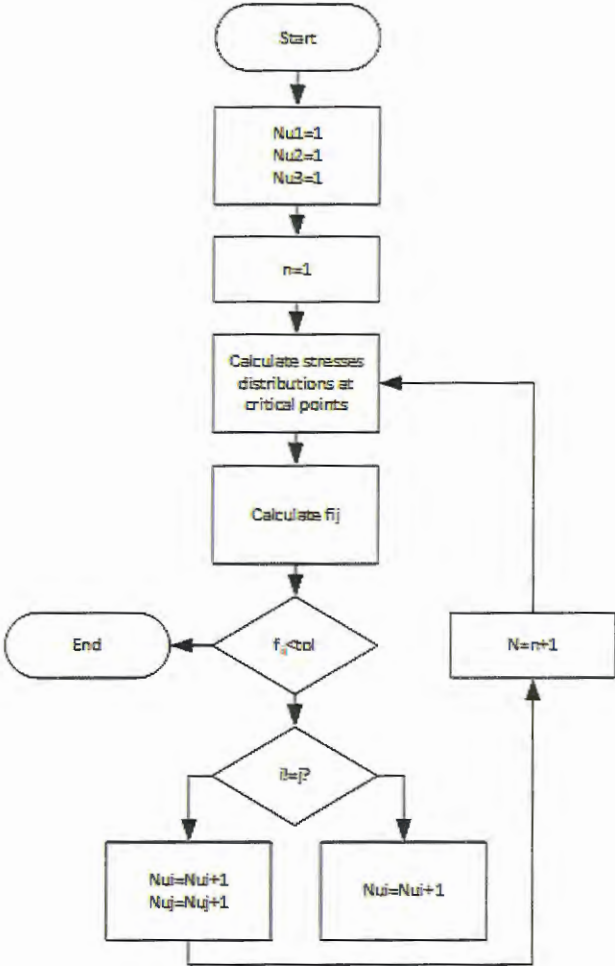
These optimization iteration loops are summarized in Figure 27 and Figure 28 for classic and mixed formulations, respectively.

This procedure guarantees that the stress/strain states calculated for the critical points, as well as its distribution over the thickness of the laminate were accurate enough to be used as boundary conditions in the microscale models. Specifically, for most of the studied cases, the in-plane displacements and out-of-plane shears were found to be needed as at least cubic per layer ( $N_{u_1} = N_{u_2} = N_{s_{13}} = N_{s_{23}} = 3$ ), and the out-of-plane displacements and in-plane stresses were taken as linear per layer ( $N_{u_3} = N_{s_{12}} = 1$ ), which in Demasi's nomenclature is the  $LW_{133}^{331}$  theory. Demasi's nomenclature for different deformation theories, which were created using the LW GUF, is given by:  $LW_{N_{u_1}N_{u_2}N_{u_3}}^{N_{s_1}N_{s_2}N_{s_3}}$ , so for example, a theory in which the in-plane displacements is taken as cubic through the thickness, and everything else is linear would be  $LW_{331}^{111}$ .

This was done from verifications with full 3D models using solid brick elements and from observations made on different works in the literature about stresses accuracy in layer-wise generalized formulations (Carrera and Ciuffreda, 2005; Qatu et al., 2010).

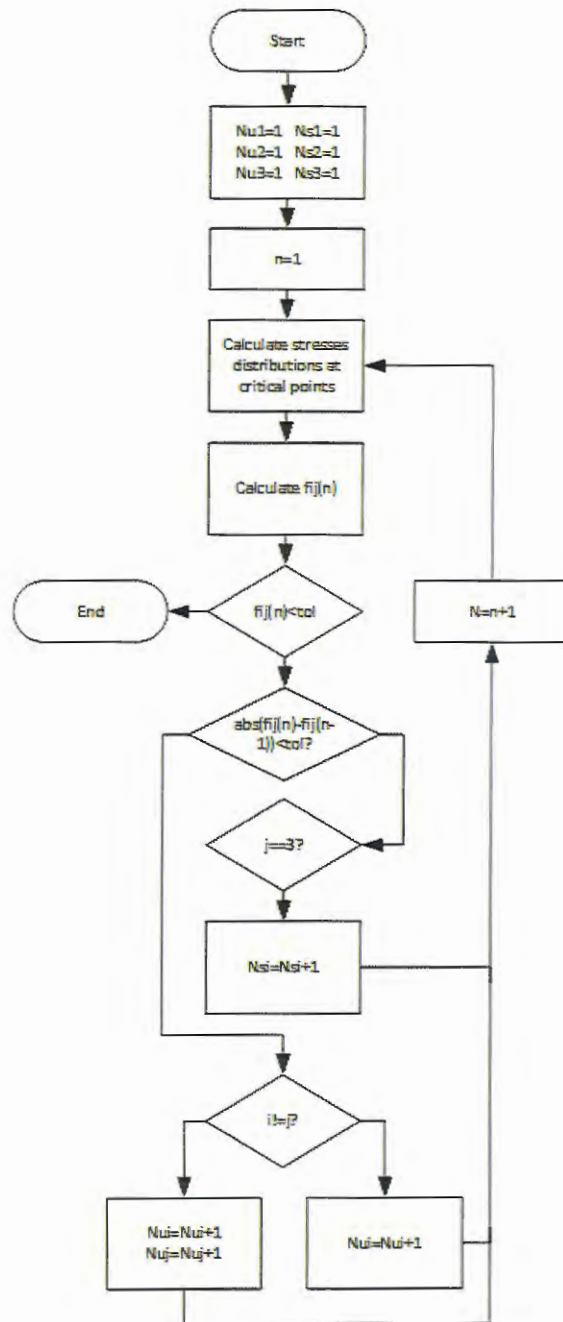


Figure 27 – Iterative loop for optimization of displacement orders for classic formulations



Source: Developed by the author

Figure 28 - Iterative loop for optimization of displacement orders for mixed formulations



Source: Developed by the author

### 4.9 Results

To study the behavior, potentialities and limitations of the proposed model, in particular the deformation theory order optimization algorithm, three numerical tests with increasingly complex geometries and loads were conducted. Four possible different lay-ups were used in the test:

- A simple unidirectional composite  $[0^8]_8$  to test the orthotropic problem;
- A cross-ply  $[0^2/90^2]_5$  and quasi-isotropic composite  $[0^2/90^2/\pm 45^2]_5$  to test the model in simple behavior, but to check for differences in stress distributions;
- A laminate unbalanced and asymmetric  $[(+30^-/-60^+)_4]_4$  to test the limitations of the model.

All tests were made with a material containing properties as shown by Table 5, and in the results all cases were compared for several deformation theories, which are represented as such:

- three digits correspond to a classical theory, which represent the orders of  $u_1$ ,  $u_2$  and  $u_3$  respectively (for example, 324 means a cubic deformation theory for  $u_1$ , quadratic for  $u_2$  and fourth order for  $u_3$ );
- six digits correspond to a mixed formulation, which represents the orders of  $u_1$ ,  $u_2$ ,  $u_3$ ,  $s_1$ ,  $s_2$  and  $s_3$  (for example, 332331 means a cubic deformation theory for  $u_1$ ,  $u_2$ ,  $s_1$  and  $s_2$ , quadratic for  $u_3$  and linear for  $s_3$ ).

Table 5 - Geometric and material properties for the numerical tests

Property	E1 [GPa]	E2 [GPa]	G12 [GPa]	G23 [GPa]	$\nu_{12}$	$\nu_{23}$	Lx [mm]	Ly [mm]	h [mm]
Value	127	10.3	5.4	3.05	0.34	0.306	100	100	0.8

Source: Developed by the author

All tests were evaluated using Abaqus™ tridimensional brick elements considering a fine mesh that passed in convergence tests with at least 8 (eight) C3D20 quadratic elements through the thickness of each layer. Results were also compared to Abaqus™ S8 bidimensional shell elements and, when possible, to analytical solutions given by Reddy and Ochoa (1996). It should be noted Abaqus™ S8 elements use an equivalent single layer formulation, and as such, may not display a complete stress distribution through the thickness of the laminate.

The meshes were chosen to be sparse enough so that the deformation theories would influence the results, but still within a mesh convergence range. This was chosen for both Classic and Mixed Model showing the effects of the high order theories on the accuracy of the solutions, and to check the possibility of using the minimum discretized possible mesh, mainly for the case that the FEM code run within the multiscale methodology for computational efficiency sake.

#### 4.9.1 First Test: Flat rectangular plate under pure tensile loads

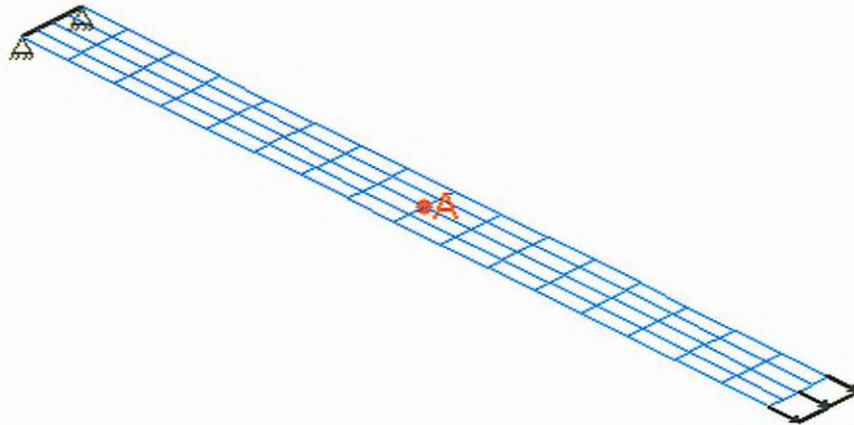
The first numerical tests consisted of a simple case to validate the model against Abaqus: a flat rectangular plate with dimensions 175 x 25 mm, following ASTM 3039 testing parameters for 90° unidirectional composite tensile tests, however with a total thickness of 50 mm to test the capabilities of the model for thick plates. The plate was fully encastred in the  $x=0$  edge and a uniform distributed normal tensile load of 1 N/mm was applied to the  $x=175$  mm top edge as shown in Figure 29. The mesh used was 16 x 4 elements, which generated an  $L/h$  elemental ratio of 4.571. This plate is regarded as a thick plate ( $L/h < 10$ ), but still away from extreme edge cases ( $L/h \cong 1$ ). Only a single center (A) point was chosen as a possible optimization point due to the almost uniform behavior of the structure, ignoring some Poisson effects. The results for the displacement at the center of the plate, as well as the maximum normal stress value at the 90° upper layer in the fiber direction are found from Table 6 to Table 9.

Table 6 - Results for First Numerical Test – Classic Model. Maximum normal stress value at critical layer in MPa. Simple lay-ups.

Discretization Orders	Lay-up	
	[0] <sub>8</sub>	[0 <sub>2</sub>  90 <sub>2</sub> ] <sub>s</sub>
111	1.1262	0.1844
221	1.1262	0.1844
222	1.0904	0.1929
331	1.1232	0.1844
333	1.1876	0.1705
<b>Optimal – 332</b>	<b>1.1262</b>	<b>0.1844</b>
<b>Abaqus™ 2D</b>	<b>1.2260</b>	<b>0.1836</b>
<b>Abaqus™ 3D</b>	<b>1.1208</b>	<b>0.1674</b>

Source: Developed by the author

Figure 29 – First numerical test



Source: Developed by the author

Table 7 – Results for First Numerical Test – Classic Model. Maximum normal stress value at critical layer in MPa. Complex lay-ups.

Discretization Orders	Lay-up							
	[0/90/+45]s				[(30/-60)4]T			
Order	u [10-5mm]	s [10-2MPa]	Dofs	Time [s]	u [10-5mm]	s [10-2MPa]	Order	u [10-5mm]
111	4.0034	1.1178	2,040	2.57	8.9750	7.7295	111	4.0034
221	4.0305	1.1254	3,230	9.12	9.0357	7.7817	221	4.0305
222	4.0380	1.1275	3,825	13.28	9.0525	7.7963	222	4.0380
331	4.0410	1.1283	4,420	17.86	9.0592	7.8020	331	4.0410
332	4.0480	1.1303	5,015	24.75	9.0750	7.8156	332	4.0480
333	4.0481	1.1303	5,610	30.40	9.0752	7.8158	333	4.0481
555	4.0836	1.1402	9,180	91.66	9.1548	7.8844	555	4.0836
<b>Opt A - 331</b>	<b>4.0480</b>	<b>1.1303</b>	-	-	<b>9.0750</b>	<b>7.8156</b>	<b>Opt A - 331</b>	<b>4.0480</b>
<b>Abaqus™ 2D</b>	<b>4.1760</b>	<b>1.1326</b>	<b>4,429</b>	<b>3.17</b>	<b>8.975</b>	<b>7.7295</b>	<b>Abaqus™ 2D</b>	<b>4.1760</b>
<b>Abaqus™ 3D</b>	<b>3.9450</b>	<b>1.1318</b>	<b>44,800</b>	<b>474.20</b>	<b>9.0870</b>	<b>7.8260</b>	<b>Abaqus™ 3D</b>	<b>3.9450</b>

Source: Developed by the author

Table 8 - Results for First Numerical Test – Mixed Model. Maximum normal stress value at critical layer in MPa. Simple lay-ups.

Discretization Orders	Lay-up	
	[0] <sub>8</sub>	[0 <sub>2</sub>  90 <sub>2</sub> ] <sub>s</sub>
111111	1.1262	0.1358
111221	1.1262	0.1358
111331	1.1262	0.1252
222111	1.0886	0.1815
222222	1.0893	0.1929
221331	1.1231	0.1891
333111	1.2203	0.1733
333333	1.1876	0.1695
555555	1.1954	0.1682
<b>Optimal - 332112</b>	<b>1.1262</b>	<b>0.1855</b>
<b>Abaqus™ 2D</b>	<b>1.2260</b>	<b>0.1836</b>
<b>Abaqus™ 3D</b>	<b>1.1208</b>	<b>0.1674</b>

Source: Developed by the author

Table 9 - Results for First Numerical Test – Classic Model. Maximum normal stress value at critical layer in MPa. Complex lay-ups.

Discretization Orders	Lay-up							
	[0/90/+45] <sub>s</sub>				[(30/-60) <sub>4</sub> ] <sub>T</sub>			
Order	u [10-5mm]	s [10-2MPa]	Dofs	Time [s]	u [10-5mm]	s [10-2MPa]	Dofs	Time [s]
111111	4.4438	1.1178	4,590	2.57	8.9750	7.7295	4,590	1.164536706
111221	4.3832	1.0975	8,223	19.59	8.8119	7.5890	8,223	8.881497267
111331	4.3931	1.0825	9,753	25.72	8.6917	7.4855	9,753	11.66079905
222111	4.3936	1.0850	11,283	23.92	8.7114	7.5025	11,283	10.84386797
222222	4.6296	1.0851	12,813	29.56	8.7123	7.5033	12,813	13.39902006
221331	4.1868	1.1434	14,343	36.91	9.1804	7.9064	14,343	16.73175166
333111	4.2840	1.0341	23,523	130.41	8.3023	7.1502	23,523	59.11726123
333333	4.1798	1.0580	34,594	291.22	8.4950	7.3161	34,594	132.0110476
555555	4.1868	1.0323	56,734	840.73	8.2883	7.1381	56,734	381.1063556
<b>Opt A - 331</b>	<b>4.1798</b>	<b>1.0341</b>	-	-	<b>8.3023</b>	<b>7.2703</b>	-	-
<b>Abaqus™ 2D</b>	<b>4.1760</b>	<b>1.0635</b>	<b>4,429</b>	<b>6.10</b>	<b>8.975</b>	<b>7.7295</b>	<b>4,429</b>	<b>6.10</b>
<b>Abaqus™ 3D</b>	<b>3.9450</b>	<b>1.0736</b>	<b>44,800</b>	<b>474.20</b>	<b>8.6199</b>	<b>7.4237</b>	<b>44,800</b>	<b>474.20</b>

Source: Developed by the author

The results showed good accuracy between the proposed model optimal deformation theory and both Abaqus™ solutions. For lower orders displacements – such as the linear 111xxx – the change in the order of the out-of-plane stresses did not change the result much. This is expected due to the nature of the lay-ups and load cases chosen for this preliminary

study, and future research will investigate this problem under harsher loads and with lay-ups that incurs higher shear loads.

Another relevant result was that for higher order in the displacements, starting with quadratic 222xxx theories, but more noticeable in cubic 333xxx theories, is that, for such powerful description of the deformation, a better description of the out-of-plane stresses did not change the results. This can be explained due to Reissner Mixed Variational Theory, due to the geometric and constitutive terms of the out-of-plane deformations may cancel each other in the virtual out-of-plane shear terms, if the geometric deformation is precise enough by itself.

Finally, for the three studied lay-ups, the found optimized theory has in-plane cubic displacements and quadratic transversal displacement 332xxx with full integration. These theories are analogous to Reddy's plate theory. And this result may indicate that cubic deformation theories are enough for obtaining accurate shear distributions of the thickness for the proposed load cases in LW theories. Future studies are required to verify if this hypothesis holds true for harsher load cases, equivalent single layer theories and classic theories.

#### 4.9.2 Second Test: Flat square plate under transversal pressure

The second numerical tests consisted of a flat square plate with dimensions 250 x 250 mm with a total thickness of 50 mm to test the capabilities of the model for thick plates. The plate was simply supported in the  $x=0$ ,  $x=250$ ,  $y=0$  and  $y=250$  edges as shown in Figure 30. At first, the plate was simulated under a uniform pressure load and then under a bisinoidal pressure load with maximum amplitude of  $1 \text{ N/mm}^2$ . Both pressure cases were applied to the top surface. The mesh used was  $16 \times 16$  elements, which generated an  $L/h$  elemental ratio of 3.2, on the same  $L/h$  range as the First Test. Four points were chosen for the optimization process: (A) at the center of the plate, (B) at  $(L/4, L/4)$ , (C) at  $(L/8, L/4)$  and (D) at  $(3L/4, L/4)$  to study the influence of the control point over the algorithm. Points (B) and (D) were tested because, even with the symmetry of the geometry, unbalanced laminates such as the  $[(+30^\circ/-60^\circ)_4]$  cases may generate different results. The results for the transversal displacement at the

center of the plate as well as computational times and number of degrees of freedom generated for each case are shown in Table 10 to Table 13.

Figure 30 – Second numerical test

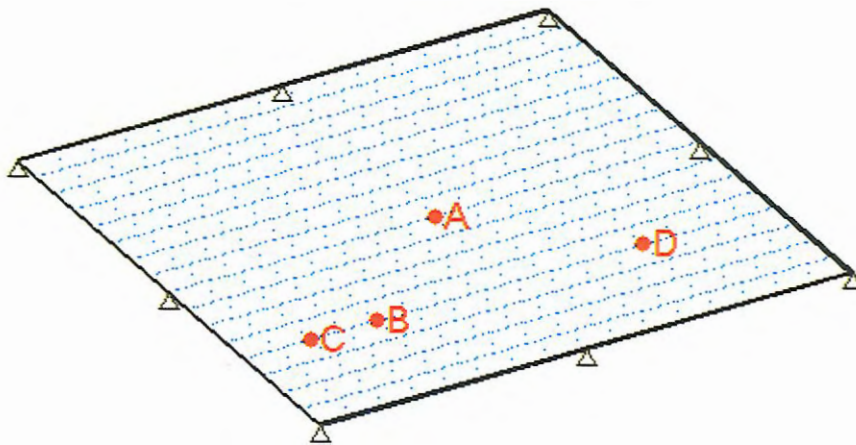


Table 10 - Results for Second Numerical Test – Bisinoidal Case – Classic Model. Transversal displacement at the center of the plate.

Discretization Orders	Lay-up					
	[0/90/+45] <sub>s</sub>			[(+30/-60) <sub>4</sub> ] <sub>T</sub>		
Formulation	w [10 <sup>-2</sup> mm]	Dofs	Time [s]	w [10 <sup>-2</sup> mm]	Dofs	Time [s]
111	4.1571	6936	12.16	4.0159	7803	19.80
221	4.1852	10982	43.15	4.0483	12427	57.90
222	4.1930	13005	62.86	4.0553	14739	76.79
331	4.1961	15028	84.52	4.0505	17051	104.97
332	4.2034	17051	117.13	4.0574	19363	147.83
333	4.2035	19074	143.88	4.0576	21675	196.51
555	4.2404	31212	433.86	4.0576	35547	333.99
A332	4.2034	-	-	4.05614	-	-
B323	4.2120	-	-	4.05675	-	-
C233	4.2120	-	-	4.05675	-	-



Abaqus™ 2D	4.3700	1734	15	4.5579	1734	15
Abaqus™ 3D	4.2470	63291	907	4.4399	63291	907
Analytical	4.2248	-	-	4.0159	-	-

Source: Developed by the author

Table 11 - Results for Second Numerical Test – Bisinoidal Case – Mixed Model. Transversal displacement at the center of the plate.

Discretization Orders	Lay-up					
	[0/90/+45] <sub>s</sub>			[(+30/-60) <sub>4</sub> ] <sub>T</sub>		
Formulation	w [10-2mm]	Dofs	Time [s]	w [10-2mm]	Dofs	Time [s]
111111	4.59458	7020	15.12	4.65811	7020	16.10
111221	4.51106	9100	26.81	4.57344	9100	27.18
111331	4.44956	11180	39.27	4.51108	11180	39.81
222111	4.45964	10140	32.48	4.52130	10140	32.93
222222	4.46012	13260	54.39	4.52179	13260	55.14
221331	4.69972	13260	55.18	4.76470	13260	55.94
333111	4.25022	13260	56.00	4.30899	13260	56.77
333333	4.34885	19500	125.05	4.40898	19500	126.78
555555	4.24306	31980	361.01	4.30173	31980	366.00
A331331	4.25022	-	-	4.30899		
B321331	4.37142	-	-	4.43186		
C321331	4.41281	-	-	4.47383		
D231331	4.41281	-	-	4.47383		
Abaqus™ 2D	4.37000	1734	15	4.43042	1734	15
Abaqus™ 3D	4.24700	63291	907	4.30572	63291	907
Analytical	4.22480	-	-	4.28322	-	-

Source: Developed by the author

Table 12 - Results for Second Numerical Test – Uniform Case – Classic Model. Transversal displacement at the center of the plate.

Discretization Orders	Lay-up					
	[0/90/+45] <sub>s</sub>			[(+30/-60) <sub>4</sub> ] <sub>T</sub>		
Formulation	w [10-2mm]	Dofs	Time [s]	w [10-2mm]	Dofs	Time [s]
111	2.40339	6936	18.40	2.58696	6936	16.10
221	2.41963	10982	32.63	2.60783	10982	33.08
222	2.42414	13005	47.79	2.61234	13005	48.45
331	2.42593	15028	39.53	2.60924	15028	40.07
332	2.43015	17051	66.19	2.61369	17051	67.10
333	2.43021	19074	67.15	2.61379	19074	68.08
555	2.45155	31212	68.15	2.61383	31212	69.09
A331	2.43015	-	-	2.61577	-	

B321	2.43513	-	-	2.62112	-	
C321	2.43513	-	-	2.62112		
D231	2.52647	-	-	2.71944		
Abaqus™ 2D	2.52647	1734	15	2.71944	1734	15
Abaqus™ 3D	2.45536	63291	907	2.64290	63291	907

Source: Developed by the author

Table 13 - Results for Second Numerical Test – Uniform Case – Mixed Model. Transversal displacement at the center of the plate.

Discretization Orders	Lay-up					
	[0/90/+45] <sub>s</sub>			[(+30/-60) <sub>4</sub> ] <sub>T</sub>		
Formulation	w [10-2mm]	Dofs	Time [s]	w [10-2mm]	Dofs	Time [s]
111111	7.54635	7020	14.00	7.67623	7020	16.10
111221	7.40917	9100	38.95	7.53669	9100	44.79
111331	7.30816	11180	57.05	7.43394	11180	65.61
222111	7.32472	10140	47.19	7.45078	10140	54.26
222222	7.32550	13260	79.02	7.45159	13260	90.87
221331	7.71903	13260	80.17	7.85189	13260	92.19
333111	6.98075	13260	81.36	7.10090	13260	93.56
333333	7.14275	19500	181.67	7.26569	19500	208.92
555555	6.96899	31980	524.47	7.08894	31980	603.14
A331331	6.98075	-	-	7.10090	-	-
B321331	7.17982	-	-	7.30339	-	-
C321331	7.24780	-	-	7.37254	-	-
D231331	7.24780	-	-	7.37254	-	-
Abaqus™ 2D	7.17749	1734	15	7.30102	1734	15
Abaqus™ 3D	6.97547	63291	907	7.09552	63291	907

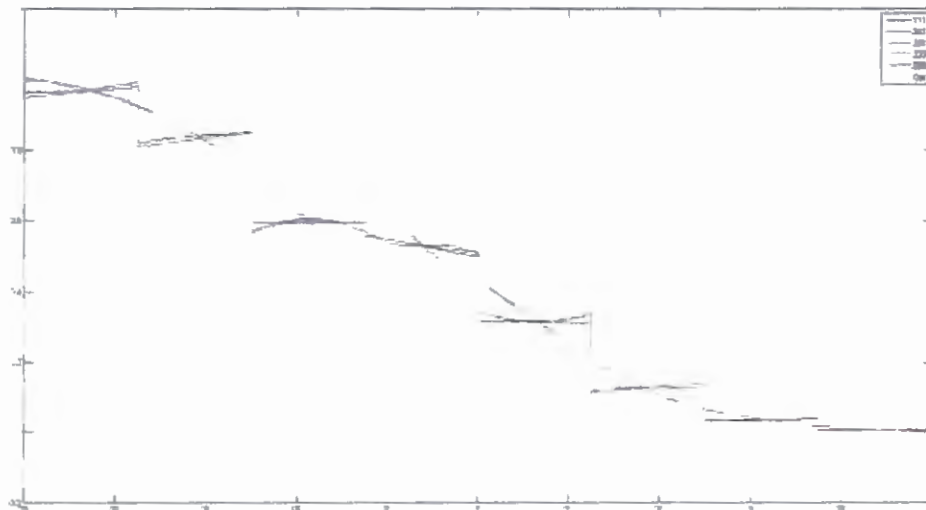
Source: Developed by the author

For the Second test the results also presented a good correlation between the proposed model, Abaqus™ and analytical solutions when applicable. As predicted, both the uniform and bisinoidal cases showed similar results for both the classic and mixed formulation models. The number of degrees of freedom through the evolution of the models can be seen, and its impact on the solution time. One thing to note is that even in the most extreme case studied, the 555, which had about half the number of degrees of freedom of the 3D Abaqus™ model (31212 against 63291 respectively), but it had a computational time 72.16% lower on average than the Abaqus™ model. This shows that the Python implementation did fulfill the efficiency objective criteria.

For the classic model, the results showed a trend of converging for Abaqus™ 3D solution with the increase in order, most notably the increase in the plane displacements  $u_1$  and  $u_2$ , but the  $u_3$  is not influenced.

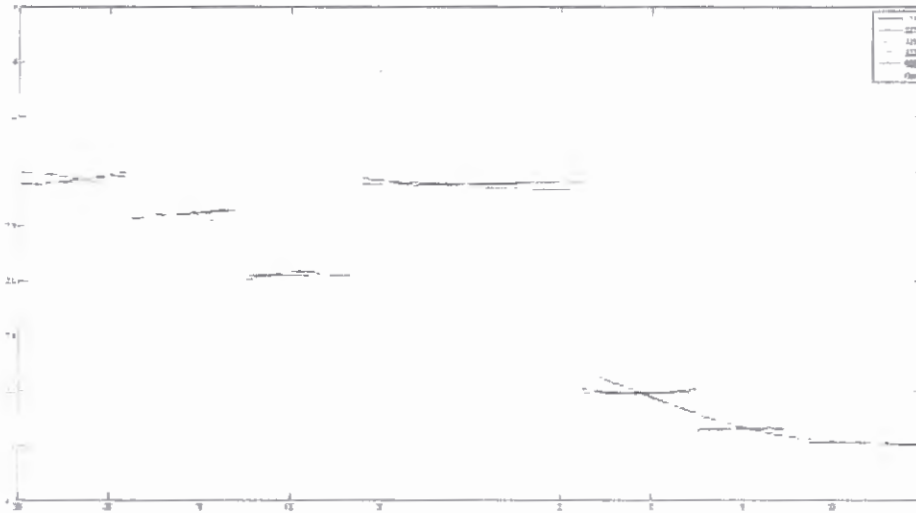
For the mixed model, the results are more complex to analyze and also more relevant. There was no clear convergence between the increase of orders in the shear stresses and the comparison to Abaqus™ or analytical results, and again the  $u_1$  and  $u_2$  displacement orders seemed to be mandatory on the answer. However, the increase in the shear stresses order created a minor convergence towards the 3D result, and when both occurred at the same time, the end results, especially for the non-symmetrical optimization points (B), (C) and (D), happened faster and if not more accurately than the classic results. However, given the small difference between the displacement results for all models when comparing to Abaqus™'s 3D solution, the faster convergence of the mixed optimization may be preferred. To better evaluate this proposition, the stress distribution for the bisinoidal case, for different models and optimization point C was gathered and shown in Figure 31 and Figure 34.

Figure 31 –  $\sigma_{13}$  Stress distribution over the thickness for different theories, Classic Case, Point C, [(+30/-60)4]<sub>T</sub> lay-up



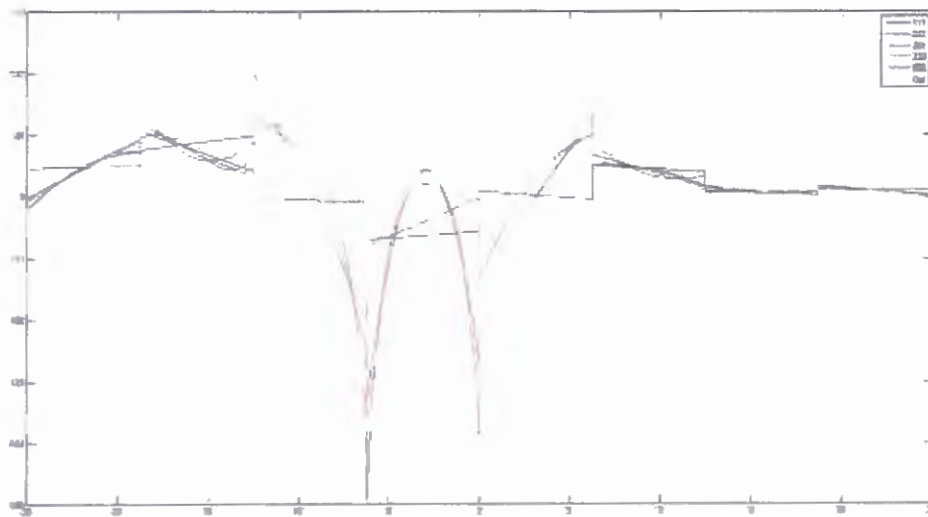
Source: Developed by the author

Figure 32 -  $\sigma_{23}$  Stress distribution over the thickness for different theories, Classic Case, Point C, [(+30/-60)4]<sub>T</sub> lay-up



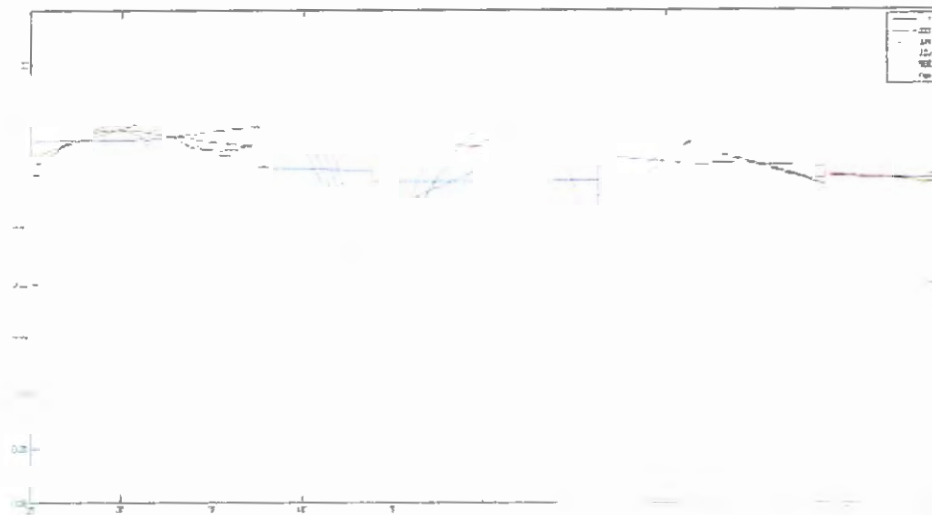
Source: Developed by the author

Figure 33 -  $\sigma_{13}$  Stress distribution over the thickness for different theories, Classic Case, Point C, [0/90/+45]<sub>s</sub> lay-up



Source: Developed by the author

Figure 34 -  $\sigma_{23}$  Stress distribution over the thickness for different theories, Classic Case, Point C,  $[0/90/+45]_s$  lay-up



Source: Developed by the author

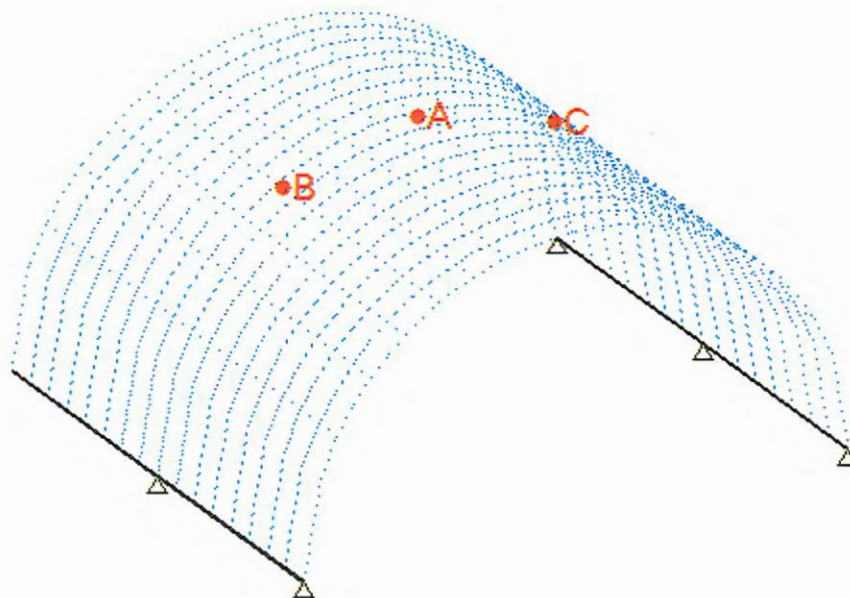
The influence of the order of the deformation theory over the stress distributions can be seen. In particular, the higher order theories influence is greater on the  $[(+30/-60)_4]_T$  lay-up, even if it exists on both. One thing to notice is when the higher order was used then the higher stress concentration over the interface between layers was found, as well as higher maximum stress values.

#### 4.9.3 Third Test: Half cylinder under uniform pressure

The third numerical tests consisted of a half cylinder shell with dimensions 150 x 162 mm with a radius of 75 mm and a total thickness of 50 mm to test the capabilities of the model for thick plates. The cylinder was simple supported in the edges as shown in Figure 35. The cylinder was simulated under a uniform pressure load of 1 N/mm<sup>2</sup> on the top surface. The mesh used consisted of 16 x 16 elements, which generated an  $L/h$  elemental ratio of approximately 4.0, on the same  $L/h$  range as the First and Second Tests. Three points were chosen for the optimization process: (A) at the center of the cylinder, (B) and (C) at the same line and radially distance  $\pm 30^\circ$ , respectively to study the influence of the control point over

the algorithm. Again, like the flat plate under pressure, Points (B) and (C) were tested because, even with the symmetry of geometry, unbalanced laminates such as the  $[(+30^\circ/-60^\circ)_4]$  cases may generate different results. The results for the transversal displacement at the center of the plate as well as computational time and number of degrees of freedom generated for each case are shown in Table 14 and Table 15. These results showed a similar response from the plane ones, and show the capacity of the implemented formulation to simulate curved surfaces.

Figure 35 – Third numerical test



Source: Developed by the author

Table 14 - Results for Third Numerical Test – Uniform Case – Mixed Model. Transversal displacement at the center of the plate.

Discretization Orders	Lay-up					
	[0/90/+45] <sub>s</sub>			[(+30/-60) <sub>4</sub> ] <sub>T</sub>		
Formulation	w [mm]	Dofs	Time [s]	w [mm]	Dofs	Time [s]
111	0.397340	3960	119.3	0.397340	3960	1.16E+02
221	0.397554	7095	909.821	0.400026	7095	4.12E+02
222	0.397938	8415	1194.53	0.400771	8415	6.01E+02
331	0.397650	9735	1110.85	0.585143	9735	551.789
332	0.397939	11055	1372.5959	0.401765	11055	1.12E+03
333	0.397942	12375	1714	0.585708	12375	915.07599
555	0.397942	20295	6055.986	0.585708	20295	3115.302
A332	0.401765	-	-	0.401765	-	-
B333	0.402587	-	-	0.402587	-	-
C233	0.402301	-	-	0.402301	-	-
Abaqus™ 2D	0.417689	16574	143.372	0.417689	16574	143.37
Abaqus™ 3D	0.405933	604942	8669.202	0.405933	604942	8669.20

Source: Developed by the author

Table 15 - Results for Third Numerical Test – Uniform Case – Mixed Model. Transversal displacement at the center of the plate.

Discretization Orders	Lay-up					
	[0/90/+45] <sub>s</sub>			[(+30/-60) <sub>4</sub> ] <sub>T</sub>		
Formulation	w [mm]	Dofs	Time [s]	w [mm]	Dofs	Time [s]
111111	0.439155	2004	60.37	0.446713	2004	58.82
111221	0.431172	3590	460.42	0.438593	3590	208.71
111331	0.425294	4258	604.50	0.432614	4258	304.05
222111	0.426257	4926	562.15	0.433594	4926	279.24
222222	0.426303	5594	694.61	0.433640	5594	566.55
221331	0.449204	6262	867.38	0.456936	6262	463.08
333111	0.406241	10270	3064.66	0.413232	10270	1576.52
333333	0.415668	15104	6843.50	0.422822	15104	3520.41
555555	0.405556	24770	19756.69	0.412536	24770	10163.17
A331331	0.406241	-	-	0.413232	-	-
B321331	0.417825	-	-	0.425016	-	-
C321331	0.421781	-	-	0.429040	-	-
Abaqus™ 2D	0.417689	16574	143.372	0.424878	16573.75478	143.3715812
Abaqus™ 3D	0.405933	604942	8669.202	0.412919	604942.0495	8669.201607

Source: Developed by the author





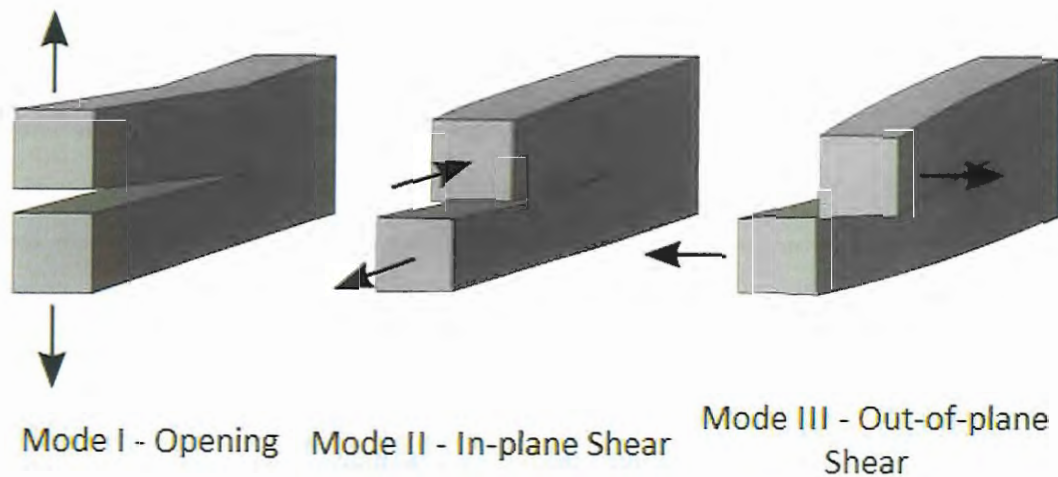
## 5 MICROSCALE MECHANICAL MODELS: DAMAGE EVOLUTION AND HOMOGENIZATION

---

This chapter presents the models and methodologies used in the microscale analysis phase of the proposed methodology, as well as its detailed implementation. That is, the concepts, models and simulations used and implemented using automated Python scripts within the commercial finite element package Abaqus™ v6.14-1 for obtaining damage parameters and homogenized elastic properties. As previously discussed in Chapter 3. Multiscale Methodology, the author used the general approach presented by Singh and Talreja (2010). With this in mind, this chapter presents the concepts, equations and methodology for numerically obtaining damage parameters, as well as adaptations and new solutions to problems found during analysis.

First, defining a crack as two separate traction free surfaces that appear in a material because of damage effects, crack propagation can occur in three different ways defined as called Mode I, Mode II and Mode III failures, and schematized in Figure 36a, Figure 36b, and Figure 36c respectively. Mode I, or opening mode, happens when a crack propagates because the applied external loads opens the crack through the work of tensile stresses normal to the crack surface planes. Mode II, or sliding mode, happens when a crack propagates because of the work of shear stresses parallel to the plane of the crack surfaces and perpendicular to the crack front, “sliding” the two crack surfaces away from each other. Mode III, or tearing mode, happens due to the work of shear stresses parallel to both the crack surfaces and crack front, distorting and twisting each crack surface in different directions.

Figure 36 – Crack propagation Modes



Source: Developed by the author, adapted from Wikipedia (2017)

Two studied problems were the influence of Crack Sliding Displacements (CSD) and subsequent crack multiplication under shear (Mode II) and problems that arose from the microscale models geometry. At first, and during preliminary studies and the CSD analyses, hexahedral RVEs were used. However, their usage with angled-ply and some specific cases of crack geometries created boundary conditions problems that will be addressed in the chapter. As a solution for these problems, a new geometry generation methodology for the RVE was proposed. Instead of hexahedra, prismatic polyhedrons were implemented, created from cutting planes aligned to the direction of the principal direction of fibers of the laminate layers. Furthermore, a new approach to the imposition of the boundary conditions for this new geometry was needed, especially for the case of homogenization analysis. This new approach was based upon the works of Danielsson et al. (2002) over periodic boundary conditions applied to polyhedral generated from pairs of parallel planes.

Following that, the chapter shows the homogenization technique used for damaged materials and how the degenerated elastic properties are linked to the macroscale analysis. After, results for validation of the model for both the homogenization technique and the damage evolution algorithm are presented. And, the validation process is based on data found in the literature, which are analytical solutions or experimental tests.

## 5.1 COD damage evolution model overview

For the prediction and simulation of damage evolution of composite laminates under tensile loads, a methodology based on continuum fracture mechanics, and using the general idea found in several different works (Varna et al. 2009, Joffe and Varna, 2001; Singh and Talreja, 2010; Maimí et al. 2011a and Maimí et al. 2011b) is proposed. These methodologies focus on the use of damage metrics based on Continuum Fractures Mechanics (CFM) concepts, in particular, crack density and work to open and/or close cracks for the intralaminar damage prediction, and energy release rates for delamination propagation.

In addition, due to the extensive research on the problem of finding homogenized properties in damaged materials by using several known methods, such as finite element analysis of RVEs, holistic approaches, and asymptotic homogenization, the problem of obtaining degraded elastic properties has become trivial, given that one knows the crack profile in a hexahedron, which represents the RVEs. As such, the main problems resides in how to obtain ways to link the macroscopic metrics – such as applied load or displacement – to the microscopic damage metrics – such as crack spacing, crack density, delaminated area, and local stress and/or strain state.

For the present work, the methodology used for the evaluation of intralaminar damage evolution in composite materials will, mainly, be based upon the methodology proposed (Varna et al. 2009, Joffe and Varna, 2001; Singh and Talreja, 2010), with some new adaptations and generalizations for both bending loads and general laminates, such as angled-ply and asymmetrical lay-ups never incorporated in previous work.

This methodology proposes that every single intralaminar failure mechanism, which creates and evolves damage, but do not generate failure or loss of cohesion in the material, for composites materials manufactured from unidirectional layers may be modelled as trespassing matrix cracks parallel to the orientation of the fibers in a given layer. Moreover, the number of cracks for each layer and its multiplication is not directly dependent of the damage in other layers. The only influence damage in a neighbor layer may have in another layer is the local change in stress/strain states that the second layer displays, and as such, the energy available to that layer to create new cracks. As such, the crack density  $\lambda$ , which is the number of cracks found in a given layer per length, characterizes the damage in a given layer.

The use of trespassing cracks over the model incurs the hypothesis that, after the formation of a crack over the thickness of a whole bundle of layers of the same direction, the crack grows unstably in the direction parallel to the fiber directions. This behavior has been shown both analytically (Pupurs et al., 2013) and numerically (Zhuang et al., 2016).

These microscale models are used to calculate different damage metrics. Specifically, a two-state approach is introduced, in which damage evolves from a state with a crack density of  $\lambda_1$  – state 1 – to a state with a crack density of  $\lambda_2 = 2\lambda_1$  – state 2. This process is exemplified for a  $60^\circ$  layer in Figure 37.

Figure 37 - Example of process of damage evolution through increase in crack density in the microscale model for a  $[\pm 60^\circ_4]_s$  laminate

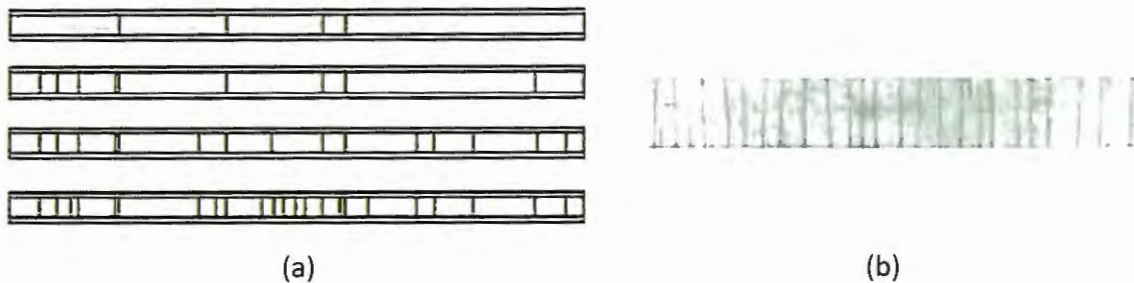


Source: Developed by the author

This approach has been used for some decades in CFM analysis, and is based on the premise that intralaminar damage evolution occurs in two distinct phases. In the first phase, the cracks are formed more or less randomly over the layer area, due to the non-uniformity of fibers, and presence of defects, but far away from each other that two cracks do not interact. This happens as, statistically, there is a greater area way from the influence previous cracks that may have a microscopic region, which is beneficial to the creation of a new crack, for example, containing a cluster of fibers, a resin rich area, or an abundance of voids. This first phase of crack multiplication evolution is shown in Figure 38. As damage progresses and more cracks are formed, the material follows the second phase of damage multiplication, in which the cracks are abundant enough, but their region of influence over the stress state is small enough, that statically, the area with the higher probability of new crack formation is the area in the middle of two existing cracks. Maimi et al. (2010a) showed that the low distance of crack influence was found analytically by several researchers, and was verified numerically in the

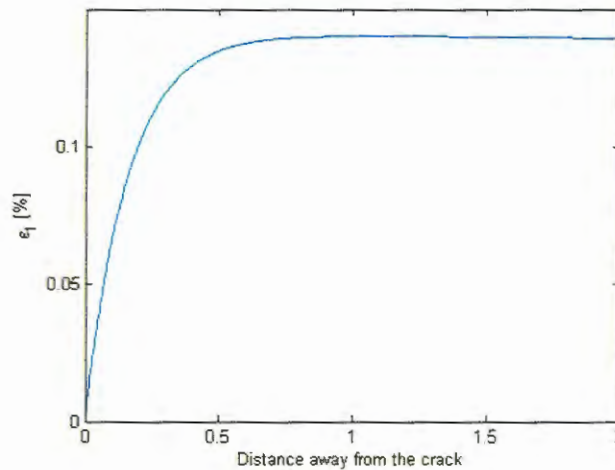
present work. Figure 39 show the distribution of the principal strain value against distance away from a crack in a cross-ply, normalized by the thickness of the layer. It shows how the influence of the crack quickly goes to the nominal value about 50% of the layer thickness.

Figure 38 – (a) Schema of the first phase of crack multiplication; (b) Experimental results showing periodicity in multiple cracks



Source: Singh and Talreja, 2014

Figure 39 - Principal strain at the center of a cracked layer over the distance away from the crack in a  $[0^\circ/90^\circ_2]_S$  laminate

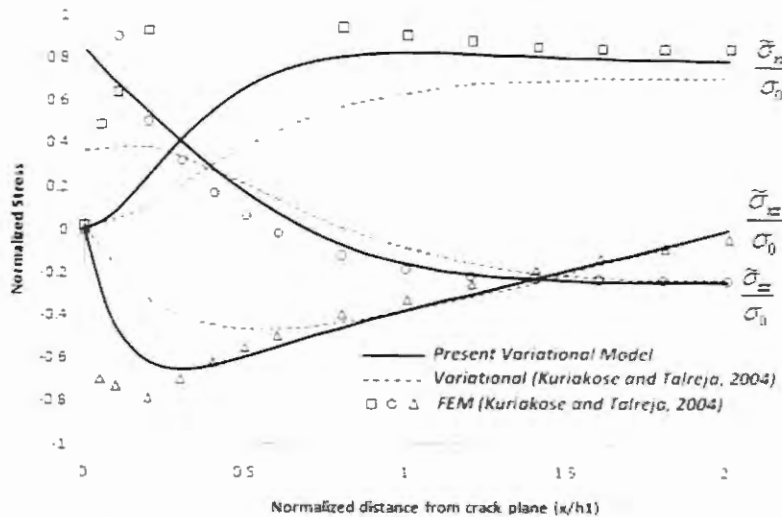


Source: Developed by the author

Analytically, Hajikezami et al. (2015) also found similar results for bending loads, shown in Figure 40, that close to the distance equal to the thickness of the layer, the normal stresses recover stabilization at a nominal value. These two phases of crack multiplication lead to a crack profile with periodic distance between layers, which was found experimentally by

several distinct researchers using damaged glass-fiber/epoxy composites under a background light as shown in Figure 38b.

Figure 40 - Analytical stresses away from the crack center under bending for a  $[90^\circ/0^\circ]_s$  laminate

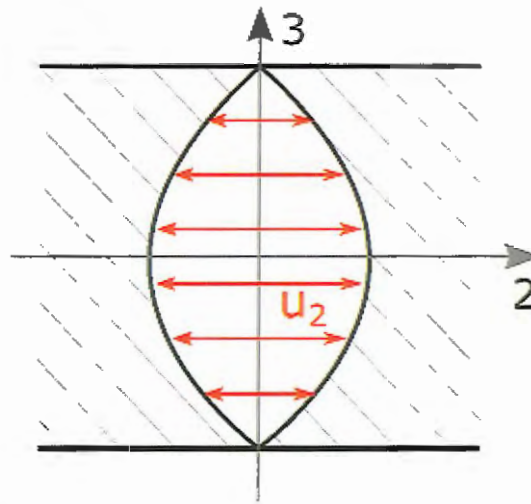


Source: Hajikezami et al. (2015)

The work required to open the existing cracks in each state is calculated for varying crack densities ( $\lambda$ ) and applied load ( $P$ ). The energy required to open  $N$  new cracks from a state containing  $N$  new cracks can be calculated from the energy required to open  $N$  and  $2N$  cracks respectively – Equation 123, based on the stresses transversal to the fiber directions on a given layer bundle ( $\sigma_2$ ) and the crack opening displacements obtained ( $u_2$ ) from the microscale models – Equation 124.

Figure 41 shows schematics how COD is calculated for an internal crack in a given laminate. This figure shows a normal cut view of a crack in the process of opening. The COD is then given by the distribution of this opening over the thickness of that layer. Also, it should be noted that the load  $P$  is used in this work in a general sense, as different kinds of metrics may be taken as an external load, i.e. applied external force, moment, deflection, strains, stresses, elongation, deformation energy or work.

Figure 41 – Schematics of the COD definition



Source: Developed by the author

$$W_{2N \rightarrow N} = W_{2N \rightarrow 0} - W_{N \rightarrow 0} = W(\lambda, P) - W\left(\frac{\lambda}{2}, P\right) = \Delta W(\lambda, P) \quad (123)$$

$$W(\lambda, P) = \int_{z_h}^{z_{h+1}} \sigma_2(\lambda, P) u_2(\lambda, P) dz \quad (124)$$

The crack multiplication occurs when the energy required to open  $N$  new cracks from a state already containing  $N$  cracks ( $W_{2N \rightarrow N}$ ) is equal the energy to open  $2N$  cracks from zero cracks minus  $N$  cracks from zero cracks or greater than the energetic resistance of the material against the opening of new cracks ( $W_C$ ). Mathematically, this occurs when Equation 125 is satisfied. The value of  $W_C$  can be obtained by using an inverse analysis, comparing results of the present methodology with results of well-behaved laminates under tensile monotonic tests, such as cross-ply or and  $\pm\theta$  lay-ups.

$$\Delta W(\lambda, P) \geq W_C \quad (125)$$

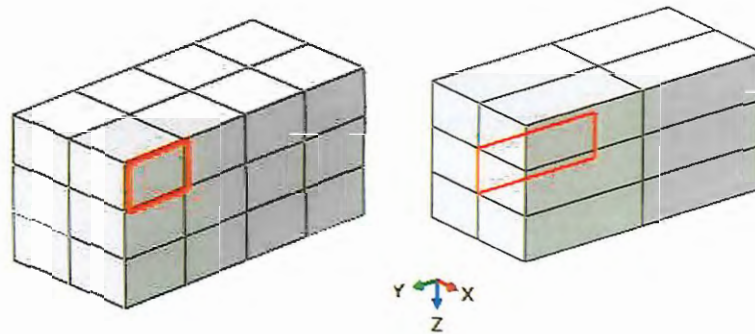
Equation 126 implies that the material behaves in such a way that intralaminar cracks grow mainly under Mode I, and even if there is sliding present – and thus work shearing stresses – the sliding is completely reversible. This happens as both the sliding parcel of the work, Equation 125, and the energy resistance to the creation of cracks through shear, which is analogous to growth under Mode II, were neglected. Singh and Talreja (2010) observed that this hypothesis is valid as because of two different behaviors. The first is that, for most polymer matrixes in use, the resistance for crack growth under Mode II is much greater than under Mode I (that is  $G_{1c} \ll G_{2c}$ ). The second is that for the cases where the shear stresses would be more relevant, in the same level than the normal stresses ( $\sigma_{12} \cong \sigma_2$ ), layers oriented less than  $45^\circ$  over the load direction, the failure is abrupt, and damage evolution can be neglected.

$$W(\lambda, P) = \int_{z_h}^{z_{h+1}} \sigma_{12}(\lambda, P) u_1(\lambda, P) dz \quad (126)$$

Even so, the present work proposes a numerical verification of this hypothesis, by simulating a crack propagation of the center crack of laminates with  $[0_n/\theta_m/0_n]$ ,  $[\theta_n/(90^\circ - \theta)_m/\theta_n]$  and  $[\pm\theta_m]$  lay-up under tensile and bending loads. For both laminates, the case of center cracks and edge cracks, until the crack grows the whole dimension of a coupon, were investigated. During the propagation, the energy release ratios  $G_1$  and  $G_2$ , as well as the crack opening displacement and crack sliding displacement of the cracks will be monitored, as the hypothesis may be numerically verified by comparing these values. Examples of the models used for this proposed analysis are shown in Figure 42. For the bending case, due to the progressive failure of different layers, failed layers are taken into account for the analysis of unbalancing of the laminate due to damage. Results of this analysis, considering the models with the center crack under bending loads, were obtained, and they are shown in Sections 5.3 and 5.4. Though these analysis are still not completed, it can be seen that before the unbalancing of the laminates, the sliding is practically null, and after the first layer failure, and introduction of strong unbalancing, the sliding parcel is still ten times lower than the opening, numerically verifying the supposition.



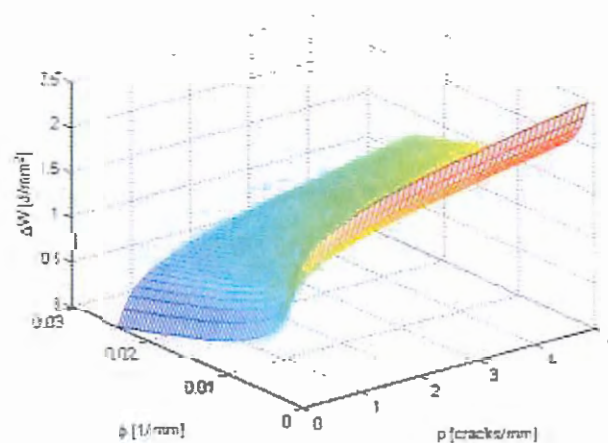
Figure 42 – Example of geometry of the proposed model for a  $[0^\circ/90^\circ/0^\circ]$  laminate to verify the hypothesis to neglect sliding. Center crack (left). Edge Crack (right).



Source: Developed by the author

Using Equation 125, a surface containing the energy released by the crack multiplication as function of crack density and external applied load ( $\Delta W$  vs.  $\lambda$  (or  $\rho$ ) vs.  $P$  (or  $\phi$ )) is constructed through several simulations of a given RVE. For each RVE and stress state profile obtained from the macroscale analysis, different models are constructed on Abaqus™ using automated Python scripts for a different number of cracks per layer of interest. Using the previous equations and for a linear step increase in this stress profile and the number of cracks the work for crack multiplication,  $\Delta W$  is calculated.

Figure 43 - Example of a  $\Delta W$  vs.  $\lambda$  (or  $\rho$ ) vs.  $P$  (or  $\phi$ ) surface



Source: Developed by the author

Finally, the curve found by the intersection of this surface and the plane of  $W_c$  height is the damage evolution behavior of a given layer for a given lay-up (crack density vs. load curve). An example of this surface is shown in Figure 43, where the crack density is being represented by  $\rho$  instead of  $\lambda$  and the load is represented by elongation  $\phi$  instead of  $P$ . As previously discussed, the methodology let several different metrics to be employed as external loads.

## 5.2 Unbalancing and opening vs. sliding studies

To study the influence of the CSD damage mode under bending loads four glass-epoxy laminates with material properties found in Table 16 are considered, an unbalanced  $[0^\circ/+0_3/-0]_s$  and balanced  $[0/\pm\theta_2]_s$  for  $\theta=45^\circ, 60^\circ, 90^\circ$ . The elastic modulus and Poisson constant were taken as close to the typical glass-epoxy values. The energy resistance to crack multiplication were taken from Singh and Talreja (2010), and the ultimate strength, strain and elastic modulus degradation due to layer progressive failure were taken from Belingardi and Cavatorta (2006).

Table 16 - Material properties used for the CSD damage mode evaluation tests

$E_1$ [GPa]	$E_2$ [GPa]	$G_{12}$ [GPa]	$\nu_{12}$	$W_{IC}$ [J/m <sup>2</sup> ]	$X_T$ [MPa]	$\varepsilon$ at failure [%]
45.0	12.0	4.80	0.280	232 <sup>(1)</sup>	509 <sup>(2)</sup>	1.7 <sup>(2)</sup>

Source: <sup>(1)</sup> Singh and Talreja (2010); <sup>(2)</sup> Belingardi and Cavatorta (2006)

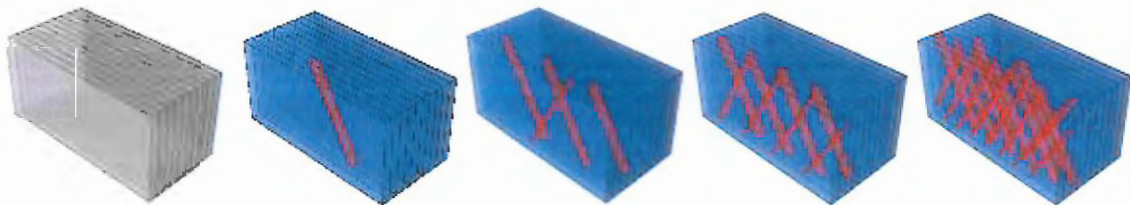
The damage evolution was evaluated for every layer per normal using the proposed in Chapter 3. The results for the COD vs. crack density curves are used to place the number and position of the cracks in the model.

Then, the damaged RVEs related to the different lay-ups was modelled and analyzed by the finite element method, using a non-uniform displacement distribution over the thickness to simulate pure bending calculated via GUF as shown in Chapter 4. This simulation was carried out in steps of strain load until any layer presented a level of stress or strain

corresponding to failure by the maximum strength or maximum strain failure criteria respectively. The models were simulated for a range of imposed axial strain loads between 0.1% and 3% with a 0.1% step. When this threshold occurs, the cracks of the layer are erased from the model, and its elastic properties are degenerated to a value found experimentally by Belingardi and Cavatorta (2006). During the simulation, the CSD of the first nucleated crack for the first and second damaged layers and average shearing stress in this crack surface are recorded. This data is used as a metric to study the influence of CSD damage mode in the damage evolution of the composite by comparing the results obtained from unbalanced and balanced lay-up, due to the simple progressive failure model, where the balanced laminate tends to the behavior of an unbalanced.

As a non-uniform distribution of load over the thickness is used, even though the laminates studied are symmetric, the load is not; as such, the whole laminate is modelled in the RVE. This way the RVE may be modelled with a different number of cracks per layer. The load in the simulation is increased quasi-statically, increasing the crack density of each layer systematically, according to the aforementioned damage evolution. This process is exemplified for the  $[0^\circ/\pm 60^\circ_2]_S$  laminate in Figure 44.

Figure 44 - Crack evolution under bending for the proposed analyses of a  $[0^\circ/\pm 60^\circ_2]_S$  laminate



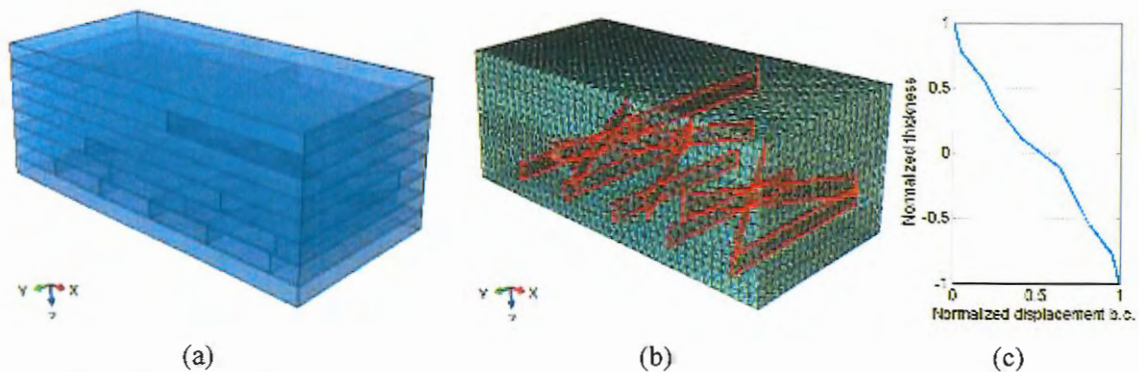
Source: Developed by the author

An example of the RVEs created is shown in Figure 45a and b. In this case, the evolution for the fourth layer of a  $[0^\circ/\pm 60^\circ_2]_S$  laminate is being calculated. The symmetry of the laminate and load are used to reduce computational time, as such only half of the laminate is modelled.

Figure 45c shows an example of the averaged displacement of a crack obtained by the implemented methodology on Abaqus® for both the balanced laminate  $[0^\circ/\pm 60^\circ_2]_S$  and unbalanced laminate  $[0^\circ/+60^\circ_3/-60^\circ]_S$ . It shows the premises that unbalancing the laminate

creates sliding displacements within the cracks, as well as that the methodology obtained the typical shape for crack opening for both crack modes.

Figure 45 - Example of RVE used for the Mode II influence verification on a  $[0^\circ/90^\circ/\pm 60^\circ]_s$  lay-up. (a) Geometrical model and cracks. (b) Mesh. (c) Example of a normalized displacement distribution over the thickness



Source: Developed by the author

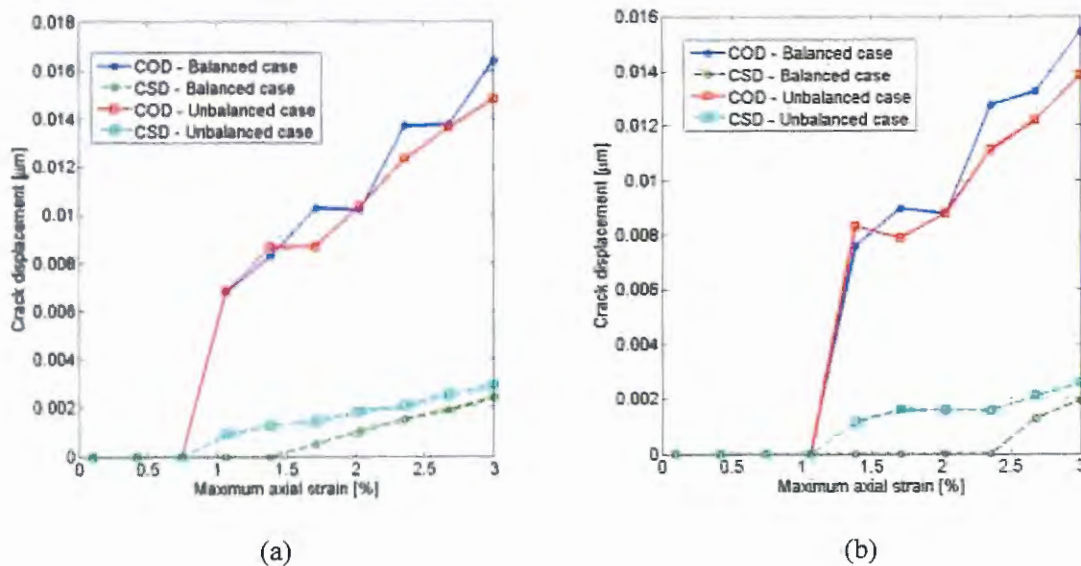
Figure 46a and Figure 46b shows the evolving CSD and the shear stress in the neighborhood of the crack for the first nucleated crack of the first and second failing layers found by both the balanced and unbalanced laminates for  $60^\circ$ . For the balanced case, as expected, the first layers to fail were the ninth, followed by the eighth layers. However, for the unbalanced case, the ninth layer was the first to fail, followed by the sixth layer, the first layer with the negative aligned angle. This fact can be explained by the increased maximum tensile stresses found in the sixth layer due to its boundary conditions. The unbalancing of the lay-up increases the shear stresses and influence of the top and bottom layers over a sudden negative angle, which, by nature of the boundary conditions of the laminate increases the working normal stresses this layer has to support.

It can be seen for the unbalanced laminate that the cracks start sliding as soon as the first crack is nucleated, around 0.613% remote maximum strain for the ninth layer, Figure 47a, and around 1.023% remote maximum strain for the eighth layer, Figure 47b. However, for the studied case, it is about one order of magnitude lower than the crack opening. For the balanced case, the crack start sliding only when the first layer fails, unbalancing the laminate.

Moreover, as the sliding begins, it quickly increases to the levels observed in the unbalanced case. Comparing Figure 46 and Figure 47, it can be observed that the progressive failure of the layers, found in the points where the behavior of the shear stress changes (increases or remain stable), had a greater impact in the COD of the balanced case than the unbalanced one. For the balanced case, during the steps that occurred layer failure, the COD remained stable, unlike for the unbalanced case in which it grew practically for the whole simulation.

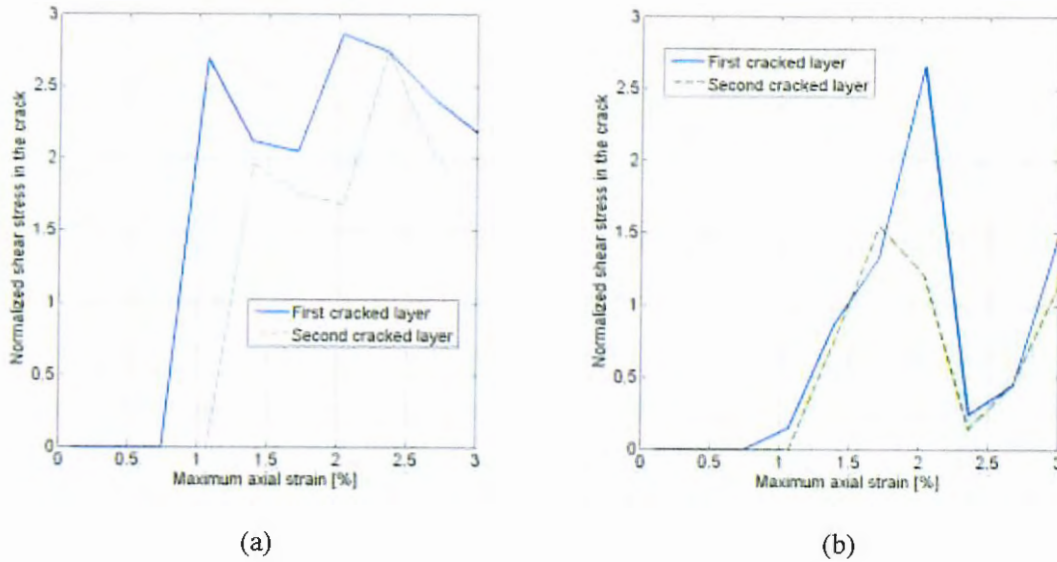
Finally, from the results shown, it can be seen that the analysis were not completely successful, especially in the shear stress, in particular due to the step range in the applied strain used. A linear step over the applied strain evolution was chosen, when a more correctly way to evolve the load is to calculate the strain step so that in each step an equal amount of damage is considered. For that, one solution is to use an arc length algorithm with the damage evolution curves, so that a given damage step, that will be set equal to the arc length radius parameter is covered in each step.

Figure 46 - Evolution of the analysis for crack displacements for 60°. a. First cracked and failed layer (ninth layer); b. Second cracked and failed layer (eighth layer for balanced, sixth layer for unbalanced)



Source: Developed by the author

Figure 47 - Evolution of the analysis for shear stress near the cracks for 60°. a. First cracked and failed layer (ninth layer); b. Second cracked and failed layer (eighth layer for balanced, sixth layer for unbalanced)



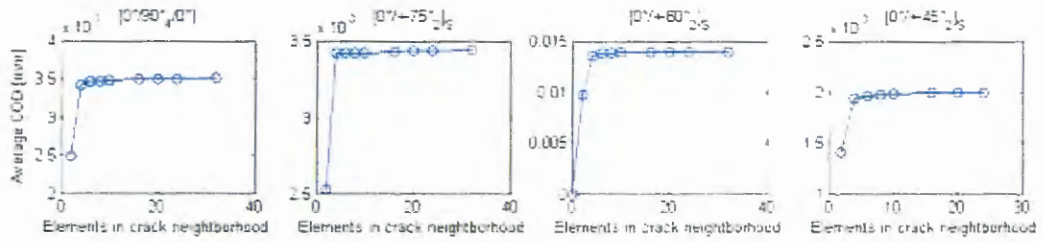
Source: Developed by the author

It is important to highlight that the shear stress evolution shown in Figure 48 and Figure 49 is not precisely calculated due, in the time of the simulations, the algorithm to automatically calculate the shear stresses was not yet implemented, and as such, they were made by manually picking some nodes around the cracks and using this data to calculate the average.

### 5.3 Geometric Convergence Tests, Adaptations and Solutions

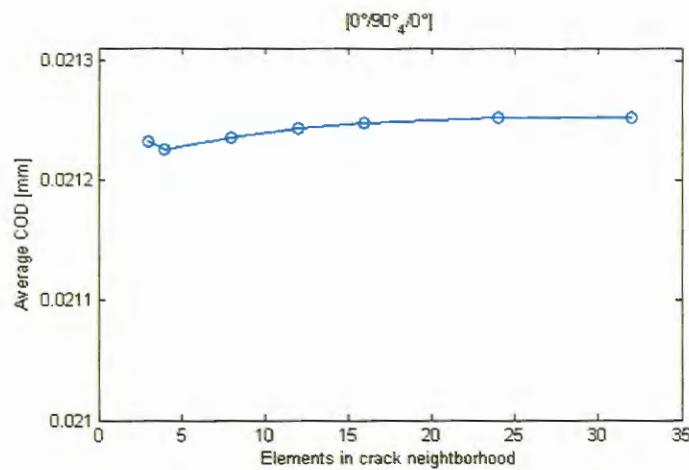
The finite element model used to simulate the intralaminar model was tested for convergence relating to both mesh density and RVE dimensions. Figure 48 and Figure 49 show the convergence tests for mesh density for respectively tensile and bending load cases for different types of laminates. Figure 50 shows the convergence tests for different laminates for the RVE dimensions. At some angles for the cracked layers orientation, some discrepancies were found.

Figure 48 - Mesh densities convergence tests for tensile loads for various laminates



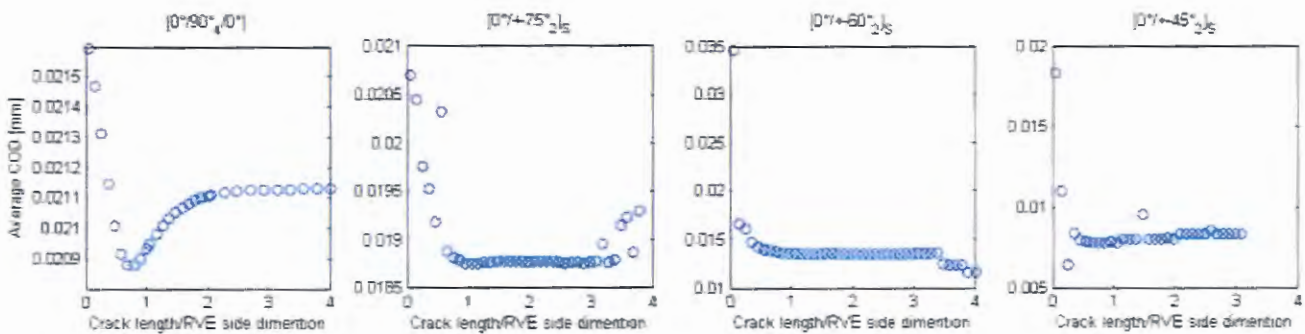
Source: Developed by the author

Figure 49 - Mesh densities convergence tests for bending loads for a [0°/90°<sub>4</sub>/0°] laminate



Source: Developed by the author

Figure 50 - RVE dimension convergence tests for bending loads for various laminates

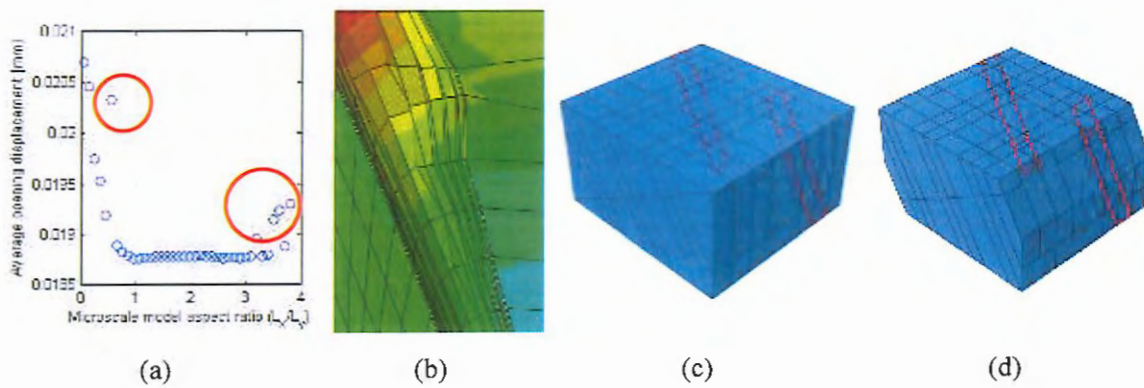


Source: Developed by the author

These discrepancies, highlighted at Figure 51a, were obtained because, at first, the microscale was modelled using simple parallelepipeds for the calculation energy released by

the multiplication of cracks at different crack density values. In particular, for damaged layers in angled direction where the cracks are angled in relation to the faces of the RVE, the cases in which the crack ends near or over the corner of the RVE were problematic as shown in Figure 51b and c. This was due to the incorrect opening of the cracks near the edges due to the boundary conditions applied to the microscale model. To solve this problem, a hexagonal prism microscale model was used for non 90° layers as shown in Figure 51d. In the angled cut-out faces, stresses rotated using the classic rotation theory for in-plane stresses are applied, as such each face works using the rotated Cauchy stresses. The out-of-plane stresses remain the same due to no rotation in the theta-axis occurring.

Figure 51 – (a) Problematic points found in the  $[0^\circ/\pm 75^\circ_2]_s$  laminate; (b) Example of crack behavior near the corner in the problematic model; (c) Example of crack problematic corner in the parallelepiped model; (d) Hexagonal prism model solution.

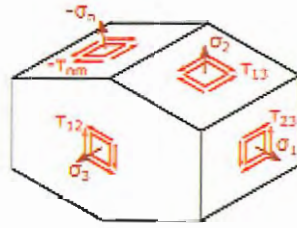


Source: Developed by the author

Figure 52 shows these boundary conditions, which were developed and implemented by the present author using the basic premise and definition of Cauchy stresses as a base. These boundary conditions may be understood as the stresses that are applied over a single point in the macroscale that is being modeled in the microscale as a thickness line that represents the laminate, but expanded to its immediate vicinity that receives stresses from the neighborhood. These stresses are the stresses distribution over the thickness obtained from the macroscale analysis, separated per face and rotated using the appropriate plan.



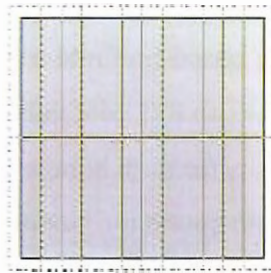
Figure 52 - Boundary conditions for the hexagonal prism model



Source: Developed by the author

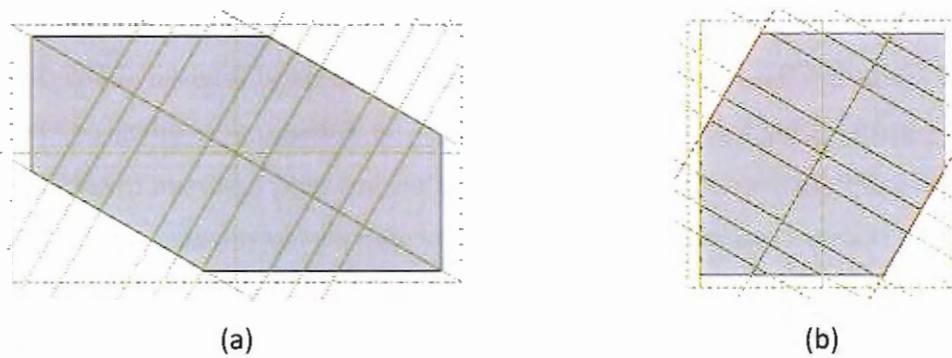
Figure 53, Figure 54 and Figure 55 shows different geometries that may be created.

Figure 53 – Example of RVE geometry used for a cross-ply lay-up with only 90° damaged layers



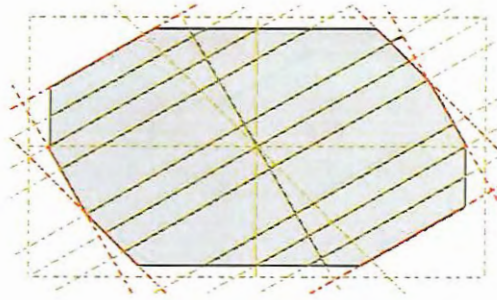
Source: Developed by the author

Figure 54 - Example of RVE geometry used for an angled-ply lay-up with: (a) only 60° damaged layers; (b) only -30° damaged layers



Source: Developed by the author

Figure 55 - Example of RVE geometry used for a generic lay-up with damaged layers oriented at  $-45^\circ$ ,  $30^\circ$ ,  $60^\circ$  and  $90^\circ$



Source: Developed by the author

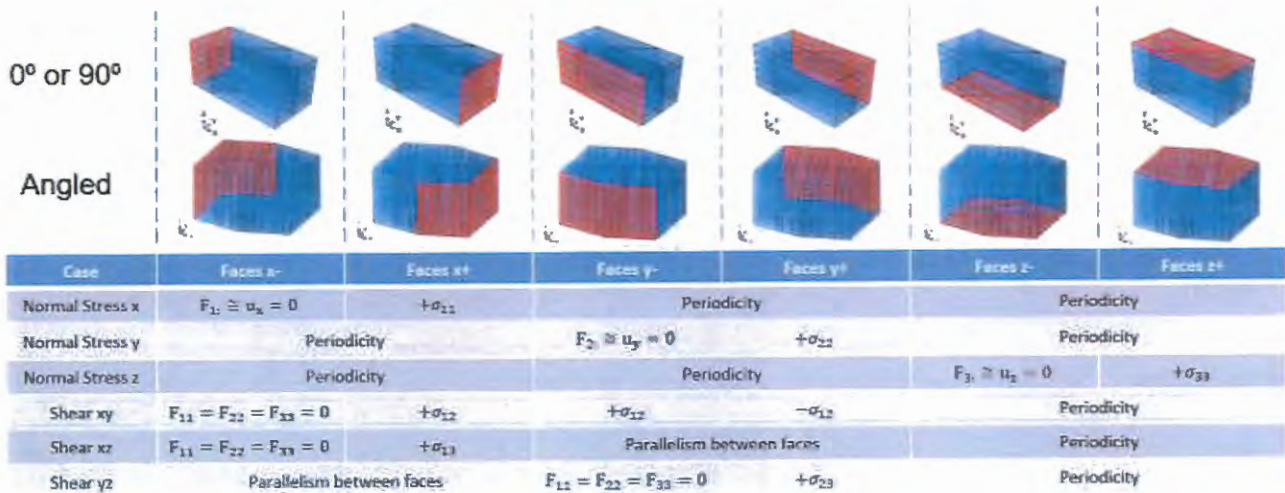
#### 5.4 Homogenization model

The degraded elastic properties as function of the crack density curves were obtained using a homogenization methodology based on finite element analysis and damaged RVEs. First, an automated Python code creates an RVE containing a given, pre-calculated amount of damage, characterized by a crack density for each bundle of layers with the same orientation. Figure 56 summarizes the load cases and boundary conditions used. The proposed model uses the six simplest boundary conditions that create linear independent stress states in the RVE: uniaxial traction in each of the three principal directions and shear in each of the three principal planes.

In homogenization process of a heterogeneous solid such as a composite ply, the RVE size must be large enough to contain sufficiently many fibers to provide average properties. With fibers of typically 0.01 mm in diameter, and a ply thickness of typically 0.125 mm, the RVE extending across a ply thickness may or may not be enough, depending on the fiber volume fraction and fiber distribution irregularity, but it is implicitly assumed to suffice in the classical laminate theory. However, when cracks appear within a ply, the local stress gradients increase sharply, leading to a breakdown of the homogenized ply properties. Away from the cracks, nevertheless, the properties hold. In obtaining the overall (average) composite properties with multiple cracks, the RVE size must be large enough to contain a representation of the cracks. To satisfy this requirement the RVE must be extended in the laminate length direction while it is limited in the thickness direction by the laminate thickness.

For each load case, the volumetric average of the engineering stress state  $\bar{\sigma}_{ij}$  and the strain  $\bar{\epsilon}_{ij}$  fields over the RVE are obtained, following Equation 127 and 128. In these equations,  $\bar{\sigma}_{ij}$  and  $\bar{\epsilon}_{ij}$  are the volumetric averages of the stresses and strains over the single n-th tridimensional element in the RVE;  $n_{gp}$  is the number of integration points used on the element;  $V^n$  is the volume of the n-th element; and  $\sigma_{ij}^{nk}$  and  $\epsilon_{ij}^{nk}$  are the ij component of stress and/or strain on the k-th integration point in the n-th element. Using these average stresses and strains, an orthotropic constitutive equation is written, as in Equation 129. The volumetric average constitutive relation is written with the elastic coefficients as variables. Thus, each load case generates six equations. Combining the six load cases, thirty-six equations are found. The final 36 equations per 13 variables linear system is solved using a least square method per layer. In other words, the procedure is performed layer-by-layer. This is made as the different membrane properties is what mathematically creates the physical behavior of traction-bending coupling in the case of asymmetric lay-ups (Reddy and Ochoa, 1996).

Figure 56 - Load Cases and Boundary Conditions for the homogenization procedure



Source: Developed by the author

$$\bar{\sigma}_{ij} = \sum_n^{n_{elem}} \frac{1}{V^n} \frac{\sum_k^{n_{gp}} \sigma_{ij}^{(nk)}}{n_{gp}} \tag{127}$$

$$\bar{\varepsilon}_{ij} = \sum_n^{n_{elem}} \frac{1}{V^{(n)}} \frac{\sum_k^{n_{gp}} \varepsilon_{ij}^{(nk)}}{n_{gp}} \quad (128)$$

$$\begin{Bmatrix} \sigma_{xx} \\ \sigma_{yy} \\ \sigma_{xy} \\ \sigma_{xz} \\ \sigma_{yz} \\ \sigma_{zz} \end{Bmatrix} = \begin{bmatrix} \bar{C}_{11} & \bar{C}_{12} & \bar{C}_{16} & 0 & 0 & \bar{C}_{13} \\ \bar{C}_{12} & \bar{C}_{22} & \bar{C}_{26} & 0 & 0 & \bar{C}_{23} \\ \bar{C}_{16} & \bar{C}_{26} & \bar{C}_{66} & 0 & 0 & \bar{C}_{36} \\ 0 & 0 & 0 & \bar{C}_{55} & \bar{C}_{45} & 0 \\ 0 & 0 & 0 & \bar{C}_{45} & \bar{C}_{44} & 0 \\ \bar{C}_{13} & \bar{C}_{23} & \bar{C}_{36} & 0 & 0 & \bar{C}_{33} \end{bmatrix} \begin{Bmatrix} \varepsilon_{xx} \\ \varepsilon_{yy} \\ \gamma_{xy} \\ \gamma_{xz} \\ \gamma_{yz} \\ \gamma_{zz} \end{Bmatrix} \quad (129)$$

Due to problems already explained in the previous Section 5.2, for laminates that feature damage in layers with an orientation different from 0 or 90°, a hexagonal prism is used as an RVE instead of a parallelepiped. As such, the common way for the imposition of stresses in the faces, as well as the classical implementation of periodic boundary conditions and parallelism between faces could not be implemented. The problem was solved by adapting the boundary conditions used in the work of Danielsson et al. 2002. In this work, the first Piola-Kirchhoff S stress tensor – Equations 130 and 131 – and the deformation tensor F – from which the logarithmic strains E are calculated as in Equation 132 – are used to apply the load cases directly as stresses using.

$$S = 2 \frac{V}{V_0} \sigma F^{-T} \quad (130)$$

$$F = RU \quad (131)$$

$$E = \ln(U) \quad (132)$$

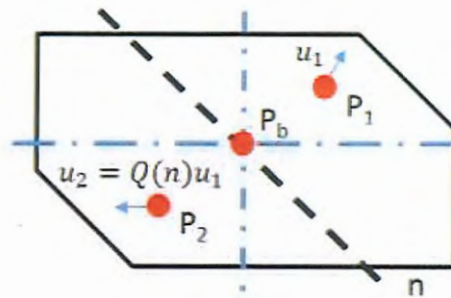
The periodicity and parallelism conditions are applied for any given polyhedron with parallel faces using Equation 133 and 134 (see Figure 56). In these equations,  $P_b$  is the barycenter of a given face,  $P_1$  and  $P_2$  represent every pair of points over the face that are reflection of each other over the normal axis n that passes over  $P_b$ , u are displacements of a

given point,  $x$  are its coordinates and  $Q(n)$  is the reflection operator tensor over  $n$ . Figure 57 represents schematically these relationships.

$$u(P_1) + Q(n)u(P_2) = 2(F - I)x(P_b) \tag{133}$$

$$(F - I)x(P_b) = u(P_b) \tag{134}$$

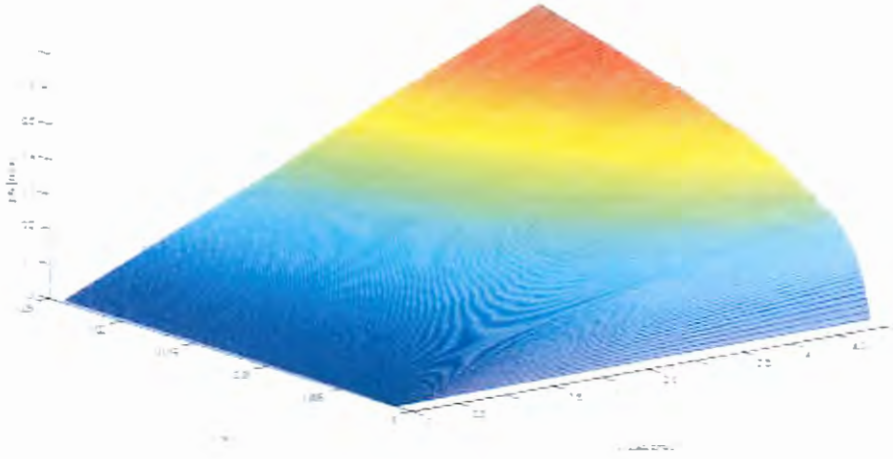
Figure 57 - Representation of the periodicity boundary conditions



Source: Developed by the author

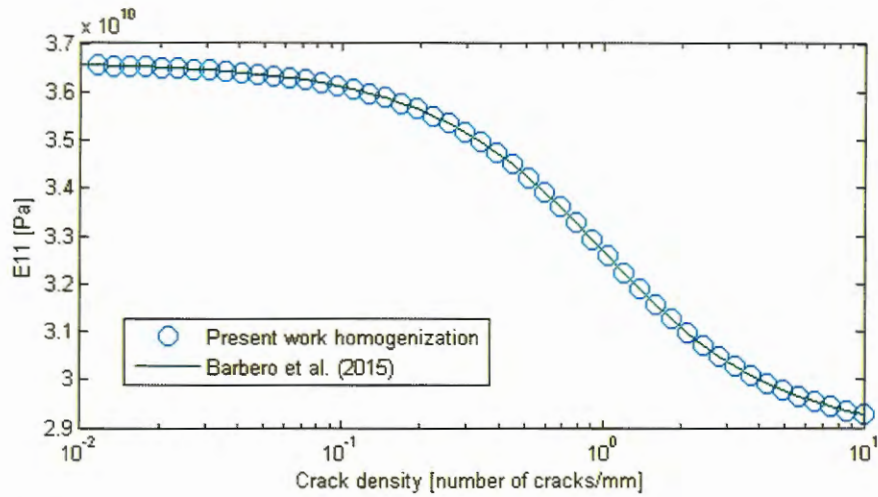
The intralaminar damage evolution and homogenization were validated using analytical solutions developed by Barbero et al. (2015) and Barbero et al. (2016) for cross-ply laminates under pure tensile and pure bending loads respectively. After the validation for homogenization, found in Figure 59 and Figure 60, the analytical solutions were used to calculate the values of  $W_c$  considering the energy surface found in Figure 58, which gave a value of  $W_{IC} = 638.72 \text{ J/mm}^2$ .

Figure 58 – Energy required for crack multiplication surface for a  $[0^{\circ}_2/90^{\circ}_4]_S$  laminate



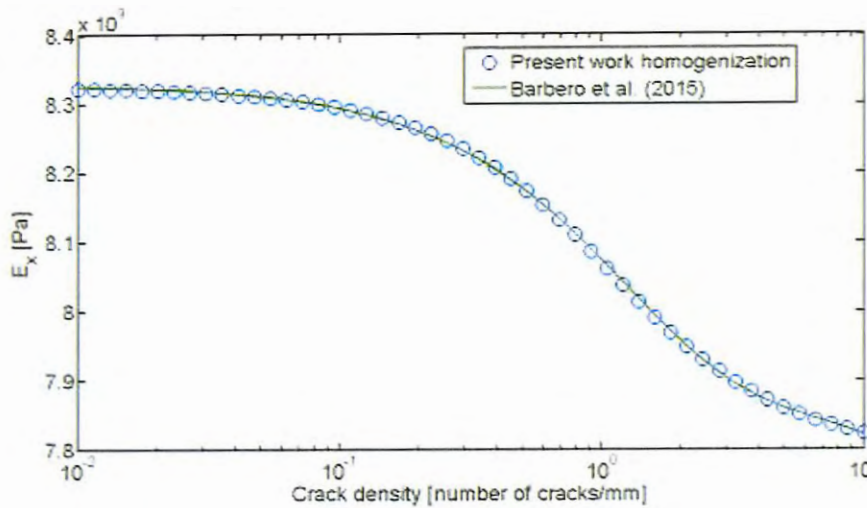
Source: Developed by the author

Figure 59 - Results for a laminate  $[0^{\circ}_2/90^{\circ}_4]_S$  property degradation under tensile loads



Source: Developed by the author

Figure 60 - Results for a laminate  $[0^{\circ}_2/90^{\circ}_4]_S$  property degradation under bending loads



Source: Developed by the author

### 5.5 Results

Two material types were analyzed using the implemented Python scripts. A glass-epoxy composite with a known value of  $W_{IC}$  with properties found in the literature (Singh and Talreja, 2010) as shown in Table 17. And, a carbon-epoxy composite characterized by the GEA (Aeronautic Structures Group of Sao Carlos School of Engineering/USP), similar to the material studied by Tita et al. (2008), with properties shown in Table 17.

Table 17 - Properties fo the analyzed material layers

	$E_1$	$E_2, E_3$	$\nu_{12}, \nu_{13}$	$\nu_{23}$	$G_{12}, G_{13}$	$G_{23}$	$W_{IC}$	$t$
	[GPa]	[GPa]	[ ]	[ ]	[GPa]	[GPa]	[J/m <sup>2</sup> ]	[mm]
<b>Glass/Epoxy</b>	46	12	0.3	0.4	5	4.3	232	0.5
<b>Carbon/Epoxy</b>	127	10.3	0.340	0.306	5.40	3.05	-	0.18

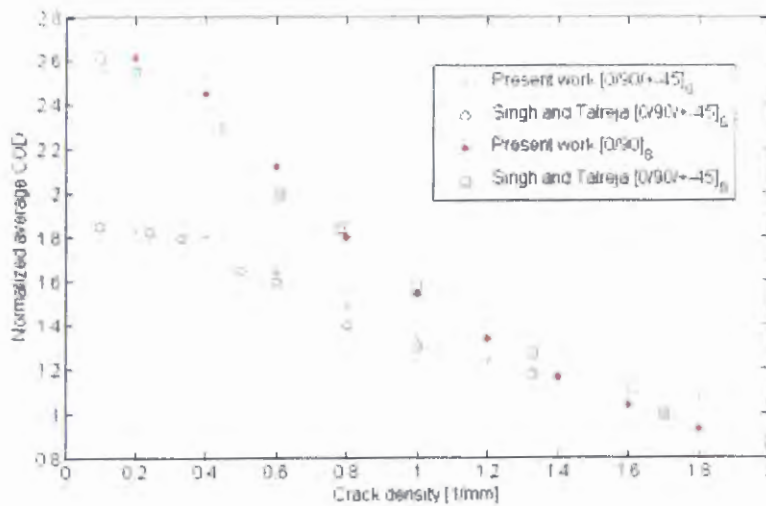
Source: Developed by the author

Figure 61 shows the normalized COD for the  $90^{\circ}$  layers evolution found for  $[0^{\circ}/90^{\circ}]_S$  and  $[0^{\circ}/90^{\circ}/\pm 45^{\circ}]_S$  laminates, using the glass-epoxy material, as well as the damage evolution

curves calculated. This shows the successfully implemented methodology discussed in Chapter 3, as the results found in the literature could be reproduced. Figure 62 shows the corresponding damage evolution curves. However, the comparison to the literature cannot be made as the data is not available.

Figure 62 shows the normalized COD for the  $90^\circ$  layers evolution found by a  $[90^\circ]_S$  laminate using the carbon-epoxy material. Using experimental data available for tensile tests of the same laminate. These results were used in conjunction to the Python algorithms to estimate the  $W_{IC}$  of the material. Results for  $W_{IC}$  varied, depending on the used experimental data set, from 581 to 643 J/m<sup>2</sup>.

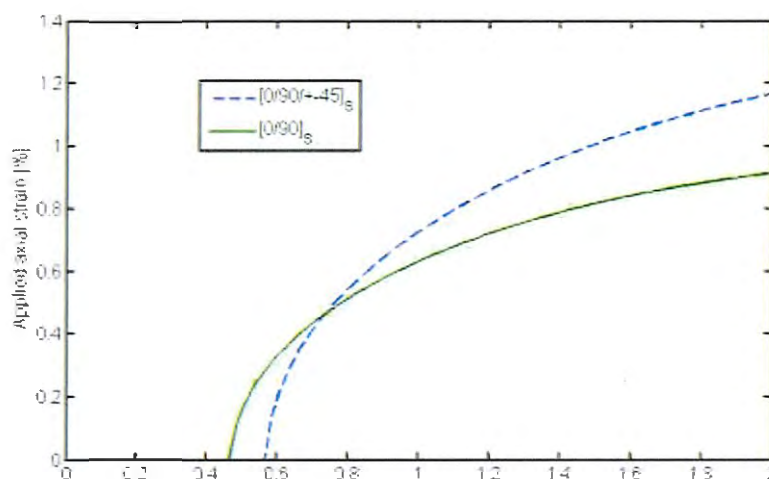
Figure 61 - Normalized average COD for a  $[0^\circ/90^\circ]_S$  glass-epoxy laminate, present work vs. literature



Source: Developed by the author



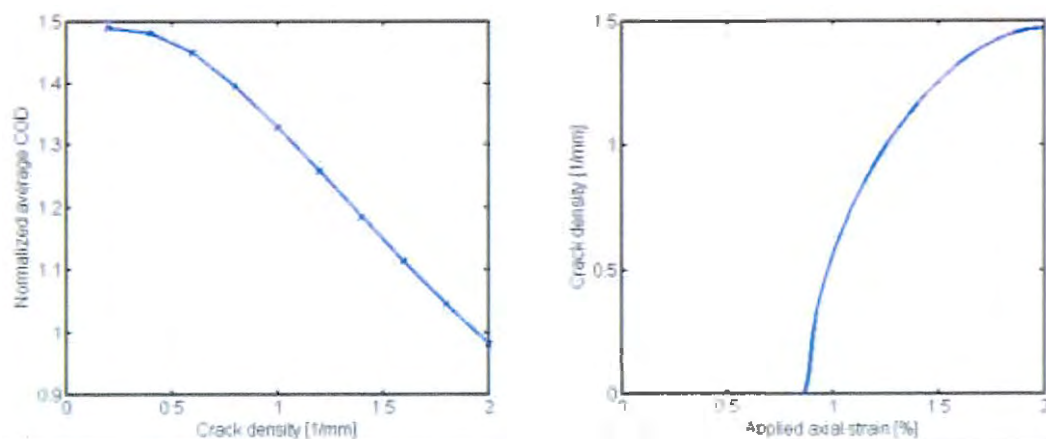
Figure 62 - Damage evolution for  $[0^\circ/90^\circ]_S$  and  $[0^\circ/90^\circ/\pm 45^\circ]_S$  glass-epoxy laminate



Source: Developed by the author

However, the  $W_{IC}$  as not accurate as the experimental tests, which showed coupons that failed before damage nucleation. This probably occurred due to problems with the experimental data, as the coupons suffered a fast failure near the clamps of the testing machine, suggesting that the thickness was not enough to obtain the real stress-strain curves of the material (Tita, 2003). In fact, experiments can be made to generate more reliable data to test the  $W_{IC}$  optimization/calculation algorithm.

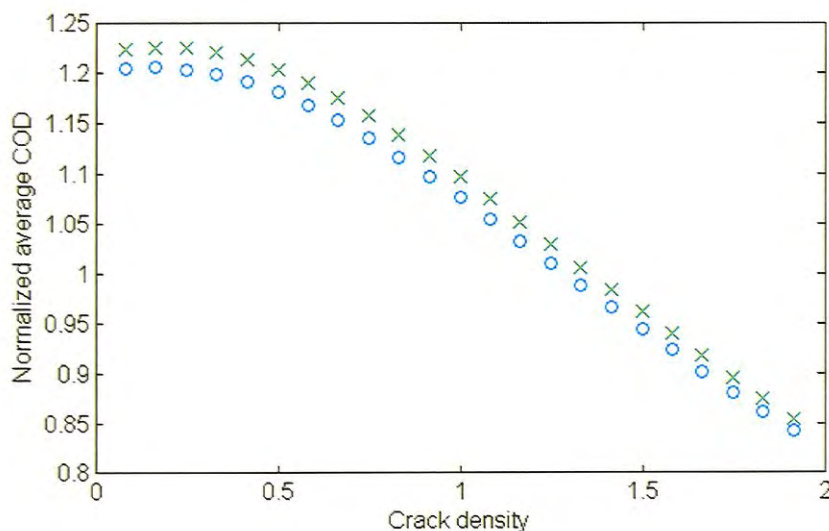
Figure 63 - COD vs. crack density and damage evolution for a  $[90]_S$  carbon-epoxy laminate



Source: Developed by the author

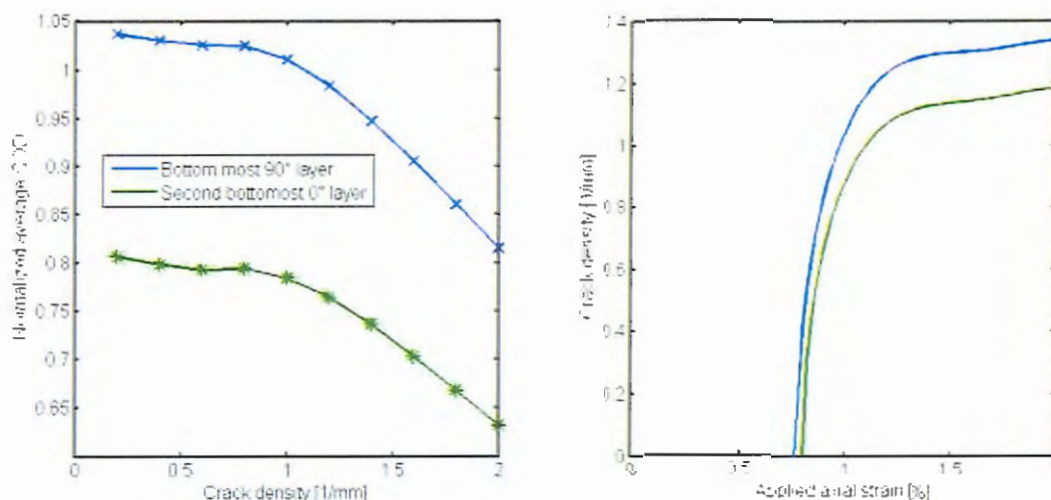
Figure 64 and Figure 65 show the crack density vs. normalized averaged COD for the 90° layers in  $[0^\circ/90^\circ/0^\circ/90^\circ/0^\circ]_S$  laminate, manufactured by using carbon-epoxy material from Ribeiro et al. (2012). Figure 64 shows the curves for the top most and middle 90° layers under tensile loads, which were calculated using uniform displacements in the RVEs. Figure 65 shows the curves for the same layers under pure bending loads, which were calculated via non-uniform displacements. It can be seen that under the tensile loads, the behavior for the same oriented layers is practically the same, as the theory predicts. However, for the bending simulations, as closer layer is to the bottom of the laminate as greater the damage absorbed by that layer. The similar shape of the curves of the two layers for the bending load requires third order deformation theory, which makes it so that the distributed displacement over both layers is similar.

Figure 64 - COD vs. crack density for the two bottommost 90° layers in  $[0^\circ/90^\circ/0^\circ/90^\circ/0^\circ]_S$  lay-up under pure bending load.



Source: Developed by the author

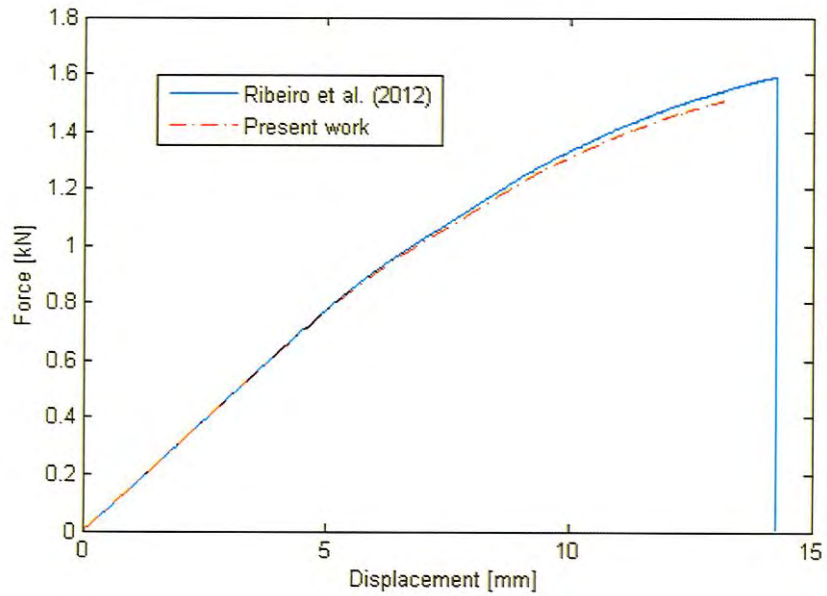
Figure 65 –COD vs. crack density and damage evolution for the two bottommost 90° layers in a [0°/90°/0°/90°/0°]<sub>S</sub> lay-up under pure bending load



Source: Developed by the author

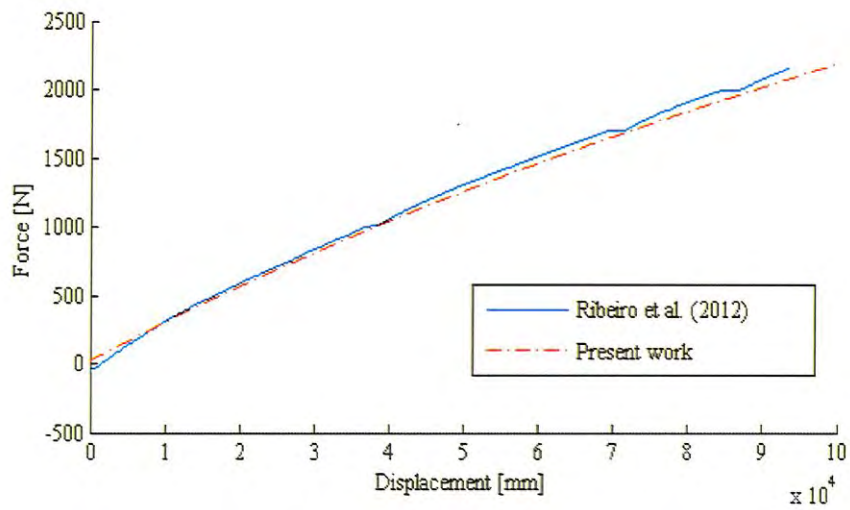
The model was applied to two different laminates: the first with [90°<sub>10</sub>] lay-up and the second with [±67.5°<sub>10</sub>]<sub>S</sub> lay-up. The values of  $W_c = 638.72 \text{ J/mm}^2$  were obtained using Barbero et al. (2015) and Barbero et al. (2016) analytical solution for the [0°<sub>2</sub>/90°<sub>4</sub>]<sub>S</sub> laminate. This specific lay-up was chosen for both being solvable by the aforementioned solution, and due to recommendations made by Singh et al. (2010). The experimental data for the [90°<sub>10</sub>] and [±67.5°<sub>10</sub>]<sub>S</sub> laminate under tension loading were obtained from the works of Ribeiro et al. (2012). For each laminate the damage evolution curve (crack density vs. load), property degradation ( $E_{11}$  vs. crack density) and experimental validation (force vs. displacement under a tensile test) calculated using the proposed methodology are shown in Figure 66 and Figure 67. It is important to highlight that for [±67.5°<sub>10</sub>]<sub>S</sub> laminate under tension, the damage is promoted by a combination of normal and shear stresses.

Figure 66 – Comparison between present methodology and experimental results for a  $[90^{\circ}_{10}]$  laminate under tension



Source: Developed by the author

Figure 67 - Comparison between present methodology and experimental results for a  $[\pm 67.5^{\circ}_{10}]_s$  laminate under tension



Source: Developed by the author

## 6 FINAL DISCUSSIONS, CONCLUSIONS AND FUTURE DEVELOPMENTS

---

Regarding the methodology for the calculation of intralaminar damage in composite materials based on multiscale analysis, it is possible to conclude that the objective of creating a computational efficient physically consistent procedure was accomplished. Both the macroscale and microscale analysis implemented in the methodology followed modern and **new approaches** for the simulation of laminated materials. In particular, from the new approaches developed, it is worth noting the **use of the Generalized Unified Theories** applied into the Finite Element Method for shell theories for the calculation of external loads, the **intralaminar damage evolution modelled through matrix crack multiplication**, and homogenization theories adapted to **non-uniform prismatic Representative Volume Elements**.

Concerning the macroscale analysis, the implementation and adaptation of the Generalized Unified Formulations (GUF) into stand-alone python codes was deemed a success. The final scripts showed both a good performance and good results that were validated by different criteria, such as comparison with full 3D models and analytical solutions. Moreover, the algorithm for generation of GUF's kernels inside the codes instead of needing them as inputs. The optimization of deformation theories in relation to stresses and strains distributions through the thickness was also successful. In particular, through this algorithm, the author was able to conclude that the advantages of mixed formulations do not offer enough gains for its justifications, and the fact that cubic deformation Layer-Wise theories are enough for the studied load cases. However, considering other laminates, this approach can provide more accuracy results, mainly for investigation about delamination

Regarding the microscale analysis, both the intralaminar damage evolution analysis and the homogenization analysis were deemed satisfactory as they were validated within experimental data and analytical solutions, which were found in the literature. In particular, the implementation of non-uniform RVEs, prismatic polyhedrons that change the number of faces depending of the lay-up of the composite laminate, proved to be successfully. And, in fact, this is a new approach not yet found in the literature. The results for the procedure

showed consistence with experimental data found in the literature, further validating the developed multiscale methodology.

Based on the conclusions, it is possible to highlight some perspectives for future works by:

- Expand the methodology to include more complex loads cases, like quasi-static indentations tests, dynamic cases such as low-energy impact or fatigue cyclic loads;
- Expand the methodology to combined and/or multiaxial loads in a way that leaves the microscale analysis independent of the external load types. This may be accomplished by changing the external load metric from strains found in the material points to elastic deformation energy accumulated on the material points and energy release through the opening and sliding of cracks due to its creation or multiplication.
- Study the model by using Energy metrics instead strains in the surface defined by the crack multiplication as function of crack density and external applied load ( $\Delta W$  vs.  $\lambda$  (or  $\rho$ ) vs.  $P$  (or  $\phi$ )).

## 7 PUBLICATIONS

---

This chapter present a list of publications by the author during the development of the Ph.D. work. Papers published in scientific journals are directly or indirectly related to the Thesis manuscript:

Sartorato, Murilo ; De Medeiros, Ricardo ; Vandepitte, Dirk ; Tita, Volnei . Computational model for supporting SHM systems design: Damage identification via numerical analyses. *Mechanical Systems and Signal Processing*, v. 84, p. 445-461, 2017.

De Medeiros, Ricardo ; Sartorato, Murilo ; Vandepitte, Dirk ; Tita, Volnei . A comparative assessment of different frequency based damage detection in unidirectional composite plates using MFC sensors. *Journal of Sound and Vibration*, v. 383, p. 171-190, 2016.

Sartorato, Murilo ; De Medeiros, Ricardo ; Tita, Volnei . A finite element formulation for smart piezoelectric composite shells: Mathematical formulation, computational analysis and experimental evaluation. *Composite Structures*, v. 127, p. 185-198, 2015.

Full papers published in scientific conferences annals:

Santos, M. V. M. ; Sartorato, M. ; Ribeiro, M. L. . Layerwise Numerical Solution For Deep Beams. In: *II Simpósio De Pós-Graduação Em Engenharia Mecânica, 2017, São Carlos. Anais do II SiPGEM, 2017.*

Sartorato, M. ; Talreja, R. ; Tita, V. . Prediction of intralaminar damage in composite materials under tensile loadings based on multiscale models and continuum fracture mechanics. In: *I Simpósio do Programa de Pós-Graduação em Engenharia Mecânica da EESC-USP, 2016, São Carlos. Anais do I SiPGEM, 2016.*

Sartorato, M. ; Medeiros, R. ; Tita, V. ; Talreja, R. . A multiscale based continuum model: influence of crack sliding mode on composite materials damage evolution. In: *International Symposium on Solid Mechanics, 2015, Belo Horizonte. Proceedings of MecSol 2015, 2015.*

MEDEIROS, R. ; SARTORATO, M. ; TITA, S. P. S. ; VANDEPITTE, D. ; RIBEIRO, M.L. ; TITA, V. Residual strength criterion based on damage metric and flexural after impact (FAI) test for

composite materials. In: Congress of Mechanical Engineering, 2015, Rio de Janeiro. Proceedings of COBEM 2015, 2015.

Sartorato, M. ; Tita, V. A non-linear finite element for curved active composites with embedded piezoelectric layers. In: II Brazilian Conference on Composite Materials, 2014, São José dos Campos. Proceedings of II BCCM, 2014.

Medeiros, R. ; Sartorato, M. ; Vandepitte, D. ; Tita, V. Experimental damage identification for unidirectional carbon reinforced plates. In: II Brazilian Conference on Composite Materials, 2014, São José dos Campos. Proceedings of II BCCM, 2014.

Medeiros, R. ; Sartorato, M. ; Vandepitte, D ; Tita, V. . Shm of composite plates: Vibration based method by using PZT sensors. In: International Conference on Noise and Vibration Engineering 2014, 2014, Leuven. Proceedings of ISMA 2014, 2014.

Medeiros, R. ; Ribeiro, M.L. ; Sartorato, M. ; Marinucci, G. ; Tita, V. . Computational simulation using PZT as sensor elements for damage detection on impacted composite cylinders. In: International Symposium on Solid Mechanics, 2013, Porto Alegre. Proceedings of MecSol 2013, 2013.

Sartorato, M. ; Medeiros, R. ; Marques, F. D. ; Tita, V. ; Vandepitte, D. . Vibration-based damage identification applied for composite plate: numerical analyses. In: XXII International Congress of Mechanical Engineering, 2013, Ribeirão Preto. Proceedings of COBEM 2013, 2013.

Sartorato, M. ; Tita, V. . Influence of the transversal shear effects on structural analysis of aircraft tails. In: XXII International Congress of Mechanical Engineering, 2013, Ribeirão Preto. Proceedings of COBEM 2013, 2013.

Medeiros, R. ; Sartorato, M. ; Marques, F. D. ; Vandepitte, D. ; Tita, V. . Vibration-Based Damage Identification Applied For Composite Plate: Experimental Analyses. In: XXII International Congress of Mechanical Engineering, 2013, Ribeirão Preto. Proceedings of COBEM 2013, 2013.

Abstracts published in scientific conferences annals:



Sartorato, M. ; Tita, V. . An Evaluation of micro-scale based continuum damage mechanics models applied to low energy impact loads in composite materials. In: 18th International Conference on Composite Structures, 2015, Lisboa. Proceedings of ICCS 18, 2015.

Medeiros, R. ; Sartorato, M. ; Vandepitte, D. ; Tita, V. . Flexural After Impact (FAI): A new criterion to evaluate the residual strength of composite materials. In: 18th International Conference on Composite Structures, 2015, Lisboa. Abstracts of ICCS 18, 2015.

Sartorato, M. ; Medeiros, R. ; Ribeiro, M.L. ; Tita, V. . A non-linear finite element for curved active composites with embedded piezoelectric layers. In: 17th International Conference on Composite Structures, 2013, Porto. Abstracts of ICCS 17, 2013.



## 8 REFERENCES

---

- Airbus. (2017) Technology | Airbus Commercial Aircraft. Available in: <<http://www.aircraft.airbus.com/aircraftfamilies>>. Access in: Oct. 23, 2017.
- Altenbach, H., Bolchoun, A. e Kolupaev, V. A. (2013). Phenomenological Yield and Failure Criteria, in Altenbach, H., Öchsner, A., eds., *Plasticity of Pressure-Sensitive Materials*, Series ASM, Springer, Heidelberg, pp. 49-152.
- Angélico, R. A. (2009). Avaliação de modelos de falhas progressivas para estruturas em material compósito. Dissertação de Mestrado, Escola de Engenharia de São Carlos, Universidade de São Paulo, São Carlos. Recuperado em 2015-03-15, de <http://www.teses.usp.br/teses/disponiveis/18/18148/tde-05072010-132751/>
- Atherton, T. J., Kerbyson. D. J. (1999) Size invariant circle detection. *Image and Vision Computing*. Volume 17, Number 11, 1999, pp. 795-803.
- Azzi V.D. e Tsai S. (1965). Anisotropic strength of composites. *Exp Mech*, Vol. 5(8), pp. 283–310.
- Barbero E. J., Barbero J. C., Ugena, C.N. (2015). Analytical solution for plane stress/strain deformation of laminates with matrix cracks. *Composite Structures*. Vol.132, pp. 621-632.
- Barbero E. J., Barbero J. C., Ugena, C.N. (2016). Analytical solution for plane stress/strain deformation of laminates with matrix cracks under bending loads. *Composite Structures*. Vol.135.
- Barbero, E. J., Damiani, T. M., Trovillion, J. (2005). Micromechanics of fabric reinforced composites with periodic microstructure. *International Journal of Solids and Structures*, Vol. 42, pp. 2489-2509.
- Barbero, E.J. and Cortes, D.H. (2010). A mechanistic model for transverse damage initiation, evolution and stiffness reduction in laminated composites. *Composites: Part B*, Vol. 41, pp. 124-132.
- Bathe, K., (1996). *Finite Element Procedures*, Prentice Hall, New Jersey.
- Batra, R. C., Gopinath, G., Zheng, J. Q. (2012). Damage and failure in low energy impact of fiber-reinforced polymeric composite laminates. *Composite Structures*, Vol. 94(2), pp. 540–547.
- Belingardi, G. and Cavatorta, M.P. (2006). Bending fatigue stiffness and strength degradation in carbon-glass/epoxy hybrid laminates: Cross-ply vs. angle-ply specimens. *International Journal of Fatigue*, Vol. 28, pp. 815-825.
- Benzeggagh M. L., Davies P, Gong XJ, Roelandt JM, Mourin M, Prel YL. (1989). A mixed mode specimen for interlaminar fracture testing. *Comp Sci Technol*. Vol. 34pp. 129-172.
- Benzeggagh, M. L. and Kenane, N. (1996). Measurement of mixed-mode delamination fracture toughness of unidirectional glass/epoxy composites with mixed-mode bending apparatus. *Composite Science and Technology*. Vol. 56, pp. 439-449.
- Benzeggagha, M. L., Khellil, K., Chotard, T. (1995). Experimental determination of TSI failure tensorial terms  $F_{ij}$  for unidirectional composite materials. *Composites Science and Technology*, Vol. 55(2), pp. 145–156.
- Benzerga, A., A., Poulain, X., Chowdhury, K. A., Talreja, R. (2009). Computational Methodology for Modeling Fracture in Fiber-Reinforced Polymer Composites. *Aerosp. Eng.*, Vol. 22(3), pp. 296-303
- Boeing. (2017) Boeing 787 Dreamliner. Available in: <<http://www.boeing.com/commercial/787/>>. Access in: Oct. 20, 2017.
- Bresler, B. e Pister, K. S. (1985). Strength of concrete under combined stresses, *ACI Journal*, Vol. 551(9), pp. 321–345.

- Bulsara, V. N.; Qu, J., Talreja, R. (1999). Damage initiation under transverse loading of unidirectional composites with arbitrarily distributed fibers, *Composites Science and Technology*, Vol. 59(5), pp. 673-682
- Caliri Jr, M. F., Ferreira, A. J. M., Tita, V., (2016) New Generalized Unified Solution Method for Thin Laminated Plates. *AIAA Journal*, p. 1-5, 2016.0
- Caliri Júnior, M. F. (2015). Contribution for theory of plates: structural analyses of laminated composites and sandwich structures via unified formulations. (PhD Thesis) (Doutorado em Engenharia Mecânica) - Universidade de São Paulo.
- Caliri, M. F.; Ferreira, A. J. M. ; Tita, V. (2017) . A new finite element for thick laminates and sandwich structures using a generalized and unified plate theory. *International Journal for Numerical Methods in Engineering (Print)*, v. 109, p. 290-304.
- Callister, W. D. (2011). *Fundamentals of Materials Science and Engineering*. (W. Anderson, Ed.) John Wiley & Sons, Inc.
- Carraro, P. A., Quaresimin, M. (2014). A damage based model for crack initiation in unidirectional composites under multiaxial cyclic loading. *Composites Science and Technology*, Vol. 99(30), pp. 154–163.
- Carrera, E. and Ciuffreda, A. (2005) A unified formulation to assess theories of multilayered plates for various bending problems. *Composite Structures*, v. 69, p. 271-293, 2005.
- Carrera, E., Brischetto, S., Cinefra, (2010) M. Variable Kinematics and Advanced Variational Statements for Free Vibrations Analysis of Piezoelectric Plates and Shells (2010). *Computer Modelling in Engineering & Sciences CMES*, 65 (3), pp. 259-341.
- Chang, K. K., Chang, K. Y. (1987). A progressive damage model for laminated composites containing stress concentrations. *Journal of Composite Materials*. Vol. 21(9), pp. 834-855.
- Cinefra, M., Carrera, E., Valvano, S. (2014a) Variable Kinematic Shell Elements for the Analysis of Electro-Mechanical Problems. *Mechanics of Advanced Materials and Structures*, 22 (1:2), pp. 77-106.
- Cinefra, M., Lamberti, A., Zenkour, A.M., Carrera, E. (2014b) Axiomatic/Asymptotic Technique Applied to Refined Theories for Piezoelectric Plates. *Mechanics of Advanced Materials and Structures*, 22 (1:2), pp 107-124.
- Cosso. F. A., Barbero, E. J., Campo, F. A. (2013). Benchmark solution for degradation of elastic properties due to transverse matrix cracking in laminate composites. *Composite Structures*, Vol. 98, pp. 242-252.
- Daniel, I. M., Luo, J., Schubel, P. M., Werner, B. T. (2009) Interfiber/interlaminar failure of composites under multi-axial states of stress. *Composites Science and Technology*, Vol. 69(6), pp. 764–771.
- Danielsso, M., Parks, D. M., Boyce, M. C., (2002). Three-dimensional micromechanical modeling of voided polymeric materials. *Journal of the Mechanics and Physics of Solids* vol. 50 pp. 351–379
- Demasi L, Livne E. (2006). Structural ritz-based simple-polynomial nonlinear equivalent plate approach: an assessment. *J Aircraft* 2006;43(6).
- Demasi, L. (2009a), Mixed plate theories based on the Generalized Unified Formulation. Part I: General Equations. *Composite Structures*, Vol. 87, pp.12-22.
- Demasi, L. (2009b), Mixed plate theories based on the Generalized Unified Formulation. Part II: Layerwise theories. *Composite Structures*, Vol. 87, pp.12-22.
- Di Leonardo, G. (1979). Fracture toughness characterization of materials under multiaxial loading. *Int J Fracture* Vol. 15, pp. 537-589.

- Drucker, D. C. e Prager, W. (1952). Soil mechanics and plastic analysis for limit design. *Quarterly of Applied Mathematics*, vol. 10(2), pp. 157–165.
- Evans, K. E. e Zhang, W. C. (1987). The determination of the normal interaction term in the Tsai-Wu tensor polynomial strength criterion. *Composites Science and Technology*, Vol. 30(4), pp. 251–262.
- Elnekhaily, Sarah & Talreja, Ramesh. (2017). Damage initiation in unidirectional fiber composites with different degrees of nonuniform fiber distribution. *Composites Science and Technology*. 155. 10.1016/j.compscitech.2017.11.017.
- Ferreira, A. J. M.; Roque, C. M. C.; Carrera, E.; Cinefra, M.; Polit, O (2011). Radial basis functions collocation and a unified formulation for bending, vibration and buckling analysis of laminated plates, according to a variation of Murakami's Zig-Zag theory. *European Journal of Mechanics A/Solids*, v. 30, p. 559-570.
- Ferreira, A. J. M.; Roque, C. M. C.; Jorge, R. M. N. (2005) Analysis of composite plates by trigonometric shear deformation theory and multiquadrics. *Computers & Structures*, v. 83, p. 2225-2237.
- Fung, Y. C. (1994) A first course in continuum mechanics. Prentice Hall.
- García, I. G., Mantic, V., Blázquez, A., París, F. (2014). Transverse crack onset and growth in cross-ply [0/90]S laminates under tension. Application of a coupled stress and energy criterion. *International Journal of Solids and Structures*. [Accepted Manuscript, DOI: 10.1016/j.ijsolstr.2014.06.015].
- González C, LLorca J. (2006). Multiscale modeling of fracture in fiber-reinforced composites. *Acta Mater*, Vol. 54(16), pp. 4171-81.
- Hajikazemi, M., Sadr, M. H., Ramesh, T. (2015). Variational analysis of cracked general cross-ply laminates under bending and biaxial extension. *International Journal of Damage Mechanics*. Vol. 24(4), pp. 582-624.
- Ha-Minh, C., Kanit, T., Boussu, F., Imad, A. (2011). Numerical multi-scale modeling for textile woven fabric against ballistic impact. *Comput Mater Sci*, Vol. 50(7) pp. 2172–84.
- Hashin Z. (1980). Failure criteria for unidirectional fiber composites. *J Appl Mech*, Vol. 47, pp. 329–363.
- Hill R. (1948). A theory of the yielding and plastic flow of anisotropic materials. *Proc. Roy. Soc. A.*, Vol. 97, pp. 193–281.
- Hinton, M. J., Kaddour A. S. and Soden P. D.(2004). *Failure Criteria In Fibre Reinforced Polymer Composites: The World-Wide Failure Exercise*. Elsevier Science Ltd, Oxford, UK.
- Hinton, M., Kaddour, S., Smith, P., Li, S., Soden, P. (2011). *Failure Criteria in Fibre Reinforced Polymer Composites*. NAFEMS World Congress, Boston, 23rd-26th May, 2011.
- Huang, Y., Talreja, R. (2014). Statistical analysis of oblique crack evolution in composite laminates. *Composites: Part B*, [Article in Press, DOI: 10.1016/j.compositesb.2014.01.038].
- Huang, Z. M. (2000). The mechanical properties of composites reinforced with woven and braided fabrics. *Composite Science and Technology*, Vol. 60, pp. 479-498.
- Ivančević, D., Smojver, I. (2014). Micromechanical damage modelling using a two-scale method for laminated composite structures. *Composite Structures*, Vol. 108, pp. 223-233.
- Joffe, R., Kranikovs, A. and Varna, J. (2001). COD-Based simulation of transverse cracking and stiffness reduction in [S/90n]S laminates. *Composites Science and Technology*, Vol. 61, pp. 637-656.
- Kaddour, A. S. and Hinton, M. J. (2012), 'Evaluation of Theories for Predicting Failure in Polymer Composite Laminates Under 3-D States of Stress: Part A of the Second WorldWide Failure Exercise (WWFE-II)', Special issue of *J Composite Material*, September 2012; 46 (19-20).

- Kaddour, A. S. and Hinton, M. J. (2013), 'Evaluation of Theories for Predicting Failure in Polymer Composite Laminates Under 3-D States of Stress: Part B of the Second WorldWide Failure Exercise (WWFE-II)', Special issue of *J Composite Materials*, March 2013; 47 (6-7).
- Kaddour, A. S., Hinton, M. J., Smith, P. A. and Li, S. (2013). Damage, Matrix cracking Criteria for Fibre Reinforced Polymer Composites, Part A of the 3rd World-Wide Failure Exercise, Special issue of *J Composite Materials*, V 47, Nos 20-21.
- Kaddour, A. S., Hinton, M. J., Smith, P. A. and Li, S., (no year). A comparison between the predictive capability of current matrix cracking, continuum damage and fracture criteria for fibre reinforced composite laminates: Part B of WWFE-III', to be published.
- Kreyszig E. (1999) *Advanced engineering mathematics*. John Wiley & Sons, INC.
- Kumar, S. L., Cinefra, M., Carrera, E., Ganguli, R., Harursampath, D. (2014). Finite element analysis of free vibration of the delaminated composite plate with variable kinematic multilayered plate elements *Composites: Part B* 66 453–465
- Ladeveze, P., LeDantec, E. (1996). Damage modelling of the elementary ply for laminated composites. *Composites Science and Technology*, Vol. 43(3), pp. 257–267.
- Lemaitre, J. (1996). *A course on damage mechanics* (2nd ed.). Munich: Springer.
- Lemaitre, J., and Desmorat, R. (2005). *Engineering Damage Mechanics - Ductile, Creep, Fatigue and Brittle Failures*. Springer.
- Lemaitre, J., and Desmorat, R. (2005). *Engineering Damage Mechanics - Ductile, Creep, Fatigue and Brittle Failures*. Springer.
- Maimí, P., Camanho, P.P., Mayugu, J.A. and Turon, A. (2011a). Matrix cracking and delamination in laminated composites. Part I: Ply constitutive law, first ply failure and onset of delamination. *Mechanics of Materials*, Vol. 43, pp. 169-185.
- Maimí, P., Camanho, P.P., Mayugu, J.A. and Turon, A. (2011b). Matrix cracking and delamination in laminated composites. Part II: Evolution of crack density and delamination. *Mechanics of Materials*, Vol. 43, pp. 194-211.
- Maio, L., Monaco, E., Ricci, F. and Lecce, L. (2013), "Simulation of low velocity impact on composite laminates with progressive failure analysis", *Compos. Struct.*, Vol. 103, pp. 75-85.
- Meng, M., Le, H. R., Rizvi, M. J., Grove, S. M. (2015) 3D FEA modelling of laminated composites in bending and their failure mechanisms. *Composite Structures*, Vol. 119, pp. 693-708.
- Murari, V., Upadhyay, C. S. (2013). Micromechanics based diffuse damage model for unidirectional composites. *Composite Structures*, Vol. 96, pp. 671-680.
- Otero, F., Oller, S., Martinez, X., Salomón, O. (2015) Numerical homogenization for composite materials analysis. Comparison with other micro mechanical formulations. *Composite Structures*, Vol. 122, pp. 405-416.
- Papoulis, A., Pillai, S. U., (2002). *Probability, Random Variables, and Stochastic Processes* (4th ed.). Boston: McGraw-Hill. ISBN 0-07-366011-6.
- Paris, F. (2001) A Study of failure criteria f fibrous composite materials. NASA Report n.CR-2001-210661/March 2001.
- Prabhakar, O., Waas, M. (2013). Micromechanical modeling to determine the compressive strength and failure mode interaction of multidirectional laminates. *Composites: Part A*, Vol. 50, pp. 11-21.
- Puck, A., and Schürmann, H. (1998). Failure analysis of FRP laminates by means of physically based phenomenological models. *Composites Science and Technology*, Vol. 58(7), pp. 1045- 1067.

- Puck, A., and Schürmann, H. (1998). Failure analysis of FRP laminates by means of physically based phenomenological models. *Composites Science and Technology*, Vol. 58(7), pp. 1045- 1067.
- Puck, A., and Schürmann, H. (2002). Failure analysis of FRP laminates by means of physically based phenomenological models. *Composites Science and Technology*, Vol. 62(12-13), pp. 1633-1662.
- Puck, A., and Schürmann, H. (2002). Failure analysis of FRP laminates by means of physically based phenomenological models. *Composites Science and Technology*, Vol. 62(12-13), pp. 1633-1662.
- Puck, A., Koop, J., Knops, M. (2002). Guidelines for the determination of the parameters in Puck's action plane strength criterion. *Composites Science and Technology*, 52, pp. 371-378.
- Pupurs, A., Krasnikovs A., Varna, J. (2013). Energy release rate based fiber/matrix debond growth in fatigue. Part II: Debond growth analysis using Paris law. *Mechanics of Advanced Materials and Structures*, Vol. 20(4), pp. 288-296.
- Qatu, M. S.; Sullivan, R. W.; Wang, W. (2010). Recent research advances on the dynamic analysis of composite shells: 2000-2009, *Composite Structures*, vol. 93, pp. 14-31.
- Quaresimin, M., Vescovi, L., Grippa, F., Veneziani, F., Giubellini, A., Aymerich, F., De Rossi, N. (2014, in press). A numerical/experimental procedure for the assessment of the crash response of composite structures. *International Journal of Automotive Composites*.
- Rao, S. S. (2009). *Engineering Optimization: Theory and Practice*. John Wiley & Sons, Inc., Hoboken, New Jersey, Fourth Edition.
- Reddy, J. N. (2004). *Mechanics of laminated composite plates and shells: theory and analysis*. CRC Press, Boca Raton, Florida, Second Edition.
- Reddy, J. N. and Liu, C. F. (1985). A Higher-Order Shear Deformation Theory for Laminated Elastic Shells. *International Journal of Engineering Science*, Vol. 23, pp. 319-330.
- Reddy, J. N.; Ochoa, O. O. (1996). *Finite Element Analysis of Composite Laminates*. Kluwer Academic Print on Demand, 1996. 3rd Edition
- Reissner E. (1984) On a certain mixed variational theory and a proposed application. *Int J Numer Meth Eng*, 20:1366–8.
- Reissner E. (1986) On a mixed variational theorem and on shear deformable plate theory. *Int J Numer Meth Eng*, 23:193–8
- Ribeiro, M. L., Tita, V., Vandepitte, D. (2012). A new damage model for composite laminates, *Composite Structures*, Vol. 94(2), pp. 635-642.
- Riccio, A., De Luca, A., di Felice, G., Caputo, F. (2014). Modelling the simulation of impact induced damage onset and evolution in composites. *Composites Part B: Engineering*, Vol. 66, pp. 340–347.
- Rikards, R., Buchholz, F. G., Wang, H., Bledzki, A. K., Korjakin, A., Richard, H. A. (1998). Investigation of mixed mode I/II interlaminar fracture toughness of laminated composites by using a CTS type specimen. *Engineering Fracture Mechanics* Vol. 61, pp. 325-342.
- Shojaei, A., Guoqiang, L., Fish, J., Tan, P. J. (2014). Multi-scale constitutive modeling of ceramic matrix composites by continuum damage mechanics. *International Journal of Solids and Structures*. [Accepted Manuscript, DOI: 10.1016/j.ijsolstr.2014.07.026]
- Sih G. C. (1974). Strain-energy-density factor applied to mixed mode crack problems. *Int J Fracture*. Vol. 10, pp. 305-326.
- Singh, C. V., Talreja, R. (2009). A synergistic damage mechanics approach for composite laminates with matrix cracks in multiple orientations. *Mechanics of Materials*, Vol. 41, pp. 954-968.

- Singh, C. V., Talreja, R. (2010). Evolution of ply cracks in multidirectional composite laminates. *International Journal of Solids and Structures*, Vol. 41, pp. 954-968.
- Soldatos, K. P. (1992). A transverse shear deformation theory for homogeneous monoclinic plates. *Acta Mechanica*, v. 94, p. 195-220.
- Soldatos, K. P. (1993). A nonlinear transverse shear deformable plate theory allowing a multiple choice of trial displacement and stress distributions. *Composites Engineering*, Vol. 3, No. 9, pp. 885-897.
- Soldatos, K. P. and Timarci, T. (1993). A unified formulation of laminated composite, shear deformable, five-degrees-of-freedom cylindrical shell theories. *Composites Structures*, Vol. 25, pp. 165-171.
- Souza F.V., Allen D.H., Kim Y.R. (2008). Multiscale model for predicting damage evolution in composites due to impact loading. *Compos Sci Technol*, Vol. 68(13), pp. 2624-34.
- Srinivasaa, V., Shivakumara, V., Nayakaa, V., Jagadeeshaiaha, S., Seethrama, M. Shenoya, R., Nafidie, A. (2010) Fracture Morphology of Carbon Fiber Reinforced Plastic Composite Laminates. *Materials Research*, 13(3): 417-424
- Talreja, R. (2014). Assessment of the fundamentals of failure theories for composite materials. *Composites Science and Technology*, Vol. 105, pp. 190–201.
- Talreja, R. and Varna, J. (2016). *Modeling Damage, Fatigue and Failure of Composite Materials*. Woodland Publishing, 1st Edition.
- Tita, V. (2003). Contribuição ao estudo de danos e falhas progressivas em estruturas de material compósito polimérico. Ph.D. dissertation, Escola de Engenharia de São Carlos.
- Tita, V., De Carvalho, J., Vandepitte, D. (2008). Failure analysis of low velocity impact on thin composite laminates: Experimental and numerical approaches. *Composite Structures*, Vol. 83, pp. 413–428.
- Tsai S.W. e Wu E. M. (1971). A general theory of strength for anisotropic materials. *J. Compos Mater*, Vol. 5, pp. 58–80.
- Turon A, Camanho PP, Costaa J, Dávila CG. (2006). A damage model for the simulation of delamination in advanced composites under variable-mode loading. *Mech Mater*. Vol. 38(11), pp. 1072-1089.
- Ullah, H., Harland, A. R., Silberschmidt, V. V. (2013). Damage and fracture in carbon fabric reinforced composites under impact bending. *Composite Structures*, Vol. 101, pp. 144-156.
- Varna, J. and Berglund, L. (1991). Multiple Transverse Cracking and Stiffness Reduction in Cross-Ply Laminates. *Journal of Composites, Technology and Research*, Vol. 13(2) pp. 97-106
- Varna, J. and Joffe, R., Akshantala, N.V., Talreja, R. (1999). Damage in composite laminates with off-axis plies. *Composite Science and Technology*, Vol. 59, pp. 2139-2147.
- Varna, J.; Berglund, L. A., Talreja, R., Jakovics, A. (1993). A study of the opening displacement of transverse cracks in cross-ply laminates. *International Journal of Damage Mechanics*, Vol. 2(3), pp. 272-289.
- Vaughan, T. J., McCarthy, C. T. (2011). Micromechanical modelling of the transverse damage behavior in fibre reinforced composites. *Composites Science and technology*, Vol. 71, pp. 388-396.
- Whitney J M. Experimental characterization of delamination fracture. In: Pagano NJ, editors. *Interlaminar response of composite materials*. Amsterdam: Elsevier, 1989. p. 161±250.
- Wikipedia. (2017) Transverse isotropy. Available in: <[https://en.wikipedia.org/wiki/Transverse\\_isotropy](https://en.wikipedia.org/wiki/Transverse_isotropy)>. Access in: Oct. 21, 2017.
- Wu, R. Y., Stachurski, Z. H. (1984). Analysis of polynomial yield criteria applied to oriented polymers. *Polymer*, Vol. 25(10), pp. 1505–1512.



- Xu, J., Lomov, S. V., Verpoest, I., Daggumati, S., Van Paepegem, W., Degrieck, J. (2015). A progressive damage model of textile composites on meso-scale using finite element method: Fatigue damage analysis. *Computers & Structures*, Vol. 152, pp. 96-112.
- Yang, L., Yan, Y., Liu, Y., Ran, Z. (2012). Microscopic failure mechanisms of fiber-reinforced polymer composites under transverse tension and compression. *Composites Science and technology*, Vol. 72, pp. 1818-1825.
- Yang, L., Yan, Y., Ran, Z. G., Liu Y. J. (2013). A new method for generating random fibre distributions for fibre reinforced composites. *Compos Sci Technol*, Vol. 76(4), pp. 14–20.
- Zhang, Y. X., Zhang, H. S. (2010). Multiscale finite element modeling of failure process of composite laminates. *Composite Structures*, Vol. 92(9) pp. 2159-2165.
- Zhuang, L., Pupurs, A., Varna, J., Ayadi, Z. (2016). Fiber/matrix debond growth from fiber break in unidirectional composite with local hexagonal fiber clustering. *Composites Part B: Engineering*, Vol. 101, pp. 124-131.
- Zhuang, L., Talreja, R. (2014). Effects of voids on postbuckling delamination growth in unidirectional composites. *International Journal of Solids and Structures*, Vol. 51(5), pp. 936–944.
- Zienkiewicz, O. C., Taylor, R. L. *The Finite Element Method* (2000), Butterworth Heinemann, Second Edition.



APPENDIX I – MACROSCALE CODE FLOWCHART (GUF)

